ISBN 978-82-326-2016-6 (printed version)
ISBN 978-82-326-2017-3 (electronic version)
ISSN 1503-8181

Doctoral theses at NTNU, 2016:338

Øystein Farsund

Optical frequency conversion of high energy pulses with high beam quality and application in standoff detection of biological aerosols

NTNU
Norwegian University of
Science and Technology
Faculty of Information Technology,
Mathematics and Electrical Engineering
Department of Electronics and Telecommunications

NTNU
Norwegian University of
Science and Technology

Doctoral theses at NTNU, 2016:338

NTNU

NTNU
Norwegian University of
Science and Technology

Øystein Farsund

Optical frequency conversion of high energy pulses with high beam quality and application in standoff detection of biological aerosols

Thesis for the degree of Doctor Philosophiae

Trondheim, December 2016

Norwegian University of Science and Technology
Faculty of Information Technology,
Mathematics and Electrical Engineering
Department of Electronics and Telecommunications

NTNU
Norwegian University of
Science and Technology

NTNU
Norwegian University of Science and Technology

Thesis for the degree of Doctor Philosophiae

Faculty of Information Technology,
Mathematics and Electrical Engineering
Department of Electronics and Telecommunications

ISBN 978-82-326-2016-6 (printed version)
ISBN 978-82-326-2017-3 (electronic version)
ISSN 1503-8181

Doctoral theses at NTNU, 2016:338

Printed by Skipnes Kommunikasjon as

Abstract

Three main topics are addressed in this dissertation. The first is concerned with the techniques that can be used to improve beam quality from optical parametric oscillators (OPOs) generating high energy pulses in the nanosecond time regime. Such OPOs require the use of wide beams to avoid optical damage, in combination with a short resonator to enable a sufficient number of roundtrips to ensure high conversion efficiency. The resulting high Fresnel number of the resonator tends to favor multi-mode operation, and thereby a poor beam quality. A solution to this problem, studied theoretically and experimentally in this work, is the orthogonal critical planes optical parametric oscillator (OCP-OPO), which takes advantage of the beam quality improvement induced by the spatial walk-off between the signal and idler beams in the nonlinear crystals used in the OPO. OPOs using birefringent nonlinear materials and type 2 collinear critical phase matching have walk-off between signal and idler. When only a single nonlinear crystal is used, walk-off takes place in only one of the transversal directions, namely the critical plane, where there is a nonzero angle between the propagation vector ($\vec{k}$) and the Poynting vector ($\vec{S}$). However, using two different types of nonlinear crystals with orthogonal critical planes, walk-off takes place in orthogonal transversal directions in the two crystals when they are phase matched for the same process. The same is achieved when two identical crystals in an OPO are separated by a half-wave plate that rotates the linearly polarized pump and signal beams by 90°, and the crystals are oriented accordingly. Both types of OPO were demonstrated experimentally. The latter type has previously been proposed in the literature. The OCP-OPO permits the use of a simple and short linear resonator, allowing two-pass pumping, easy alignment, and wavelength tuning, and it has proven to be a reliable frequency conversion source for laboratory and field use.

Secondly, the thesis presents experimental results of sum frequency mixing of the output of an OCP-OPO with its pump pulse (or higher harmonics of the pump) to generate high-energy pulses in the ultraviolet. The results were obtained in a compact experimental setup. The achieved conversion efficiencies are comparable to the previously best published work on OPOs of similar complexity. Simulations indicate that even higher conversion should be possible with an optimized pump laser, but modifying this laser or building our own pump laser were out of scope of this work.

Finally, the ultraviolet sum-frequency device described above was employed in an experimental lidar setup for standoff detection of biological aerosols based on laser induced fluorescence. The instrument was used to acquire fluorescence spectra in an experiment where different biological agents were released in a semi-closed chamber at two hundred meters standoff distance. The fluorescence spectra of the biological aerosols were compared for different excitation wavelengths.

The results showed that excitation at 294 nm was more effective than the more common excitation at the third harmonic of a Nd:YAG laser (355 nm). The ratio between induced fluorescence and excitation pulse energy was as expected higher at the shorter wavelength. More importantly, however, was the diversity of the fluorescence spectra at the shorter wavelength excitation. This holds promise of improving automatic classification of potentially harmful biological agents from background aerosols such as pollen and fungi.

Acknowledgements

The research presented in this dissertation was brought about as part of projects on development of laser sources and instrumentation at Norwegian Defence Research Establishment (FFI). I sincerely appreciate the opportunity I have been given to carry out the research and reporting to complete this thesis. I am also grateful for my job, in the intersection of experimental, theoretical and practical work.

A number of persons at FFI have been involved in the scientific accomplishments presented herein. First of all, I would like to express my gratitude to Gunnar Rustad, who I have been working closely with in the topics treated herein, and who introduced me to the fields of lasers and nonlinear optics. He has also led the research leading to the results of the current work. In addition, he has encouraged me to carry out the extra effort it has been to draw parts of this research together into a dissertation. I would also like to thank the leader of our research group, Knut Stenersen, for continuous encouragement, support, invaluable discussions and recommendations during the course of this research. I have also taken advantage of close collaboration with Gunnar Arisholm who always found time for most clarifying discussions in the maze of nonlinear optics, as well as providing simulation models, Sisyfos support, and supervision in my scientific struggles. I would also like to thank many other colleagues for discussions, suggestions, criticism and practical help: Magnus W. Haakestad, Helge Fonnum, Espen Lippert, and Stephane Nicolas.

I am also grateful to prof. Johannes Skaar who took the time to evaluate the research results with an eye to writing a thesis about them, and encouraged me to proceed and complete.

Finally, I would like to thank my dear wife Bodil for her patience, extra effort and unconditional support.

Contents

Chapter 1

Introduction

Radiation characterized by high spatial and temporal coherence is important in a number of applications ranging from telecom and industrial processes to sensing and spectroscopy. Coherent light is commonly produced by a laser. Lasers can be realized using different principles of pumping and gain materials [1]. Solid state laser materials are often used when aiming for high power beams or high energy pulses. The laser material determines the frequency of the radiation, and they are available only in specific wavelength intervals. Moreover, the frequency tunability of a laser is limited. One way to reach frequencies uncovered by solid state laser materials is by second order nonlinear frequency conversion. Nonlinear frequency conversion also allows tunability in terms of frequency.

The work presented in this thesis deals with second order nonlinear frequency conversion in optical parametric oscillators (OPOs) and sum frequency generation (SFG) devices pumped by pulses with high energy and of several nanoseconds duration. A small pump beam width is favorable in terms of beam quality and high conversion efficiency. However, the fluence has to be kept below the damage threshold of the optical components. The fluence can be reduced either by reducing the pulse energy or increasing the beam width. Pulse energies in the tens of millijoule range require beam widths with diameters in the millimeter range. Temporally, efficient conversion in an OPO requires that the resonant signal wave has sufficient number of roundtrips while the pump pulse and signal overlap inside the nonlinear material. Nanosecond pulses are on the order of 1 m long, which means that the resonator length should be $\sim$10 cm. A several millimeter wide pump beam in a short resonator allows many transverse modes thus poor beam quality, unless other actions are taken to improve it. On the other hand, the applications call for high energy pulses and high beam quality, which is essential for high nonlinear frequency conversion efficiency and for directing

energy into a small solid angle. Examples of applications are stand-off detection, which has been the main motivation of the work presented herein, atmospheric sensing and laser ranging.

The motivation for this work, standoff detection, is presented in the next section. Section 1.2 gives a brief on the history on nonlinear optics, and finally the outline of the thesis is presented in Section 1.3.

1.1 Motivation and background - standoff detection

FFI's main motivation for putting effort into the work presented in this thesis, was to build a demonstrator for standoff detection and classification of biological aerosols at a distance of several hundred meters. A summary of the background for these activities is given in this section.

An attack using biological agents in the form of aerosols has the potential to infect tens of thousands of people, leaving its victims unaware of their situation until symptoms start to develop [2]. Real-time detection of biological agents has therefore been identified as urgent in order to provide early warning to be able to take protective measures [3] before contamination. In contrast to chemical warfare agents, with well defined absorption lines in the optical spectrum, biological agents can contain thousands of different molecules, complicating the detection as compared to detection of chemical warfare agents.

In this context, we are interested in optical standoff detection, which may be realized by several different techniques. Examples of active techniques are ultraviolet laser induced fluorescence (UV-LIF), infrared (IR) depolarization and long-wave infrared differential scattering. UV-LIF is one of the most promising methods [4], offering potentially kilometer standoff distance with acceptable sensitivity and ability to discriminate agents. Employing state of the art classification algorithms to such data, a UV-LIF based system holds promise even with false alarm rates sufficently low for an operational instrument [J1, C1, C2]. In the following subsection the principle of operation and requirements of a UV-LIF based lidar for standoff bioaerosol detection are presented. These requirements lead to specifications of the OPO and SFG devices which will be described later.

Ultraviolet laser induced fluorescence in biological detection

UV-LIF uses the fluorescence properties of a number of molecules present in biological material. The two most important fluorescent molecules for UV-LIF applications are the reduced form of nicotinamide adenine dinucleotide (NADH) and tryptophan. NADH is important in cell respiration, thus present in all living organisms. Tryptophan is an amino acid acting as protein building blocks

in protein biosynthesis, and is found also in non-living organisms, such as a virus. The two molecules fluoresce differently, in that NADH absorbs radiation at longer wavelengths as compared to tryptophan [5]. Standoff detection implies extremely low signal levels, as a consequence of the low fluorescence cross section of the agent in combination with long distance between instrument and agent. It is therefore crucial that the instrument delivers as much light as possible to the agent present in the field of view, in a wavelength interval with highest possible fluorescence cross section. Thus not only readily available ultraviolet (UV) wavelengths must be considered, but also the fluorescence cross section of the agents. The magnitude of the fluorescence cross section should be considered for highest possible return signal. The fluorescence emission spectrum should be assessed with respect to possibility of classifying the different agents. A standoff instrument working at several hundred meters distance with appropriate distance resolution requires laser pulses with high energy and nanosecond duration, in addition to fairly high beam quality to be able to deliver sufficient energy into a small probe volume. Presently, the best type of laser in terms of optical specifications in combination with compactness, robustness and availability, is a 1064 nm wavelength, Q-switched laser based on the Nd:$Y_3Al_5O_{12}$, neodymium-doped yttrium aluminium garnet laser crystal (Nd:YAG) with frequency conversion to the third (355 nm) or fourth harmonic (266 nm) of the fundamental wavelength. Such lasers are commercially available in fairly small (portable to field trials, at least) formats, delivering approximately 10 ns pulses with energy on the order of 100 mJ. On the other hand, the fluorescence cross sections of relevant agents turn out to peak at wavelengths between the third and fourth harmonic.

FFI started an experimental bio-standoff detection activity in 2004, by building a lidar based on the third harmonic of a Nd:YAG commercially available laser, an intensified CCD-camera for fluorescence spectra measurements, and a photo multiplier tube (PMT) with response in the UV for ranging by means of elastic backscattering. The instrument was tested in laboratory [J1] as well as field trials including dissemination of bio-agents in closed chamber as well as in open air [C3]. Signal processing algorithms were developed, and the results showed that the biolidar could measure and discriminate the relevant agents at several hundred meters [J1, C1–C4]. However, a literature study and in-house work indicated that the fluorescence return signal could be more than doubled by reducing the excitation wavelength below 355 nm. The ideal wavelength should also be longer than 266 nm for two main reasons. First of all, the fluorescence cross section has its maximum around 280 nm [6]. Secondly, ozone in relevant concentration levels close to the ground [R1] absorbs significantly at 266 nm. Based on the results of biolidar research conducted by partners in NATO Research and Technology Organization [4], as well as internal work at FFI [6, R1, R2], we decided to build a coherent light source with wavelength in the $280 - 300$ nm range. A study

of ways to reach this wavelength region, with pulses of nanosecond duration and pulse energy on the order of tens of millijoule, concluded with nonlinear frequency conversion. More specifically, optimal excitation wavelength can be achieved by sum frequency mixing the signal from an OPO with the harmonic of the OPO pump laser [R3].

1.2 Brief on the history of nonlinear optics

The development of the field of nonlinear optics is described in textbooks [7–11]. Papers on the history of nonlinear optics have also been published, for example Nobel Laureate N. Bloembergen's year 2000 perspective on the past, present and future [12], or E. Garmire's review on the impact of nonlinear optics in 2013 daily life [13]. A few years ago, the nonlinear optics community celebrated its 50 years anniversary, which was marked at topical conferences [14, 15] by presentations given by some of the pioneers of nonlinear optics; N. Bloembergen, A. Yariv, S. Harris, R. Shen, R.L. Byer and G. Mourou. Only a brief summary, mainly based on the above mentioned references is given in this section, trying to highlight some major events in the context of this thesis. The earliest observations of nonlinear electromagnetic phenoma were driven by DC or low-frequency electric and magnetic fields. An example is the (DC) qudratic Kerr electrooptic effect (not to be confused with the optical or AC Kerr effect). The Kerr electrooptic effect is how a DC electric field induces birefringence in isotropic media [12], [16, section 18.1]. Kerr showed in 1875 that the birefringence was proportional to the square of the electric DC field [17]. The Kerr effect is described by a third order nonlinear susceptibility with polarization proportional to the cubic in the electric field, however, of these only one can be an optical field, thus it is not a true nonlinear optical effect. Another precursor of nonlinear optics was the linear electrooptic Pockels effect, studied by Pockels around 1895. The optical polarization is bilinear in the DC field and the optical field amplitude. Half a century later, KH_2PO_4, potassium dihydrogen phosphate (KDP) crystals were grown to be used as fast optical switches and microwave modulators, as the DC field was replaced by a microwave electric field with frequency ω_m, creating sidebands at $\omega \pm \omega_m$. ω_m is not limited to the microwave region, and may be in the optical range, thereby modifying the refractive index at its own frequency, and create 'sidebands' at 0 and 2ω, thus it is a true nonlinear optical effect. According to R. W. Boyd, the first published observation of a nonlinear optical effect, was by G. N. Lewis in 1941. In an organic dye in a boric acid glass host he reported increased saturation of fluorescence intensity with increasing optical field excitation [18].

Nonlinear optical effects become significant when the electric field strengths are on the order of those of interatomic fields ($\sim 10^8$ V/m). Therefore, the inven-

tion of the laser in 1960 [19, 20] was the enabling technology for the development of nonlinear optics. The observation of frequency doubling in quartz using a ruby laser by Franken *et al.* in 1961 [21] is often held to be the birth of the field of nonlinear optics. Shortly after that, the seminal paper by Armstrong *et. al.* [22] laid the foundation for the theoretical understanding of nonlinear optical phenomena. The importance of phase matching was ackowledged, and a number of nonlinear effects, such as sum frequency mixing [23, 24], parametric amplification [25] and optical parametric oscillation [26] were demonstrated. Two-photon absorption and stimulated Raman scattering were demonstrated by 1964 [12]. Nonlinear optics was also an important scientific field in the former Soviet Union from 1962, lead by R. Khokhlov and S. Akhmanov [25, 27–29].

In the context of this thesis, parametric processes are of particular importance. In a parametric process, the quantum state of the nonlinear material is not changed [11, Section 1.2]. R. L. Byer's presentation *Fifty years of Nonlinear Optics, tunable sources from OPOs to Coherent X-rays* [14, 30] gives a timeline of nonlinear optics from his perspective. This includes the events around the first OPO and tunable continuous wave (CW) parametric laser, the development of nonlinear materials and quasi phase matching (QPM) in the 1970's and 1980's, from ∼2 W to 100 kW CW coherent radiation and MJ pulse energy in the IR and UV at the National Ignition Facilities. A. Yariv presents the beginning of quantum nonlinear optics and its answers to communication challenges in *Celebrating the 50^{th} anniversary of nonlinear optics* [14, 31]. The quantum description of nonlinear optics forms the foundation for the understanding of a number of phenomena and applications, such as noise and coherence in parametric amplifiers and OPOs, spontaneous parametric fluorescence, squeezing of the quantum fluctuations, and entangled photon states.

Nonlinear optics has impact on the improvement of lasers, understanding light-material interactions in spectroscopy as well as in information technology [13]. In the first category, changing the wavelength of coherent light, for example using OPOs and generation of white light continuum lend themselves to a number of applications including spectroscopy. Short laser pulses can be generated by nonlinear processes such as Q-switching and modelocking. Q-switching can produce pulses with high energy and of nanosecond duration. Mode-locking can produce ultrashort (femtosecond) pulses and is presently a hot research topic. Frequency-resolved optical gating (FROG) is a widely used technique to characterize the time dependence of femtosecond laser pulses. Commonly used FROG set-ups use a nonlinear material such as second harmonic generation (SHG) to shift the frequency of the laser pulse before it is frequency resolved [32]. Laser-material interactions can cause permanent changes, called machining, or temporary changes as used in spectroscopy, or changes in selected species of the material and used as analysis tools. Laser induced breakdown spectroscopy (LIBS) is an

example of the latter. Permanent changes are caused by heat or nonlinear effects, normally multiphoton absorption. Laser machining by way of ablation uses nonlinear processes. In the information technology category, stimulated Brillouin scattering (SBS) and, less importantly, stimulated Raman scattering (SRS), limit the data rates, transmission lengths and simultaneous number of wavelengths that can be transmitted in a single mode optical fiber. On the other side, Raman lasers and Raman fiber amplifiers are practical sources in telecommunications. Four wave mixing is another nonlinear effect putting restrictions to wavelength division multiplexing systems and high energy laser sources.

In summary, a number of present important daily life applications, such as commercial lasers, telecommunications, material processing and military applications all benefit from nonlinear optical processes. This is also reflected in science, where at least nine Nobel prizes in physics and chemistry have been enabled by nonlinear optics [13].

1.3 Outline of the thesis

Chapter 2 presents the theory of second order nonlinear interactions in general, emphasizing OPOs. This is also covered in a number of textbooks, e.g. [7, 8, 11, 33], but is included for completeness. Chapter 3 reviews OPOs for the generation of high energy nanosecond pulses in the spectral domain for biolidar applications. The advantages and shortcomings of the different OPOs are discussed. The proposed method of OPOs using orthogonal critical planes is also presented and compared to existing methods. Sum frequency mixing the output of a high energy nanosecond OPO with the pump laser or one of its harmonics to generate ultraviolet (UV) pulses is presented in chapter 4. In chapter 5 an application using orthogonal critical planes OPO and SFG in standoff biological aerosol detection is described. The central papers published within this thesis are summarized in chapter 6 before conclusion and outlook are presented. The papers are listed in chapter 8, and author contributions are stated in chapter 9.

The publications of this thesis are cited with capital roman numbers in bold, e.g. [**I**] and reprinted in appendices I-V. Other relevant work has been published in connection with this thesis. These publications are cited with the prefix J, C or R before an arabic numeral, depending on if it were published in a journal, at a conference or as a technical report, respectively.

Chapter 2

Theory of second order nonlinear optics

Presence of light can modify the optical properies of a material system. These changes can lead to a number of phenomena, for example second- (SHG) and third harmonic generation, sum frequency generation (SFG) and difference frequency generation (DFG). The study of phenomena following such light induced modifications of a material's optical properties is called nonlinear optics. Some of the modifications of the optical properties of a material can be described by the polarization, or average dipole moment per unit volume of the material. A linear dependence between field strength and polarization is sufficient in many cases. However, as the field strength of the imposed light increases, typically from an intense laser beam, modelling the polarization with linear dependence on the field strength only is no longer sufficient. When the nonlinear polarization can be treated as perturbations, it may be expanded as a Taylor series of the electric field. In this chapter the theory describing up to second order nonlinear effects is presented.

In Section 2.1 the governing equations of nonlinear optics are deduced from Maxwell's equations, and the nonlinear polarization is discussed in Section 2.2. Maxwell's equations in macroscopic media and the relation between the polarization and the electromagnetic fields form the basis for the wave equation. The wave equation and some fundamental principles of second order nonlinear interactions are discussed using simplified cases in Section 2.3 and Section 2.4. Poynting vector walk-off is utilized in the main result of this thesis, the orthogonal critical planes optical parametric oscillator (OCP-OPO) [I, II, V], and is therefore explained. Section 2.5 discusses phase matching, which is particularly important for the efficiency of parametric frequency conversion of second order nonlinear

interaction. The basics of OPOs are summarized in Section 2.6. Finally, an overview of simulation system for optical science (Sisyfos), FFI's in-house made simulation software indispensable in the present work, is given in Section 2.7.

2.1 Fundamentals

Maxwell's equations govern electromagnetic phenomena [34]. For sources in vacuum, these eqations read (SI-units):

$$\begin{aligned} \nabla \cdot \vec{e} &= \frac{\rho}{\epsilon_0} \\ \nabla \cdot \vec{b} &= 0 \\ \nabla \times \vec{e} + \frac{\partial \vec{b}}{\partial t} &= 0 \\ \nabla \times \vec{b} - \frac{1}{c^2}\frac{\partial \vec{e}}{\partial t} &= \mu_0 \vec{j} \end{aligned} \tag{2.1}$$

In (2.1), $\vec{e}$ is the electric field and $\vec{b}$ is the magnetic field, both with rapid and drastic variations over microscopic distances. ρ and $\vec{j}$ are the (microscopic) charge and current densities, respectively, whereas ϵ_0 and μ_0 are the vacuum permittivity and permeability. $c = (\epsilon_0\mu_0)^{-\frac{1}{2}}$ is the speed of light in vacuum. The microscopic equations may be solved for a small number of well defined charges and currents. However, for a macroscopic aggregate of matter a microscopic solution becomes impossible. For one, the number of charged particles in atoms and nuclei, are prohibitively large. Secondly, the microscopic fields' drastic variations over atomic distances are irrelevant to our observations at a macroscopic scale. Averaging the microscopic fields or sources over a volume large compared to an atom (yet small compared to the wavelength), we obtain macroscopic fields and sources. Maxwell's macroscopic equations derived from the microscopic Equations (2.1) are [34, Section 6.7]:

$$\begin{aligned} \nabla \cdot \vec{D} &= \rho \\ \nabla \cdot \vec{B} &= 0 \\ \nabla \times \vec{E} + \frac{\partial \vec{B}}{\partial t} &= 0 \\ \nabla \times \vec{H} - \frac{\partial \vec{D}}{\partial t} &= \vec{J} \end{aligned} \tag{2.2}$$

In (2.2), $\vec{E}$ is the macroscopic electric field (average of $\vec{e}$), $\vec{B}$ is the macroscopic magnetic induction (average of $\vec{b}$), $\vec{D}$ is the electric displacement (or electric

induction) and $\vec{H}$ is the macroscopic magnetic field. ρ is the macroscopic (free) charge density. Finally, $\vec{J}$ is the macroscopic (free) current density.

$\vec{D}$ and $\vec{H}$ are determined from the matter's response to the external fields. The constitutive relations connect the fields $\vec{D} = \vec{D}[\vec{E}, \vec{B}]$ and $\vec{H} = \vec{H}[\vec{E}, \vec{B}]$, and may be very complicated. Following [34] they are expanded in a series of multipoles and read:

$$\begin{aligned} \vec{D} &= \epsilon_0 \vec{E} + \vec{P} - \nabla \cdot \mathbf{Q} + ... \\ \vec{B} &= \mu_0 \vec{H} + \mu_0 \vec{M} + ... \\ \vec{J} &= \sigma \vec{E} + ... \end{aligned} \tag{2.3}$$

Here, $\vec{P}$ is the macroscopic polarization, $\vec{M}$ is the macroscopic magnetization, $\mathbf{Q}$ is the macroscopic quadrupole density and σ is the conductivity. In dielectric materials the quadrupole moment and higher order terms as well as the magnetic dipole may be neglected [9, p. 3]. Moreover, working in the optical frequency regime and with nonmagnetic materials, $\mu = \mu_0$ [35, §6]. Furthermore, we assume no free charges or currents, $\rho = 0$ and $\vec{J} = 0$. We are thus left with the macroscopic polarization for the description of the matter response to the applied fields. From (2.2) we find the governing equations for the macroscopic fields in our case:

$$\nabla \cdot \vec{D} = 0 \tag{2.4}$$

$$\nabla \cdot \vec{B} = 0 \tag{2.5}$$

$$\nabla \times \vec{E} + \frac{\partial \vec{B}}{\partial t} = 0 \tag{2.6}$$

$$\nabla \times \vec{H} - \frac{\partial \vec{D}}{\partial t} = 0 \tag{2.7}$$

The constitutive equations, (2.3), simplify to:

$$\vec{D} = \epsilon_0 \vec{E} + \vec{P} \tag{2.8}$$

$$\vec{B} = \mu_0 \vec{H} \tag{2.9}$$

2.2 The nonlinear polarization

The polarization $\vec{P}$ is a vector quantity representing the electric dipole moment per unit volume of a dielectric medium [11, Chapter 1],[35, §6]. The nonlinear optical polarization depends on the detailed electronic and molecular structure of the material and is expressed in the susceptibility χ, which in general is a tensor. χ is an operator which converts the electric field(s) to the polarization. In linear

theory the polarization is linear with respect to the electric field, $\vec{P} = \epsilon_0 \chi^{(1)} \vec{E}$, or on component form $P_i = \epsilon_0 \chi^{(1)}_{ij} E_j$, where repeated indices imply summation. In nonlinear theory, the polarization depends nonlinearly on the electric field. Several textbooks deduce the nonlinear polarization from a microscopic perspective, see for example [7, Chapter 2], [9, Section 1.3-4], [36, Chapter 13] and [11, Chapter 3].

For a phenomenological understanding of the underlying physics, nonlinear susceptibility can be explained from a classical perspective where the electron motion is modelled as an anharmonic oscillator, or by a free electron gas model [9, Section 1.3-4], [37, Section 3.2]. In the anharmonic model the electrons of a dielectric medium are held in equilibrium by the nucleus of the atoms, and brought out of equilibrium by an externally applied electric field. The displaced electrons described by the anharmonic oscillator set up dipole moments and act as new sources (displacement field) to and modify the electric field locally. The anharmonic term is small and treated as a perturbation. The polarization can then be expressed as a Taylor series expansion in the electric field. As the applied field increases, higher order terms of the polarization must be included for an appropriate description of the electron motion. In the free electron gas model, the externally applied electromagnetic field results in electronic motion driven by the Lorentz force $\vec{F} = q\left(\vec{E} + \vec{v} \times \vec{B}\right)$, of which the last term is nonlinear, however small compared to the first, and thus treated as a perturbation. Averaging to macroscopic scales yields expressions for the macroscopic susceptibilities.

When the interacting beams have frequencies far from resonance and $\vec{E}$ is sufficiently weak, perturbation theory holds. In that case the macroscopic nonlinear polarization may be expanded in a Taylor series of the applied field $\vec{E}$:

$$
\begin{aligned}
\vec{P}(\vec{r},t) &= \epsilon_0 \int_{-\infty}^{\infty} \chi^{(1)}(\vec{r}-\vec{r}',t-t') : \vec{E}(\vec{r},t) d\vec{r}' dt' \\
&+ \int_{-\infty}^{\infty} \chi^{(2)}(\vec{r}-\vec{r}_1,t-t_1;\vec{r}-\vec{r}_2,t-t_2) : \\
&\quad \vec{E}(\vec{r}_1,t_1)\vec{E}(\vec{r}_2,t_2) d\vec{r}_1 dt_1 d\vec{r}_2 dt_2 \\
&+ \cdots \\
&+ \int_{-\infty}^{\infty} \chi^{(n)}(\vec{r}-\vec{r}_1,t-t_1;\vec{r}-\vec{r}_2,t-t_2;\ldots\vec{r}-\vec{r}_n,t-t_n) : \\
&\quad \vec{E}(\vec{r}_1,t_1)\vec{E}(\vec{r}_2,t_2)\cdots\vec{E}(\vec{r}_n,t_n) d\vec{r}_1 dt_1 d\vec{r}_2 dt_2 \cdots d\vec{r}_n dt_n \\
&+ \cdots
\end{aligned}
$$

Here, $\chi^{(n)}$ is the n^{th} order nonlinear susceptibility, which is a tensor of rank $n+1$. The colon ':' denotes that the tensor $\chi^{(n)}$ to the left of the symbol operates on the tensor product of the electric fields $(\vec{E}(\vec{r}_1,t_1)\vec{E}(\vec{r}_2,t_2)\cdots)$, which appears to

the right of the symbol. In the electric dipole approximation, the susceptibility is independent of $\vec{r}$. This means that the nonlocality of the susceptibility can be neglected. This assumption is often permissible at optical frequencies and lower [34, Section 1.4]. In this case, the susceptibility is a function of frequency only, and can be written:

$$\chi^{(n)} = \chi^{(n)}(\omega = \omega_1 + \omega_2 + \cdots \omega_n; \omega_1, \omega_2, \cdots \omega_n)$$

$\chi^{(1)}$ is the linear susceptibility (refraction and linear absorption [16, Section 5.2]) and $\chi^{(2)}$ is the second order susceptibility tensor. It can be shown that only noncentrosymmetric media have a nonzero second order polarization [11, Section 1.4-5]. $\chi^{(2)}(\omega)$ has 27 elements. However, the number of nonzero independent elements may be greatly reduced due to symmetries. For a given second order process involving beams with well-defined polarizations and narrow range of angles, the susceptibility can be reduced to a scalar, termed $\chi_{\text{eff}} = 2d_{\text{eff}}$, see for example [11, p. 40]. The third order susceptibility $\chi^{(3)}$ is responsible for third harmonic generation, stimulated Raman scattering, self phase modulation, two-photon absorption and four wave mixing (FWM). The optical nonlinear susceptibilities are small, thus field strengths on the order of the atomic electric fields are required to observe nonlinear effects. Only second order nonlinear effects are treated here.

With the basic set of equations, (2.4-2.9), and an expression for the polarization, we can find the wave equation which describes the propagation and interaction of optical waves in nonlinear media.

2.3 The wave equation

Taking the curl of (2.6) and using that the time derivative and curl operators commute, we find:

$$\nabla \times \nabla \times \vec{E} = -\frac{\partial}{\partial t}\left(\nabla \times \vec{B}\right)$$

Inserting (2.9) and using (2.7) yield:

$$\nabla \times \nabla \times \vec{E} = -\mu_0 \frac{\partial^2 \vec{D}}{\partial t^2}$$

Inserting (2.8) and rearranging, we obtain the inhomogeneous wave equation in nonlinear media:

$$\left(\nabla \times \nabla \times + \frac{1}{c^2}\frac{\partial^2}{\partial t^2}\right)\vec{E} = -\mu_0 \frac{\partial^2 \vec{P}}{\partial t^2} \tag{2.10}$$

By help of identity $\nabla \times (\nabla \times \vec{F}) = \nabla(\nabla \cdot \vec{F}) - \nabla^2 \vec{F}$ (2.10) may be written:

$$\nabla(\nabla \cdot \vec{E}) - \nabla^2 \vec{E} + \frac{1}{c^2} \frac{\partial^2 \vec{E}}{\partial t^2} = -\mu_0 \frac{\partial^2 \vec{P}}{\partial t^2} \tag{2.11}$$

A similar equation for $\vec{H}$ can be found. It is normally suffient to solve for $\vec{E}$ because of the simple relation between $\vec{E}$ and $\vec{H}$. Solutions of the wave equation for different cases are summarized in the following. For details, see e.g. [38, Chapter 2].

2.3.1 Free space

In free space $\vec{D} = \epsilon_0 \vec{E}$, and (2.4) implies $\nabla \cdot \vec{E} = 0$. The wave equation reduces to the familiar form

$$\left(\frac{1}{c^2} \frac{\partial^2}{\partial t^2} - \nabla^2 \right) \vec{E} = 0$$

This equation has plane wave eigenmode solutions:

$$\vec{E}(\vec{r}, t) = \mathcal{E} \hat{e} e^{-i(\omega(\vec{k})t - \vec{k} \cdot \vec{r})} + cc$$
$$\vec{H}(\vec{r}, t) = Z_o^{-1} \mathcal{E} \hat{h} e^{-i(\omega(\vec{k})t - \vec{k} \cdot \vec{r})} + cc$$

$Z_0 = \sqrt{\frac{\mu_0}{\epsilon_0}}$ is the vacuum impedance and the amplitude $\mathcal{E}$ is a complex constant, $\hat{e}$, $\hat{h}$ are unit vectors along the electric and magnetic fields, respectively. ω can be taken as positive with no loss of generality due to the complex conjugate (denoted cc) terms. $\vec{k} = k\hat{u}$ is the wave vector, $\omega(\vec{k}) = c|\vec{k}|$, and $\hat{e}, \hat{h}, \hat{u}$ form an orthonormal basis. There are two eigenmode solutions with orthogonal polarizations (along $\hat{e}_1$ and $\hat{e}_2$) for each propagation direction $\hat{u}$, and the unit normal vectors $\hat{e}_1$, $\hat{e}_2$ and $\hat{u}$ form a right-handed orthogonal set, defined by some vector $\hat{v}$ non-parallel to the propagation direction $\hat{u}$:

$$\hat{e}_1 = \frac{\hat{u} \times \hat{v}}{|\hat{u} \times \hat{v}|}$$
$$\hat{e}_2 = \hat{u} \times \hat{e}_1$$

By way of (2.6) and (2.7) the eigenpolarization directions for $\vec{H}$ are easily found:

$$\hat{u} \times \hat{e}_1 = \hat{h}_1 = \hat{e}_2$$
$$\hat{u} \times \hat{e}_2 = \hat{h}_2 = -\hat{e}_1$$

Now, any beam can be expanded in terms of the eigenmodes, see for example [38, Section 2.3], [33, 37].

2.3.2 Linear media

In linear dielectric media the polarization is $\vec{P}^{\text{linear}} = \epsilon_0 \chi^{(1)} : \vec{E}$, and the displacement can be written $\vec{D} = \epsilon_0(1+\chi^{(1)}) : \vec{E} = \epsilon_0 \epsilon : \vec{E}$. The linear susceptibility $\chi^{(1)}$ is a tensor for anisotropic media. In combination with (2.8) the wave equation can be written:

$$\left(\nabla \times \nabla \times + \frac{1}{c^2}\frac{\partial^2}{\partial t^2}\right)\vec{E} = -\mu_0 \frac{\partial^2 \vec{P}^{\text{linear}}}{\partial t^2}$$

$$\left(\nabla \times \nabla \times + \frac{1}{c^2}\frac{\partial^2}{\partial t^2}\,\epsilon\right)\vec{E} = 0 \tag{2.12}$$

In order to find the eigenmodes, we assume a solution equal to the solution in free space. We have $\vec{D} = \mathcal{E}\epsilon_0 \xi \hat{d} \exp[-i(\omega(\vec{k})t - \vec{k}\cdot\vec{r})] + cc$, with unit vector $\hat{d}$, and $\xi\hat{d} = \epsilon\hat{e}$. From (2.4):

$$\nabla \cdot \vec{D} \propto \hat{u} \cdot \hat{d} = 0$$

thus the displacement $\hat{d}$ is orthogonal to the direction of propagation $\hat{u}$. The same is valid for $\hat{h}$ by way of (2.5) and (2.9). Inserting the trial solution into (2.12), we get:

$$(i\vec{k})^2 \hat{u} \times (\hat{u} \times \hat{e}) + \frac{(-i\omega)^2}{c^2}\hat{e} = -\mu_0(-i\omega)^2 \epsilon_0 \xi \hat{d}$$

$$(ck)^2 \hat{u} \times (\hat{u} \times \hat{e}) + \omega^2 \hat{e} = -\xi \hat{d}$$

Using the vector identity $\vec{a} \times (\vec{b} \times \vec{c}) = (\vec{a}\cdot\vec{c})\vec{b} - (\vec{a}\cdot\vec{b})\vec{c}$, we obtain:

$$c^2k^2(\hat{u}\cdot\hat{e})\hat{u} + \xi\hat{d} = (c^2k^2 - \omega^2)\hat{e} \tag{2.13}$$

Hence $\hat{e}$ must lie in the $(\hat{u}, \hat{d})$ plane to satisfy the wave equation. From (2.7) it is easily seen that the vectors $\hat{d}, \hat{h}, \hat{u}$ form a righthanded set of orthogonal unit vectors.

In isotropic media (as in free space), $\hat{e} \parallel \hat{d}$ and the eigenmodes are degenerate because they have equal index of refraction (as well as equal propagation direction and frequency) and are not unique. In birefringent media, the two polarization modes have in general different refractive indices. The mode with the greatest index of refraction is called the slow eigenmode (because it has the least phase velocity), and the fast eigenmode has the lowest refractive index for that particular propagation direction. The polarization modes of a birefringent medium are degenerate only when the beam propagates in a direction parallel to an *optic axis*. Uniaxial crystals have a single optic axis which coincides with a crystal axis. Biaxial crystals have two optic axes that lie in the plane of the principle axes of the least and greatest index of refraction. Any other propagation direction has

two unique, orthogonal polarization modes. A wave entering the crystal with one of these polarization directions, will keep its polarization state while propagating through the crystal. Any monochromatic electromagnetic wave propagating through a birefringent material can be decomposed into a linear superposition of these two eigen-polarizations. In a uniaxial crystal, one of the polarization modes will always be parallel to the electric field, termed the ordinary polarization (or o-wave). The orthogonal polarization with nonparallel $\hat{d}$ and $\hat{e}$ is called the extraordinary polarization (or e-wave). If the beam propagates in one of the principal planes of a biaxial crystal, but not parallel to an optic axis, one polarization mode will be parallel to the electric field (ordinary), and the orthogonal polarization will be nonparallell (extraordinary) as in a uniaxial crystal. For other propagation directions, both polarizations will be extraordinary.

Finding the indices of refraction of both polarization modes for different propagation directions is important in nonlinear frequency conversion because it may facilitate high conversion by way of phase matching. Phase matching is discussed in Section 2.5. Finding the index of refraction for a given propagation direction is described in textbooks [39, Chapter 14], [33, Chapter 4], [37, Section 2.3].

Poynting vector walk-off

Second order nonlinear effects take place in materials without inversion symmetry, most of which are birefringent. In such materials, the index of refraction depends on the state of polarization and propagation direction. The propagation direction in a crystal is often specified relative to the crystal axes by polar (θ) and azimuthal (ϕ) angles. The propagation direction inside the birefringent material is important for appropriate manufacturing of the crystal. An example of a crystal cut for normal incidence for propagation direction $\theta \simeq 45°$ and $\phi = 0$ is shown in Figure 2.1. As discussed above, $\hat{d}$, $\hat{h}$ and $\hat{u}$ form an orthogonal right-handed coordinate system. What's more, the electric field $\hat{e}$ lies in the plane spanned by $\hat{d}$ and $\hat{u}$, (2.13), thus $\hat{e}$ can be written:

$$\hat{e} = a\hat{d} + b\hat{u} \tag{2.14}$$

Here, a and b are constants subject to the condition $a^2 + b^2 = 1$. Hence, $\vec{E}$ is in general not perpendicular to $\hat{u}$, as illustrated in Figure 2.2. The energy flow, expressed by the Poynting vector $\vec{S} = S\,\hat{s} = \vec{E} \times \vec{H}$ is therefore in general not parallel to the direction of propagation:

$$\hat{s} = \hat{e} \times \hat{h} = \left(a\hat{d} + b\hat{u}\right) \times \hat{h} = a\hat{u} - b\hat{d}$$

The walk-off angle ρ is the angle between the propagation direction and Poynting vector $\hat{s} \cdot \hat{u} = a = \cos\rho$. This is the same as the angle between the displacement

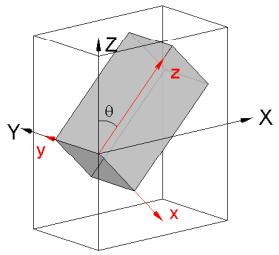

Figure 2.1: Illustration of (for example a uniaxial) crystal with faces normal to propagation direction with polar angle $\theta \simeq 45^o$ and $\phi = 0$ relative to the crystal axes (X, Y, Z). A beam propagating in the z-direction has eigen-polarizations parallel to the x- (e-wave) and y-axes (o-wave).

and the electric field vectors, see (2.14): $\hat{d} \cdot \hat{e} = a$. The Poynting vector of the e-wave will "walk away" from the propagation direction $\vec{k}$ as it propagates through the anisotropic medium by the walk-off angle ($\rho \sim 0 - 4°$ depending on propagation direction, for common nonlinear crystals [40]). Depending on their directions of polarization, two beams propagating in a crystal will experience different walk-off angles, hence limit the practical interaction length of a nonlinear process. (Ordinary beams have no walk-off). Narrow beams will have shorter interaction length than wider ones.

If walk-off and nonlinear interaction takes place simultaneously, the phase-fronts become correlated when they "slide" across each other as they propagate through the crystal. The latter effect is of particular importance in the context of this thesis. In many OPO applications, walk-off limits the interaction length because of narrow beams. In such situations, walk-off can be mitigated by the use of one or more walk-off compensating crystal pairs [41], in which the second crystal is oriented such that the walk-off between the interacting waves is reversed.

Spatial walk-off should not be confused with temporal walk-off, which is the loss of temporal overlap between to pulses caused by group velocity mismatch between the pulses.

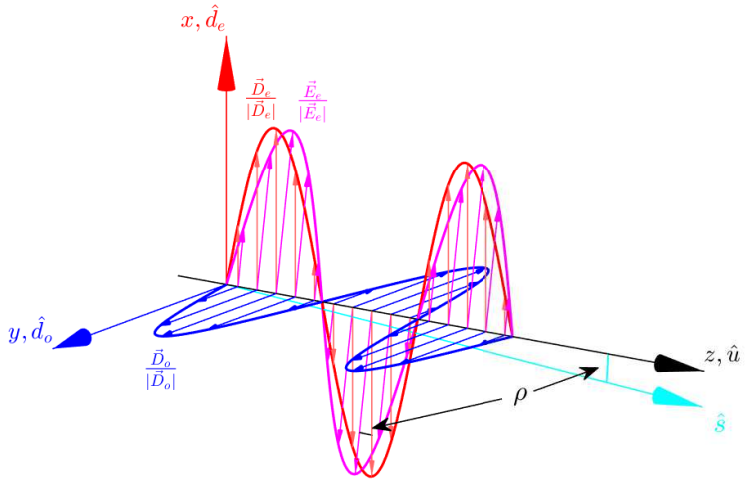

Figure 2.2: Eigenpolarization directions of electric and displacement fields in a uniaxial crystal. The propagation direction $\hat{u}$ forms an angle θ with the crystal Z-axis, see Figure 2.1. The ordinary eigenpolarization $\hat{e}_o$ (blue) is parallel to $\hat{d}_o$ and behaves as if travelling in an isotropic material. The extraordinary eigenpolarization with electric field vector $\hat{e}_e$ (magenta) forms an angle ρ with $\hat{d}_e$ (red), as $\hat{e}_e$ has a component in the propagation direction $\hat{u}$. The Poynting vector (direction $\hat{s}$) walks off from the propagation direction $\hat{u}$ also with angle ρ.

2.3.3 Nonlinear media

In nonlinear media, the polarization has additional (nonlinear) components, $\vec{P}^{\mathrm{NL}} = \chi^{(2)} : \vec{E}\vec{E} + \cdots$. $\chi^{(2)}$ is of special interest in the present work. In the nonlinear case, the wave equation for the electric field becomes inhomogeneous, driven by the nonlinear polarization components:

$$\left(\nabla \times \nabla \times + \frac{1}{c^2}\frac{\partial^2}{\partial t^2}\epsilon\right)\vec{E} = -\mu_0 \frac{\partial^2}{\partial t^2}\vec{P}^{\mathrm{NL}} \tag{2.15}$$

We find some interesting features of the inhomogeneous wave equation by considering its driving terms. The electric field can in general be written as a sum of its frequency components:

$$\vec{E}(\vec{r},t) = \sum_n \vec{E}_n(\vec{r})e^{-i\omega_n t} + cc$$

Including only the second order susceptibility $\chi^{(2)}$, when the argument of $\vec{E}(\vec{r})$ is omitted the nonlinear polarization reads:

$$\begin{aligned}\vec{P}^{\mathrm{NL}} &= \chi^{(2)} : \left[\sum_m \left(\vec{E}_m e^{-i\omega_m t} + cc\right)\sum_n \left(\vec{E}_n e^{-i\omega_n t} + cc\right)\right] \\ &= \chi^{(2)} : \left[\sum_{m,n}\left(\vec{E}_m\vec{E}_n e^{-i(\omega_m+\omega_n)t} + cc + \vec{E}_m\vec{E}_n^* e^{-i(\omega_m-\omega_n)t} + cc\right)\right]\end{aligned}$$

Assuming the input consists of two monochromatic waves of different frequencies $\omega_2 \neq \omega_1$ we get:

$$\begin{aligned}\mathbf{P}^{\mathrm{NL}} = \chi^{(2)} \quad : \quad & \left[\underbrace{\vec{E}_1\vec{E}_1^* + \vec{E}_2\vec{E}_2^*}_{\text{Optical rectification}} + \underbrace{\vec{E}_1\vec{E}_1 e^{-i(2\omega_1)t} + \vec{E}_2\vec{E}_2 e^{-i(2\omega_2)t}}_{\text{Second harmonic}} + cc\right] \\ +2\chi^{(2)} \quad : \quad & \left[\underbrace{\vec{E}_1^*\vec{E}_2 e^{-i(\omega_2-\omega_1)t}}_{\text{Difference frequency}} + \underbrace{\vec{E}_1\vec{E}_2 e^{-i(\omega_1+\omega_2)t}}_{\text{Sum frequency}} + cc\right]\end{aligned}$$

This means that two monochromatic beams of different frequencies can interact via second order nonlinear polarization to give rise to beams with frequency components at the second harmonic, the sum and difference of the two input frequencies in addition to a nonradiating DC electric field, called optical rectification. These are the four basic process when two monochromatic waves of different frequencies interact by second order nonlinear polarization. Optical

rectification is used in electrooptical and magnetooptical modulation of light [9, Chapter 4] and nonlinear generation of THz-radiation [42].

In a real scenario, however, the input often consists of a set of beams with given frequencies and narrow frequency bandwidth. In principle, the nonlinear polarization has frequency components at all combinations of any of the frequency components. However, in practical devices only one of the above mentioned polarization components couples to the other waves to generate a macroscopic field of interest. This is tied to the conservation of momentum, which is termed wave vector or phase matching, which will be discussed in Section 2.5. Phase matching is normally achieved by precise orientation of the propagation direction in a nonlinear crystal for beams with a given set of frequencies.

In the next section we assume two monochromatic waves that interact via difference frequency polarization to generate a third wave.

2.4 Coupled wave equations for difference frequency generation

In this section we find the coupled wave equations by considering the difference frequency polarization only. We have chosen DFG as an example because this is the most important case for the reported work. The coupled equations for SFG and SHG can be derived in the same manner.

By convention we assume $\omega_1 < \omega_2 < \omega_3$. Further, we assume two continuous wave, monochromatic input beams with $\vec{E}_1(\vec{k}_1, \omega_1)$ and $\vec{E}_3(\vec{k}_3, \omega_3)$. The wave equation has to be satisfied for all frequency components separately (ω_1, ω_3 and the difference frequency component ω_2). SHG, SFG and optical rectification are neglected. Omitting the argument of the fields ($\vec{E}_i = \vec{E}_i(\vec{k}_i, \omega_i)$), the set of wave equations (2.15) can be written:

$$\begin{aligned}
\left(\nabla \times \nabla \times - \frac{\omega_1}{c^2}\epsilon\right) \vec{E}_1 &= \frac{\omega_1^2}{c^2}\, \chi^{(2)}(\omega_1 = -\omega_2 + \omega_3) : \vec{E}_2^*\, \vec{E}_3 \\
\left(\nabla \times \nabla \times - \frac{\omega_2}{c^2}\epsilon\right) \vec{E}_2 &= \frac{\omega_2^2}{c^2}\, \chi^{(2)}(\omega_2 = \omega_3 - \omega_1) : \vec{E}_3\, \vec{E}_1^* \\
\left(\nabla \times \nabla \times - \frac{\omega_3}{c^2}\epsilon\right) \vec{E}_3 &= \frac{\omega_3^2}{c^2}\, \chi^{(2)}(\omega_3 = \omega_1 + \omega_2) : \vec{E}_1\, \vec{E}_2
\end{aligned} \tag{2.16}$$

We assume solutions of the same kind as discussed in the linear medium case, however we need to include several beams. The factors $\mathcal{E} = \mathcal{E}(\vec{r}, t)$ of the electric fields are now slowly varying (as compared to the optical variation) quantities in space and time. Furthermore, we assume that the waves are linearly polarized, transverse infinite plane waves travelling in the z-direction incident on a nonlinear medium, $\vec{k} = k\hat{e}_z$. The electric field can thus be written

$\vec{E} = \sum_n \mathcal{E}_n(z)\hat{e}_n e^{-(i\omega_n t - k_n z)}$. The transverse infinite plane wave assumption implies that the divergence of the electric field vanishes, and $\nabla \times \nabla \times = \nabla^2$, the Laplacian. ($\nabla \cdot \vec{E}$ is often negligible compared to the Laplacian in nonlinear optics [11, Section 2.1].) In our case the Laplacian can further be replaced by d^2/dz^2, and the first term of the wave equation can be written:

$$-k^2 \frac{d^2E}{dz^2} = \mathcal{E}'' e^{-i(\omega t - kz)} + 2ik\mathcal{E}' e^{-i(\omega t - kz)} - k^2 \mathcal{E} e^{-i(\omega t - kz)}$$

Here, prime denotes differentiation with respect to z. The first term on the right hand side can normally be neglected. This is called the slowly varying amplitude approximation, which means that the amplitude of the electric field varies slowly compared to the optical wavelength, $\mathcal{E}'' << k\mathcal{E}'$.

Inserting into (2.16), the wave equation for frequency component ω_n becomes:

$$\left[ik_n\mathcal{E}_n' - k_n^2\mathcal{E}_n + \frac{\omega_n^2}{c^2}\epsilon\mathcal{E}_n\right] e^{-i(\omega_n t - k_n z)} =$$
$$-\frac{\omega_n^2}{c^2}\chi^{(2)}(\omega_n, \omega_k, \omega_l) : \mathcal{E}_k\mathcal{E}_l e^{-i[(\omega_k+\omega_l)t - (k_k+k_l)z]}$$

$|k| = n\omega/c$ and $n^2 = \epsilon(\omega, \vec{k})$. n is the refractive index for a wave of frequency ω travelling in the $\vec{k}$-direction. When this is inserted into the equation, the two last terms on the left hand side cancel. The coupled equation for the electric field of the mixed frequency component is thus:

$$\begin{aligned} ik_2\mathcal{E}_2' e^{-i(\omega_2 t - k_2 z)} + cc &= -\frac{\omega_2^2}{c^2}\chi^{(2)}(\omega_2, \omega_3, -\omega_1) : \mathcal{E}_3\mathcal{E}_1 e^{-i[(\omega_3-\omega_1)t - (k_3-k_1)z]} + cc \\ ik_2\mathcal{E}_2' e^{-i\omega_2 t} &= -\frac{\omega_2^2}{c^2}\chi^{(2)}(\omega_2, \omega_3, -\omega_1) : \mathcal{E}_3\mathcal{E}_1 e^{-i(\omega_3-\omega_1)t} e^{i(k_3-k_1-k_2)z} \end{aligned}$$

Evidently, $\omega_2 = \omega_3 - \omega_1$, which means that the energy of the process is conserved as described below. $\Delta k \equiv k_3 - (k_2 + k_1)$ is called the phase mismatch. The equations for the other two frequency components are similar, and we have a set of coupled equations:

$$\begin{aligned} \frac{\partial\mathcal{E}_1}{\partial z} &= i\frac{\omega_1}{n_1 c}\chi_{\text{eff}}\mathcal{E}_3\mathcal{E}_2^* \exp(i\Delta k z) \\ \frac{\partial\mathcal{E}_2}{\partial z} &= i\frac{\omega_2}{n_2 c}\chi_{\text{eff}}\mathcal{E}_3\mathcal{E}_1^* \exp(i\Delta k z) \\ \frac{\partial\mathcal{E}_3}{\partial z} &= i\frac{\omega_3}{n_3 c}\chi_{\text{eff}}\mathcal{E}_1\mathcal{E}_2 \exp(-i\Delta k z) \end{aligned} \tag{2.17}$$

In (2.17), χ_{eff} is the effective nonlinear susceptibility [11, Section 1.5]. (2.17) implies that the conversion is most efficient when $\Delta k = 0$, which is called perfect phase matching.

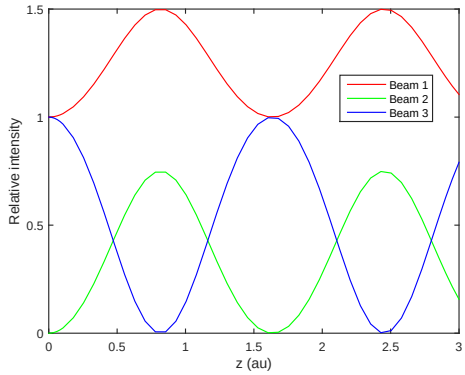

Figure 2.3: Illustration of energy transfer between the waves for a perfectly phase matched DFG-process with two input waves. Once the pump (beam 3) has been depleted, it is regenerated by the reverse process. Intensities and propagation distance z have been normalized.

From (2.17) we see that both the amplitudes and the phases of all three beams determine the energy transfer between the different frequency components. If two beams with significant amplitudes are input, the third beam will immediately be generated. When $\mathcal{E}_2(z = 0) = 0$ difference frequency generation will take place. On the other side, if beams of frequencies ω_1 and ω_2 have significant amplitudes, sum frequency generation may take place. The relative phase between the beams, $\Delta\Phi(z) = \arg(E_3) - \arg(E_2) - \arg(E_1) = \Phi_3 - \Phi_2 - \Phi_1 = \arg(\mathcal{E}_3) - \arg(\mathcal{E}_2) - \arg(\mathcal{E}_1) - \Delta kz$ also plays an important role in determining the direction and efficiency of energy transfer. This way $\Delta\Phi$ determines if sum- or difference frequency generation takes place at a given position in the nonlinear medium. This means that if all energy is transferred from one of the beams, the energy starts flowing in the other direction, regenerating the depleted beam, as illustrated for a perfectly phase matched DFG-process in Figure 2.3. This is called back-conversion. Because practical beams normally have nonuniform intensity distribution across the beam, back-conversion starts in the high intensity spots. This has detrimental effect on the beam quality, in addition to reducing conversion efficiency.

2.4.1 The Manley-Rowe relations and energy conservation

Considering the intensity I in terms of photon (N) rates,

$$I_j = \frac{2n_j|\mathcal{E}_j^2|}{Z_0}$$
$$N_j = \frac{I_j}{\hbar\omega_j}$$

by help of (2.17) one finds the Manley-Rowe relations (for details, see [11, section 2.3], [9, section 6.7]):

$$\frac{\partial N_1}{\partial z} = \frac{\partial N_2}{\partial z} = -\frac{\partial N_3}{\partial z} \tag{2.18}$$

which is valid for lossless propagation. The Manley-Rowe relations tell us that the energy flow is conserved and distributed between the three interacting beams. In other words, the photon rate at which ω_3 is destroyed equals the photon rates at which ω_1 and ω_2 are created or vice versa. In other words, a parametric process is able to "split" the most energetic photon into two photons, or "combine" the two lower energy photons into one, $\omega_1 + \omega_2 \leftrightarrow \omega_3$.

2.4.2 Name conventions

The interacting beams

The high intensity input beam is normally termed pump, as it supplies energy to the process. In DFG the lower frequency beams are called signal and idler beams. The beam which is the aim of the application is normally what we call the signal. In this report, we also use the convention $\omega_1 < \omega_2 < \omega_3$.

Optical parametric processes

The applications of second order nonlinear difference frequency processes have different names. If the high frequency beam (ω_3) with a substantial amplitude and one of the low frequency beams (e.g. ω_2) are incident, ω_1 is generated, and ω_2 is amplified. Such a device has been named optical parametric amplifier (OPA). If only the ω_3 beam is input, the two phase matched lower frequency beams can be generated by amplification of spontaneous parametric emission which is initiated by quantum noise, a process called optical parametric generation (OPG), or parametric fluorescence. If an OPG device is placed inside an optical resonator that provides feedback for one or both of the generated beams, we have an optical parametric oscillator (OPO).

2.5 Phase matching

The transfer of energy between the waves of different frequencies depends on the phase mismatch $\Delta\vec{k}$. Consider the process described in (2.17), where the driving terms are proportional to $\exp(-i\Delta kz)$, as the beams propagate through the nonlinear medium of length L. This means that the efficiency of the energy transfer varies as the waves propagate through the nonlinear material. If the mismatch is small, it has low impact on the transfer for small z, but gradually reduces the efficiency of the energy transfer. On the other side, a large mismatch will lead to oscillatory energy transfer throughout the medium. To illustrate the behavior of the coupled equations, we group the mismatch times the crystal length ΔkL in three ranges:

$|\Delta kL| \geq \pi$ The phase matching terms oscillate, which means that the driving term in one position will cancel that in another position. This results in poor energy transition.

$|\Delta kL| < \pi$ The phase matching term does not change sign as the wave propagates through the crystal. The frequency mixing process takes place, however less efficiently than at perfect phase matching.

$|\Delta k| = 0$ Perfect phase matching. Maximal transfer of energy between the beams is achieved at perfect phase matching $\Delta\vec{k} = 0$. Under this condition, the relative phase between the three beams $\Delta\Phi$ remains constant while propagating through the nonlinear medium.

Efficient frequency mixing of a $\chi^{(2)}$ process requires $|\Delta kL| \sim C$, and $C \lesssim \pi$. The value $C = 2.78$ is often used. In the fixed field approximation, i.e. two of the beams have almost fixed amplitudes, the solution of the amplitude of the third beam is proportional to $\frac{\sin \Delta k/2z}{\Delta k/2z}$. At the point $\Delta kz = 0.886\pi = 2.78$, the power is half of what it is at $\Delta k = 0$, see [43, section 2.1.3] for a discussion. A physical interpretation of perfect phase matching, namely $\hbar\vec{k}_3 = \hbar\vec{k}_1 + \hbar\vec{k}_2$ means that the momentum of the process is conserved. However, according to the Heisenberg uncertainty relation, the uncertainty of momentum is inversely proportional to the interaction length ($\hbar\Delta k \propto \frac{1}{L}$) [16, p. 769], thus the importance of phase, or momentum, matching increases with interaction length.

2.5.1 Birefringent phase matching

In birefringent phase matching, the dispersion of the crystal for different combinations of propagation direction and polarization orientation are used to minimize

Table 2.1: Different types of birefringent phase matching [44].

PM type	Polarization		
	ω_1	ω_2	ω_3
1	Slow	Slow	Fast
2	Fast	Slow	Fast
3	Slow	Fast	Fast

the phase mismatch. These properties also allow wavelength tuning and determine the acceptance of variation in a number of parameters such as bandwidth and angle between the interacting waves.

When phase matching is perfect for parallel beams, we have *collinear* phase matching. The interacting waves' propagation vectors have the same direction, and the phase mismatch may be treated as a scalar. The phase mismatch is:

$$\Delta k \equiv (n_3\omega_3 - n_2\omega_2 - n_1\omega_1)/c \tag{2.19}$$

In (2.19), n_i and ω_i are the refractive index and frequency of wave i, respectively, and c is the vacuum phase velocity. In isotropic materials possessing normal dispersion, the index of refraction increases with frequency and (2.19) does not have a solution. Hence perfect phase matching is impossible in this case.

In birefringent materials there are in general two eigenwaves with different states of polarization and different (eigen-) indices of refraction for each direction of propagation, as discussed in Section 2.3. By selecting the fast polarization state for the highest frequency wave, and the slow polarization for one or both lower frequency waves, the birefringence may cancel the dispersion. Perfect phase matching can be attained for appropriate directions of propagation given the set of frequencies. When the propagation direction is not parallel to any of the crystal axes, we have critical phase matching. This allows varying the refractive index of the extraordinary wave in the range between the highest and lowest possible value. It is therefore the most common way to achieve phase matching in birefringent crystals. Different combinations of polarization states of the lower frequency waves, are called type 1,2 and 3 phase matching, according to [44], and is described in Table 2.1. The polarization of the three interacting waves in type 2 phase matching is illustrated in Figure 2.4.

Practical applications often call for the generation or amplification of a beam with a certain frequency, or within a frequency interval. Moreover, usually only a limited number of different pump frequencies are available. Thus in applications of nonlinear frequency conversion, the set of frequencies is normally given. Phase matching this given set of wavelengths may not be possible for any propagation direction, or even several solutions may exist for a given birefringent medium. If

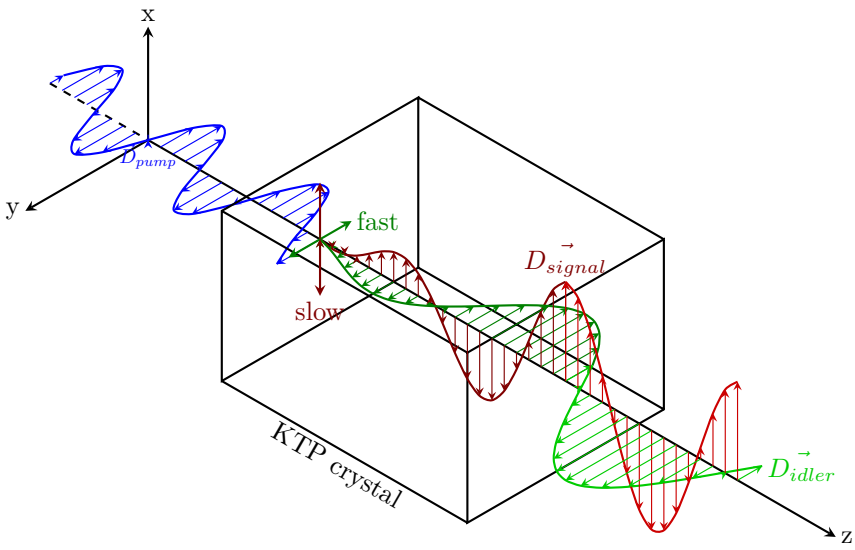

*Figure 2.4: Illustration of linear polarization directions in a type 2 (*fsf*) collinearly phase matched process. Pump (blue) and idler (green) are polarized in the fast direction, signal is polarized in the slow mode. In KTP cut for propagation in the XZ-plane, the fast polarization is the ordinary and the slow mode is the extraordinary. $\vec{D}_{pump}$ is not shown inside the crystal for clarity.*

the phase matching happens to occur for propagation along one of the crystal axes, $\vec{E}$ and $\vec{D}$ are parallel as discussed in Section 2.3.2, thus there is no walk-off between the interacting waves. This condition is satisfied only for a particular set of frequencies for the medium in consideration and is termed noncritical phase matching (NCPM).

Wavelength tuning

The phase mismatch (2.19) depends on a number of parameters, such as frequencies, propagation direction and temperature:

$$\begin{aligned}\Delta k(\omega_1, \omega_2, \omega_3, \theta, \phi, T, ...) = \quad & \tfrac{\omega_3}{c}\, n_3(\omega_3, \theta, \phi, T, ...) \\ & -\tfrac{\omega_2}{c}\, n_2(\omega_2, \theta, \phi, T, ...) \\ & -\tfrac{\omega_1}{c}\, n_1(\omega_1, \theta, \phi, T, ...)\end{aligned} \tag{2.20}$$

In critical birefringent phase matching, the indices of refraction hold the key to how these parameters affect the phase mismatch. Usually, the crystal orientation is changed to perfectly phase match different sets of frequencies, allowing for wavelength tuning of the nonlinear mixing process. The phase matching condition determines frequency bandwidth and acceptance angle for a given pump beam.

In order to tune the wavelength of the nonlinear interaction, it is important to know how the index of refraction varies with wavelength. This is normally expressed in Sellmeier equations which express the index of refraction as function of the vacuum wavelength for each principal axis. Thus for a given set of wavelengths we can solve for the propagation direction which gives perfect phase matching. This is called the phase matching angle, and yields tuning curves for the process in a given crystal. If two waves are incident on the crystal, e.g. in sum frequency mixing, the frequency of the third wave is given, and the crystal must be oriented for optimal conversion. On the other side, if only one wavelength is input, as in an OPO, the two generated frequencies can be tuned according to the phase matching angle without affecting the conversion efficiency, at least in a limited interval. An example of wavelength tuning in a $KTiOPO_4$, potassium titanyl phosphate (KTP) OPO pumped by 1064 nm is given in Section 3.1.1.

Acceptance intervals

The phase mismatch dependency on propagation direction, frequencies, and other parameters, result in a limited tolerance to change in these parameters. Interactions involving two input waves, where the frequency of the third is given by the conservation of energy, responds to changes in these parameters by reduced conversion efficiency due to increased phase mismatch. For interactions with one input wave, on the other side, the frequencies of the two generated waves adapt

to changes by minimizing the phase mismatch as long as the energy is conserved. For example if the crystal in an OPO is rotated in the critical direction, the signal and idler frequencies change to those of the lowest phase mismatch for the new orientation, if phase matching still is possible when the condition $\omega_3 = \omega_1 + \omega_2$ is satisfied.

The tolerance to variations of the paramater p is called acceptance intervals defined as the interval in which the inequality

$$L\,|\Delta k| < 2.78 \tag{2.21}$$

is satisfied. p may be crystal parameters such as orientation or temperature, or beam parameters such as frequency or beam direction. Beam direction tolerance is called acceptance angle and expresses tolerance to divergent or misaligned beams or misaligned crystal. If the parameter is perturbed from perfect phase matcing, Δk may be expanded in a Taylor series:

$$\Delta k(\Delta p) \simeq \Delta k(0) + \frac{\partial \Delta k}{\partial p}\Delta p + 1/2\frac{\partial^2 \Delta k}{\partial p^2}\Delta p^2 + \cdots$$

Expansion to first order is often sufficient. As the phase mismatch multiplied by the interaction length L (normally equal to the crystal length), the acceptance interval is given as a product of p and interaction length L:

$$L\left|\frac{\partial \Delta k}{\partial p}\Delta p\right| = 2 \cdot 2.78 \tag{2.22}$$

p may be perturbed to both greater and lesser values, for example if p is divergence, the inequality (2.21) yields the half-angle. Therefore, when findind the full acceptance interval, the right hand side of (2.22) is multiplied by 2. Acceptance intervals are discussed in more detail in [45, Section 2.14], [46, Section 2.4] and [47]. Calculating the acceptance angle involves non-collinear beams. The scalar assumption (2.19) is no longer valid. Consequently, the vector nature of phase matching has to be taken into account, where both magnitude and direction of $\vec{k}_i$ affect the phase mismatch. Therefore, acceptance angles serve a purpose only when specified along with which beams change direction, which are kept fixed, and if a beam is allowed to adapt in order to minimize the phase mismatch.

Birefringent phase matching requires that the interacting beams have different polarizations. Therefore at least one of the beams normally have walk-off. This means that the beams will walk away from each other as they propagate through the nonlinear material. This will limit the interaction length as the overlap between the fields decreases along the collinear propagation direction, and reduces the acceptance angle as the beams are spatially correlated in the critical plane where walk-off takes place. In the plane wave assumption, a small change of

propagation direction for the ordinary wave leads to increased phase mismatch by changing the direction of its wave vector. The index of refraction of the ordinary wave is unchanged. The refractive index changes marginally for a similar change of propagation direction in the noncritical direction of the extraordinary wave. However, a small change of propagation direction in the critical plane for the extraordinary ray results in considerable change of refractive index. The phase mismatch therefore increases significantly as compared to the the other two cases. The acceptance angle for the extraordinary wave will therefore be narrow in the walk-off plane and wide in the orthogonal plane.

For beams with narrow transverse dimensions, or with more complicated phase structures, the plane wave description fails because each beam contains transverse components of $\vec{k}$. Then the acceptance angle is more appropriately described by walk-off of the extraordinary wave which introduces phase shifts. These phase shifts are connected to the lateral displacement of the structured phase fronts of the extraordinary wave. Assume interacting waves with spherical phasefronts. If the extraordinary wave is tilted towards the walk-off direction, $|\vec{k}_e|$ will decrease. This is equivalent to the plane wave description above, and results in phase shifts associated with the refractive index change. The phase fronts will still be spherical, however the center of curvature will move laterally proportional to the walk-off angle multiplied by the propagation length in the birefringent medium. This will cause additional phase shifts between the extraordinary and the ordinary wave depending on the position in the crystal. Armstrong and co-workers have shown that phase shifts associated with walk-off of the extraordinary wave completely accounts for the effects of acceptance angle [48].

Non-collinear phase matching

When the interacting beams are nonparallel the different $\vec{k}_i$ have to be treated as vectors. At perfect non-collinear phase matching, the transversal parts of the momentum of the two lower frequency beams cancel ($\vec{k}_{1,T} = -\vec{k}_{2,T}$), and their longitudinal sum equals the momentum of the high frequency beam, see Figure 2.5. The interaction length of nonparallel beams is restricted by the angle between the beams, the beam diameter and walk-off. See [37, 43] and references therein for a discussion of non-collinear phase matching.

2.5.2 Quasi phase matching

Other types than birefringent phase matching exist, but are not treated here. In quasi phase matching (QPM) the sign of the effective nonlinearity d_{eff} is flipped (or disrupted) in a regular manner such that the nonlinear conversion does not change direction as the wave propagates through the nonlinear medium. QPM

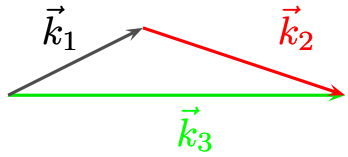

Figure 2.5: $\vec{k}_i$ of perfect non-collinear phase matching.

is less effective than perfect phase matching (by a factor $2/\pi$ [40]). However the conversion may be very efficient because it allows the use of the highest nonlinear coefficient. This is possible because QPM does not require the use of different polarization states for the interacting waves. The highest nonlinear coefficient is often unavailable in birefringent phase matching. QPM is treated in textbooks, see for example [37].

2.6 Optical parametric oscillators

An OPO is basically an OPA placed inside an optical resonator. If the gain of the OPA at the signal frequency is larger than the losses of the resonator, the signal may amplify a microscopic signal initiated from quantum noise to macroscopic levels by multiple passes through the nonlinear medium [49]. Characteristics of OPOs are discussed in [43]. A few of these are particularly important in this work, and they are summarized in the following. The resonator properties will affect the output beams in terms of efficiency and quality. An OPO can be tuned over a range of frequencies and beam directions in the same manner as an OPA as discussed in Section 2.5. No transfer of energy, momentum or angular momentum between the light and material take place in an optical parametric process, thus the response is instantaneous [40]. The pump beam properties and dynamics are therefore closely related to the output waves. Moreover, as discussed in Section 2.3, the output beam quality may be aggravated by back-conversion.

2.6.1 Resonator properties

A linear cavity with two parallel mirrors confining standing optical waves forms the simplest and most compact resonator geometry. Different linear OPOs are illustrated in Figure 2.6. If the ouput mirror reflects the pump beam as well as

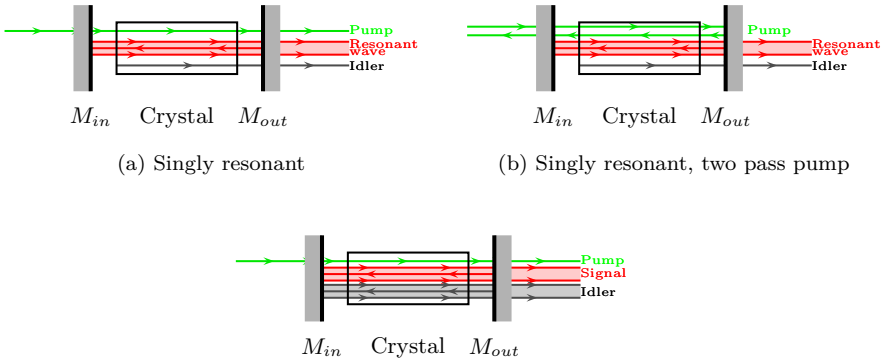

(a) Singly resonant

(b) Singly resonant, two pass pump

(c) Doubly resonant

Figure 2.6: Sketch of OPO linear resonators, M_{in} - input mirror, M_{out} - output mirror.

part of the signal, we have a double pass pump OPO, see Figure 2.6b. A two-pass pump OPO can be beneficial in terms of efficiency, but may cause severe problems with back reflections into the pump laser. Ring resonators comprised of three or more mirrors have a number of possibilities, such as flexibility of outcoupling of different beams at different locations, and out of the plane reflections. However, they are more complex and usually more challenging to align. A ring resonator lifts the need for an optical isolator as two-pass pumping is irrelevant, and reduces the optical fluence within the crystal as the beams pass only once per roundtrip.

OPO resonators can be classified in singly, doubly or triply resonant, depending on the number of resonated waves, controlled by way of the spectral properties of the resonator mirrors. Singly and doubly resonant OPOs are shown in Figure 2.6. Consider a singly resonant OPO (SRO). As parts of the signal are reflected by the cavity mirrors its amplitude grows. The idler on the other hand is coupled out at the mirrors. The idler phase can therefore adapt to the signal and pump phases during each pass through the crystal, effectively leading to a stable OPO. In a doubly resonant OPO, however, the idler amplitude also increases for each roundtrip and the OPO becomes sensitive to small phase changes, such as sub-wavelength changes of resonator length. On the other side, a doubly resonant OPO (DRO) has a significantly lower pump intensity threshold than does an SRO.

2.6.2 Pump sources

The properties of the pump beam are important for the generated beam. The pump pulse duration t_{pump} relative to the OPO resonator rountrip time $t_{\text{roundtrip}}$ determines the mode of operation of the OPO :

$t_{\text{pump}} >> t_{\text{roundtrip}}$: When the pump is CW or the pulse length significantly longer (∼20 ns) than the OPO resonator roundtrip time, the relative pump power is often low. This requires small beams, low losses, DRO (or even triply resonant OPO) and high effective nonlinearity in order for a microscopic signal to grow to macroscopic levels. Typically, CW OPOs use quasi phase matched crystals with high nonlinear coefficient in combination with small beams. Improvements in material science and polishing techniques have resulted in a new class of QPM crystals allowing the use of their highest nonlinear coefficient and long interaction lengths for the generation of CW light, for example periodically poled KTP (PPKTP) [50]. More recently, materials for generation in the UV have been developed [51, 52].

$t_{\text{pump}} << t_{\text{roundtrip}}$: When the pump pulse is significantly shorter than the resonator round-trip time (which is typically several nanoseconds) the OPO is nececarilly synchronously pumped. Such pump sources often have high repetition rates (on the order of 100 MHz), and the OPO resonator length is adjusted to match this. This means that the pump pulse repetition rate is synchronized with the roundtrip time of the resonator, such that successive pump pulses always overlap the signal pulse in the nonlinear medium. Frequency combs are generated by means of ultrafast pulses from synchronously pumped OPOs. Recently, generation of ultrafast pulses in mode-locked CW-OPOs have been demonstrated [51, 53–55].

$t_{\text{pump}} \sim 1 - 10 \cdot t_{\text{roundtrip}}$: When the resonator roundtrip time is on the order of 1/10 of the pump pulse length (this happens for ns-pulses generated by for example Q-switched lasers), the OPO is operated in a transient regime. The power and spatial properties change during the evolution of the pump pulse. The startup time of the OPO should be as short as possible, because the pump power that passes through the nonlinear medium before a significant signal has been generated, remains unconverted. On the other side, high gain and rapid startup results in back-conversion when the pump reaches high powers and the consequence is reduced beam quality and lower conversion efficiency.

This thesis deals with high energy, nanosecond pulses.

2.6.3 Beam quality

Beam quality is defined as the product of the beam width and beam divergence. A laser beam is often compared to a Gaussian (TEM_{00}) beam which is diffraction limited. The figure of merit is the M^2-number defined as:

$$M^2 = \frac{\pi}{4\lambda} \cdot D_0 \cdot \Theta_0,$$

Here, D_0 is the second moment width (4σ diameter) and Θ_0 is the second moment divergence (4σ divergence) of the beam. For details, see for example [56, 57].

In order to minimize the buildup-time, the resonators of nanosecond OPOs are usually made as short as possible. They commonly use plane mirrors, which do not constrain the transverse spatial properties of the generated beam. This means that the nonlinear gain is determined by the transversal profile of the pump beam, which to a large extent determines the output beam quality by gain guiding. However, dealing with high energy nanosecond pulses, optical damage thresholds of the crystal and mirrors of the OPO call for wide beams. Wide beams in short resonators are tantamount to high Fresnel-numbers, thus the resonator does not significantly restrict the divergence of the generated beams, as it supports higher order transverse modes. The beam divergence may be improved by way of resonator modifications, such as unstable or long resonators, variable reflectance mirrors, or other means as will be discussed in Section 3.2. As mentioned previously, back-conversion is detrimental to beam quality. Back conversion is a sum frequency process in an OPO. Sufficient intensities of both idler and signal have to be present in order for back conversion to take place. However, if the intensity of either signal, idler or both is reduced, back-conversion will be hampered and OPO performance is improved. One commonly used way to reduce back-conversion in OPOs is by idler removal. Normally, idler is removed by dichroic mirrors which let the idler out of the resonator. Another way to remove the idler, is by idler absorption in the nonlinear crystal. Under certain conditions this may improve signal beam quality, as was discussed in a paper written in conjunction with the work of this thesis [J2]. A significant part of this thesis has dealt with the mitigation of high divergence following the above described problems of high energy, nanosecond OPOs.

2.6.4 Walk-off in OPOs

For small beam OPOs, Poynting vector walk-off will limit the interaction length beacuse the energy of the extraordinary beam(s) will walk off from the propagation direction. However, for most crystals it is possible to find a crystal orientation that maintains the effective nonlinearity and at the same time reverses the walk-off for most crystals [58]. This is called walk-off compensation. On the

other side, high energy nanosecond OPOs require the use of wide beams to avoid optical damage. Wide beams ensure sufficient overlap between the interacting beams throughout the crystal, and walk-off compensation does not necessarily offer improved conversion efficiency. Poynting vector walk-off correlates the beams spatially as they walk away from each other, in the walk-off or critical plane, thereby improving the beam quality. This effect can be taken advantage of as discussed in [I, II, III]. Temporal walk-off is of little concern in high energy nanosecond pulses.

2.7 Sisyfos - model for numerical simulations

The FFI-developed Sisyfos is a numerical model for simulating optical parametric frequency conversion, lasers and beam propagation in nonlinear or turbulent media, originating from G. Arisholm's Ph.D. thesis [43]. The model accounts for all relevant effects, such as nonlinear interaction, diffraction, and idler absorption [J2]. The beam propagation method is described in [59]. In an OPO, the signal develops from quantum noise, which is modelled semiclassically as equally distributed average complex amplitude per mode [49]. The different frequency components are coupled through the nonlinear polarization, which is computed in the time domain. Sisyfos can also model thermal effects. Sisyfos has proved to compare well with experiments [I, 60, 61]. A tutorial including simulation examples is found in [62].

Throughout this work, Sisyfos was used to establish realistic and reasonable ranges for the different experimental parameters, such as nonlinear material, crystal lengths, mirror reflectivities and geometry of resonators. Furthermore, the simulations were used to narrow parameter space to appropriate experimental conditions with potential for high performance. Simulation results have been incorporated in some of the papers, however far more simulations have formed the basis for the conclusions and experiments presented herein, see e.g. [R3, R4].

Chapter 3

Optical parametric oscillators for high pulse energy

OPOs are suitable for downconverting a pump beam to two beams with lower frequency. The usefulness of the generated beams is largely tied to their beam quality and parameters such as pulse energy and pulse length, depending on the application. The quality of the generated beams is strongly influenced by the quality of the pump beams. However, also the nonlinear interaction itself as well as the geometry of the resonator affect the generated beams. Back conversion can have detrimental effect on the beam quality [J2, 63].

When the OPO process is phase matched, see Section 2.4, the reverse (SFG) process also is, and this process may be strong when the signal and idler beams are intense. Back conversion is therefore a fundamental limitation of conversion efficiency and beam quality. As the pump is depleted, back conversion increases unless either the idler or the signal is removed (or both). The onset of back-conversion is normally nonuniformly distributed across the beam as it depends on the spatial and temporal profiles of the beams. The beam properties of the pump is therefore to some extent transformed to the generated beams, which will be more or less closely related to the quality of pump beam.

Another practical limitation is the optical fluence allowed by the optical components. According to (2.17), energy conversion is proportional to the product of the electric fields. Strong electric fields are therefore beneficial. However, field strengths have to be balanced by the optical damage threshold of the crystal, its coatings or other optical components of the OPO. Reducing the optical fluence

without reducing pump pulse energy or power, can be obtained by increasing the beam width. In practical OPOs pumped by pulses with energy on the order of tens of millijoule and nanosecond duration, the pump beam diameter can be several millimeter across.

The resonator geometry also has impact on the beam quality. Small beam waists can be avoided by use of plane mirror resonators and collimated beams. Furthermore, for the signal to build up to macroscopic levels during the pump pulse, a significant number of signal roundtrips in the resonator is required. Thus nanosecond pulses require short resonators, on the order of 10 cm. A short resonator combined with wide beams have high Fresnel numbers. Therefore, it supports higher order transverse modes with significant divergence, tantamount to low beam quality. The Fresnel number ($F = W^2 n/\lambda L_c$, where W, n, L_c are pump beam radius, refractive index and crystal length, respectively) is merely based on geometric factors. A more detailed analysis of a generic OPO, shows that the Fresnel number should be replaced by an "effective" Fresnel number in which the resonator length is scaled by the number of roundtrips necessary for the signal to build to macroscopic levels [J2]. This means that if the signal uses a substantial part of the pump pulse to grow to a macroscopic level, the signal is influenced by a longer resonator than its geometric length. Consequently, fewer higher order modes are supported than expected by a pure Fresnel number analysis. However, phase matching conditions of the particular nonlinear interaction may come into play. This is what happens in type 2 OPOs which tend to generate beams of asymmetric divergence, as discussed in Section 3.1. Ways to improve the beam quality by mitigating this asymmetry have been demonstrated as discussed in Section 3.2. Our proposed method of orthogonal critical planes OPO (OCP-OPO) as a means to improve the beam quality of high energy nanosecond OPOs, is described in Section 3.2.3. The OCP-OPO represents the major finding of this dissertation, both in terms of effort, publications and usefulness.

The phase mismatch properties of the nonlinear interaction may be used to improve beam quality. However, these means do not directly affect the signal build-up time, which is important regarding conversion efficiency in nanosecond OPOs. This is briefly touched in Section 3.3.

3.1 Beam quality of ordinary OPOs

Simple and versatile OPOs often use critical birefringent phase matching, and the phase mismatch has been minimized for collinear beams. However, the phase mismatch depends on the true experimental conditions, also the actual angle beween (the different parts of) the three interacting beams. If the acceptance angle (see Section 2.5.1) is smaller than the divergence of the modes supported by the resonator, the phase mismatch can restrain the divergence. In critical birefringent

phase matching, the refractive index of the beam with extraordinary polarization changes with the angle between the propagation direction and the optic axis of the crystal. Thus the phase mismatch depends on the divergence not only because of noncollinear (parts of the) beams, but also because the refractive index changes in the plane containing the extraordinary polarization and propagation direction (called the critical plane). Furthermore, if the signal and idler beams have orthogonal polarizations, thus walk-off with respect to each other, their relative phase will correlate spatially in the walk-off direction. This correlation will grow with each pass in the resonator. We have this set of polarizations in type 2 phase matching. Consequently, the divergence in this case becomes asymmetric. The divergence will be limited by the optical resonator in both transversal directions. Secondly, it can be further constricted by the phase mismatch in the critical plane. A quantitative example including calculations regarding a particular nonlinear process is presented in Section 3.1.1. The process is 1064 nm $\rightarrow$ 1700 nm + 2844 nm using an ordinary KTP OPO and type 2 phase matching.

3.1.1 Phase matching considerations in KTP

To quantify the effects discussed above, calculations related to type 2 phase matching in a KTP crystal are presented. The OPO is pumped by a 1064 nm pulsed laser. The propagation direction for collinear phase matching is calcultated in terms of azimuthal and polar angles relative to the crystal axes. Moreover, the phase mismatch is calculated as function of different parameters, which may be varied during experiments. Another important parameter is the value of the nonlinear coefficient, χ_{eff}, which depends on the propagation direction. All calculations are based on Sellmeier equations and the algorithms included in Sisyfos. Second order susceptibility and crystal structure data are retrieved from [11, 45, 64, 65].

The biaxial crystal KTP is orthorhombic and belongs to point group $mm2$. Using contracted notation (see [11, Section 1.5] and the symmetries of this point group, the d_{il} tensor reads:

$$d_{il} = \begin{bmatrix} 0 & 0 & 0 & 0 & d_{15} & 0 \\ 0 & 0 & 0 & d_{24} & 0 & 0 \\ d_{31} & d_{32} & d_{33} & 0 & 0 & 0 \end{bmatrix}$$

Lossless propagation in KTP of the waves involved is a good approximation. Hence Kleinman's symmetry may be employed, i.e. there is full permutation symmetry of the nonlinear coefficients. This leaves only three independent values,

and d_{il} simplifies to:

$$d_{il} = \begin{bmatrix} 0 & 0 & 0 & 0 & d_{31} & 0 \\ 0 & 0 & 0 & d_{32} & 0 & 0 \\ d_{31} & d_{32} & d_{33} & 0 & 0 & 0 \end{bmatrix}$$

The values of the independent coefficients are [64, p. 54]:

$$\begin{aligned} d_{31}(1.0642\ \mu\text{m}) &= 1.4\ \text{pm/V} \\ d_{32}(1.0642\ \mu\text{m}) &= 2.6\ \text{pm/V} \\ d_{33}(1.0642\ \mu\text{m}) &= 11\ \text{pm/V} \end{aligned} \tag{3.1}$$

The coefficients are measured for the process 1064 nm + 1064 nm→ 532 nm. For other sets of waves, with wavelengths closer to a resonance where absorption is not negligible, the coefficients will in general take other values. Otherwise, the coefficients may be scaled using Miller's rule, which is empirical and states that the ratio R between the first and second order susceptibility for a given set of waves is almost constant [11, p. 27].

$$R = \frac{\chi^{(2)}(\omega_1 + \omega_2, \omega_1, \omega_2)}{\chi^{(1)}(\omega_1 + \omega_2)\chi^{(1)}(\omega_1)\chi^{(1)}(\omega_2)} \tag{3.2}$$

Boyd has shown that Miller's rule may be interpreted in terms of a calculation of the nonlinear susceptibility of a classical anharmonic oscillator as a model for noncentrosymmetric materials [11, pp. 21-28]. The coefficients of KTP are not scaled in the current calculations. However, in Section 4.2, the nonlinear coefficients of BBO are scaled using (3.2).

In order to achieve efficient conversion, we want to maximize d_{eff}. Taking the values of (3.1), d_{33} has by far the greatest value. However, d_{33} involves nonlinear interaction with electric field components in the Z-direction for all three waves, which is impossible in collinear birefringent phase matching, and we are left with other tensor components. QPM, however, takes advantage of the often large d_{33}-component. Normally, phase matching a process in one of the principal planes of the crystal axes, XY,YZ or XZ, yields the highest nonlinear coupling. In this case, the effective nonlinear coefficients for propagation in the (θ, ϕ)-direction read [45, p.117]:

$$\begin{aligned} d_{\text{eff}}^{\text{XY}} &= d_{31} \sin^2\phi \ + \ d_{32} \cos^2\phi \\ d_{\text{eff}}^{\text{YZ}} &= d_{31} \sin\theta \\ d_{\text{eff}}^{\text{XZ}} &= d_{32} \sin\theta \ , \theta > V_z \end{aligned} \tag{3.3}$$

In (3.3), V_z is the optic axis. If $\theta < V_z$ we have type 1 phase matching in the XZ-plane. The effective nonlinear coefficients given in (3.3) are plotted for all possible

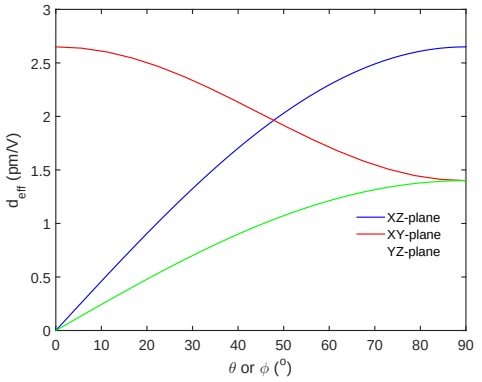

Figure 3.1: Span of possible d_{eff}-values for polarizations according to type 2 phase matching in different crystal planes of KTP.

Table 3.1: Calculated phase matching angles in the crystal planes for type 2 critical phase matching the process 1064 nm $\rightarrow$ 1700 nm + 2844 nm *in KTP [66].*

Plane	θ	ϕ	d_{eff}
XZ	45.7°	0°	1.9 pm/V
YZ	36.7°	90°	0.84 pm/V

values of ϕ and θ in Figure 3.1. Considering the process 1064 nm $\rightarrow$ 1700 nm + 2844 nm and using type 2 collinear critical phase matching, the calculated phase matching angles in the planes of the crystal axes are shown in Table 3.1. Phase matching in the XY-plane ($\theta = 90°$) is impossible owing to the large difference between the principal index of refraction of the Z-direction (n_Z) and both n_X and n_Y, which are shown in Figure 3.2 as function of wavelength. The phase mismatch in the XY-plane is $\Delta k = \frac{1}{c}\left(\omega_3 n_\phi(1064\text{ nm}) - \omega_2 n_Z(1700\text{ nm}) - \omega_2 n_\phi(2844\text{ nm})\right)$. $\Delta k < 0$ for all n_ϕ, which is the index of refraction of propagation direction in the XY-plane ($\theta = 90°, \phi$) and $n_X(\lambda) < n_\phi(\lambda) < n_Y(\lambda)$. The small difference between n_X and n_Y significantly restricts the allowable set of frequencies for type 2 phase matching in the XY-plane. We choose phase matching in the XZ-plane because it allows perfect phase mathching with the highest possible nonlinear coupling.

Collinearly phase matching the process for an arbitrary propagation direction is in general also possible. In that case, both polarization states will have walk-off, and the calculations become more tideous, in particular the evaluation

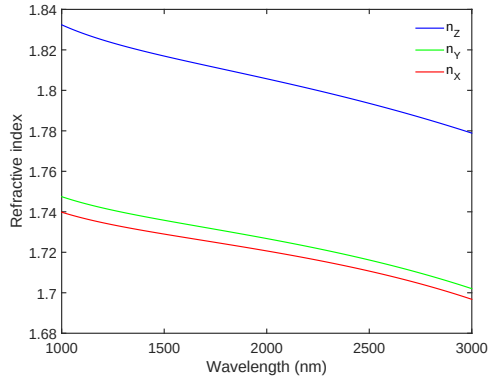

Figure 3.2: Principal indices of refraction for KTP as function of wavelength [66].

of d_{eff}. Explicit expressions of the effective nonlinear coupling for $mm2$ crystals, can be found, e.g. in [45, 67] and references therein. However, these expressions are not exact. On the other side, calculations of indices of refraction for arbitrary propagation direction and thus phase matching angles and associated effective nonlinear coupling are effortless using Sisyfos thanks to its use of tensor notation. For a broader discussion we also include type 1 (ssf) phase matching for the same process. This is possible, although normally not interesting because d_{eff} vanishes in the principal planes [67, section 3.1.7]. However, type 1 phase matching is possible for propagation directions outside the principal planes, if also d_{eff} is nonvanishing. In Figure 3.3, phase matching angles and d_{eff} for type 1 and type 2 phase matching are shown. From this calculation, it is evident that phase matching in the XZ-plane yields the highest nonlinear coupling. Moreover, energy conversion is possible in a type 1 process in propagation directions out of the principal planes.

Assume a KTP crystal is prepared for 1064 nm pumping and phase matched for propagation in the XZ-plane. In an OPO the signal and idler frequencies are allowed to vary freely, so by rotating the crystal with respect to the resonator, another set of frequencies are generated to minimize the phase mismatch. By varying the angle θ or ϕ, we find the wavelength tuning curve, as shown in Figure 3.4. Tuning the polar angle θ, which is the angle between the direction of propagation and the axis of highest refractive index (Z-axis), changes the refractive index of the extraordinary wave significantly. Tuning θ is therefore much more efficient in terms of wavelength shift, than tuning the azimuthal angle ϕ, which is the angle between the crystal axis of lowest refractive index (X-axis)

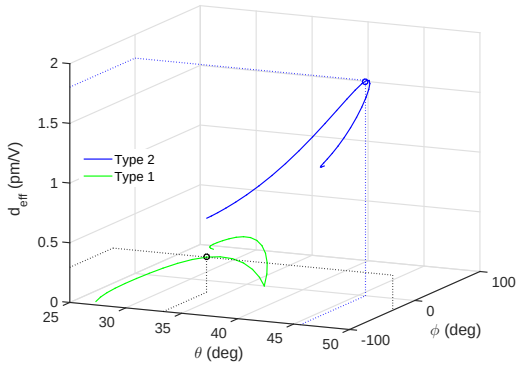

Figure 3.3: Phase matching in arbitrary directions given by azimuthal (ϕ) and polar (θ) angles and the associated nonlinear coupling coefficient, d_{eff}, for the process 1064 nm → 1700 nm + 2844 nm *for type 1, or* ssf *(green) and type 2, or* fsf *(blue) birefringent collinear phase matching.*

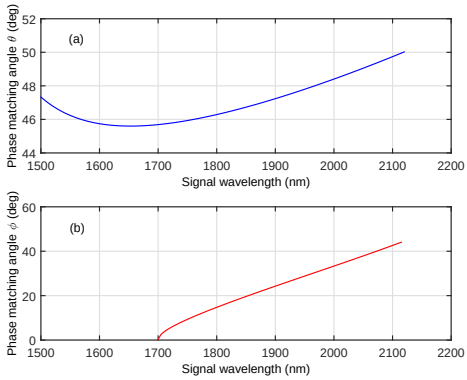

Figure 3.4: Type 2 phase matching angle for different signal wavelengths for the KTP OPO pumped by 1064 nm. *Tuning the polar angle θ, while keeping the azimuthal angle $\phi = 0$ is shown in the top graph, whereas tuning ϕ while keeping $\theta = 45.8°$ is shown in the bottom graph.*

and the projection of the propagation direction in the XY-plane. The latter also changes d_{eff} significantly (see Figure 3.4) because ϕ has to be tuned much more than θ for tuning the wavelength equivalently.

We now consider the beam quality of the resonant (signal) beam in a type 2 collinearly phase matched OPO based on a KTP crystal as discussed above. The beam width is primarily determined by the width of the pump beam. On the other side, signal divergence is determined also by the nonlinear interaction and the resonator geometry. We gain insight into the nonlinear process by studying the phase mismatch $\Delta\vec{k}$. In order to find how $\Delta\vec{k}$ depends on divergence, other parameters have to be defined. The crystal orientation is held fixed with respect to the resonator axis, and the pump parameters and direction of propagation are kept constant. Furthermore, signal and idler wavelengths are held constant, whereas the nonresonant idler beam is allowed to adapt freely to minimize the mismatch. In order to find the divergence of the signal beam, we need to calculate the noncollinear phase mismatch. The resonator can support a certain angular spread in the signal beam, and is not expected to curb signal divergence. The phase mismatch as function of signal beam divergence is shown in Figure 3.5. The divergence can be in either of two orthogonal directions α or β. α is chosen such that it is the same as changing the polar angle θ when the perturbation starts from perfect collinear phase matching. β is the orthogonal direction. For small perturbations around the phase matching angle, α equals changing the polar angle θ and β equals changing azimuthal angle ϕ. The development of the noncollinear phase mismatch, (2.20), can be described as follows. $\vec{k}_p$ does not change, because we have assumed that pump parameters are kept constant. When the azimuthal angle of the signal is changed slightly ($\beta \neq 0$), $\vec{k}_s$ stays almost unchanged because the index of refraction n_s is unchanged for small β. The idler wave compensates the mismatch caused by the angle β between $\vec{k}_p$ and $\vec{k}_s$ by changing its propagation direction in the opposite direction. Neither does n_i change, because the idler angle is also changed in the noncritical direction. The magnitude of the angle is weighted approximately by the ratio between signal and idler frequencies. Consequently, the mismatch stays low for a significant interval (several milliradians) of the angle β. On the contrary, if the signal propagation direction changes in the critical plane $\alpha \neq 0$, n_s changes $|\vec{k}_s|$, because the slow polarization is the extraordinary wave in our case. Moreover, type 2 phase matching implies that the idler is polarized orthogonally to the signal, hence n_i does not change, nor does $|\vec{k}_i|$. As a result, for the same range of phase mismatch the allowable interval of the angle α is much smaller than for β . The same argument is valid for phase matching in materials whose fast polarization is extraordinary, however the roles of signal and idler are interchanged. This means that the allowable divergence in the walk-off or critical plane will be smaller than in the orthogonal transverse direction. From Figure 3.5a, the blue part of

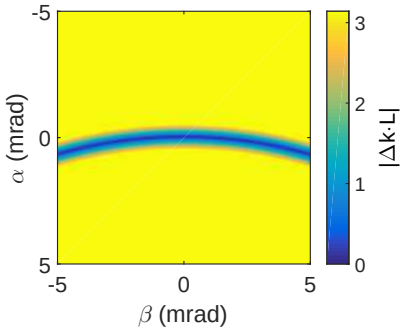

(a) Absolute value of phase mismatch as function of signal divergence.

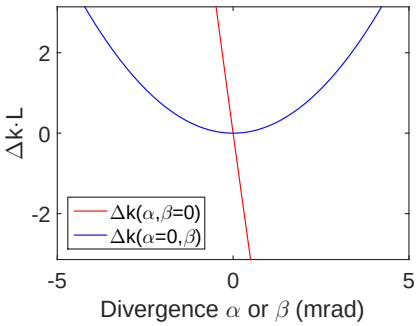

(b) Numerical value of phase mismatch when signal propagation direction deviates from collinear phase matching by angles α (red curve) and β (blue curve).

Figure 3.5: Noncollinear phase mismatch as function of angles α and β. These angles are deviations of signal propagation relative to the propagation direction of perfect phase matching. Perfect phase matching is collinear of type 2 in KTP with $(\theta, \phi) = (45.7°, 0)$. A small α is equivalent to changing θ, and a small β is equivalent to changing ϕ. Signal and idler wavelengths are kept constant, whereas other idler parameters are allowed to vary to mimimize phase mismatch.

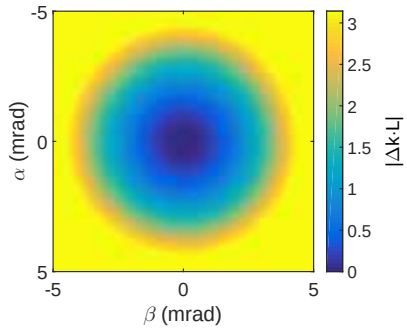

Figure 3.6: Noncollinear phase mismatch as function of transverse directions α and β relative to the propagation direction of perfect phase matching, which is collinear of type 1 in BBO with $\theta = 30.2°$.

the image (low $|\Delta\vec{k}|$) shows this asymmetric phase mismatch which leads to an asymmetric divergence. Figure 3.5b shows phase mismatch as function of α and β separately. The divergence dictates the far field pattern of the beam, which we expect to be asymmetrical in the same manner.

Type 1 vs type 2 phase matching

Type 1 phase matching implies that both the signal and idler are polarized in the slow direction. Assume for now that the slow polarization is extraordinary. Nevertheless, the situation for perturbations in the noncritical direction $\beta \neq 0$ is the same as for type 2 phase matching as was explained above. However, when the propagation direction is perturbed in the critical plane, the idler can compensate the changes of n_s by changing its propagation direction and thereby changing n_i. For example, if α is perturbed such that, n_s increases, n_i will decrease if the idler also propagates in the critical plane however with an angle of opposite sign relative to perfect collinear phase matching ($\sim -\frac{\omega_s}{\omega_i}\alpha$). This way the reduction of $|\vec{k}_i|$ compensates for the increase of $|\vec{k}_s|$ at the same time as the net transverse component of the phase mismatch is reduced, keeping in mind that $|\vec{k}_p|$ is constant. If the slow polarization were ordinary, the perturbations would be in the noncritical plane. Type 1 phase matching for the process in discussion is possible in $\beta - BaB_2O_4$, beta-barium borate (BBO), which is a negative uniaxial crystal, and thus the slow polarization is ordinary. The mismatch as function of divergence is indeed symmetrical as shown in Figure 3.6.

Other mechanisms, such as the resonator geometry and pump beam quality also affect the divergence and hence the beam quality of the generated signal

beam. The effect discussed above is demonstrated in the following subsection, where the results are input and simulated using Sisyfos.

3.1.2 Simulations of an ordinary KTP OPO

A series of simulations of an ordinary OPO was carried out to visualize the effects of the methods addressed above. The results indeed demonstrate the issues regarding beam quality. Parameters of the simulated OPOs are given in Table 3.2 (two 30 mm long KTP crystals were used in a walk-off compensating configuration), and the OPO layout is sketched in Figure 3.7. Walk-off compensation gives higher conversion than equally oriented crystals, but beam quality results are similar.

The pump near and far fields as well as pulse profile, are shown in Figure 3.8. The results in terms of beam quality are shown in Figure 3.9 as M^2 as function

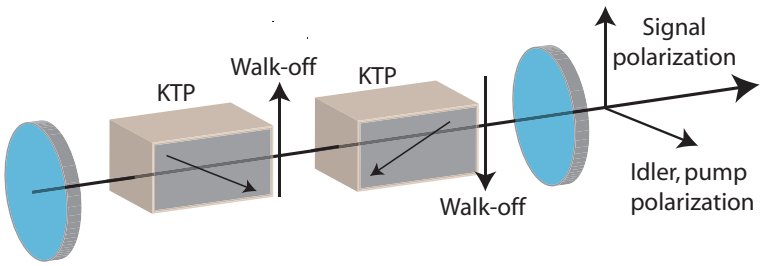

Figure 3.7: Layout of the simulated ordinary OPO with crystals in a walkoff compensated configuration. One of the crystals is rotated by 180° *around the axis of extraordinary polarization (signal wave). The effective nonlinear coefficient will have the same sign, whereas walk-off will be in opposite directions in the two crystals. Arrow on crystal face indicates crystal Z-axis.*

of pump beam diameter for the critical and noncritical directions. The pump fluence was approximately the same in all simulations. The beam quality in the critical direction is good and fairly constant at different Fresnel numbers. In the noncritical direction, however, the beam quality is reduced with increasing effective Fresnel number ($M^2 \propto$ pump beam diameter). The asymmetry is also expressed in the far field irradiation pattern shown in Figure 3.8 (d).

Table 3.2: Parameters used in the simulations.

Pump properties	Value
Wavelength	1064 nm
Spatial profile	Supergaussian order 4
FWHM diameter	0.5-5 mm
Pulse shape	Supergaussian order 2
FWHM pulse length	5 ns
M^2	1.2

OPO parameters		Value
Signal wavelength		1700 nm
Idler wavelength		2844 nm
Air gaps		2 mm
Peak fluence		<2 J/cm^2
Round trip time		0.7 ns
Number of roundtrips during pump pulse		7
Mirror reflectance	input	output
Pump	0	1
Signal	1	0.5
Idler	0.05	0.05

Crystal properties	KTP
Crystal length	2×30 mm walk-off compensating configuration
Walk-off angle	2.3°
Beam with walk-off	slow (XZ)
θ	46°
ϕ	0
d_{eff}	2.6 pm/V

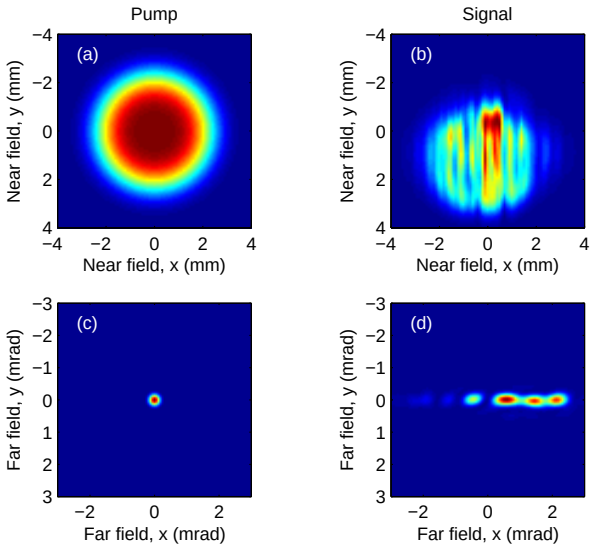

Figure 3.8: Pump beam near field (a) and far field (c), used to simulate the generation of signal near (b) and far (d) fields in an ordinary OPO with two KTP crystals in walk-off compensating configuration.

3.2 Methods to improve asymmetric beam divergence

The problem with high divergence even when pumping with a high quality beam, is limited to the special case of OPOs with a short (∼10 cm) optical cavity and wide beams; in other words for the generation of pulses of nanosecond duration and energy on the order of several tens of millijoule. Moreover, critical birefringent phase matching often leads to an asymmetric far field as discussed above. Nonetheless, such OPOs have important applications in remote sensing, spectroscopy and military countermeasures [63]. Several approaches to evade the problem of asymmetric far field have been demonstrated, see [R4] for a discussion and simulations of various methods. The most important ways to improve beam divergence can be categorized by way of (pump) beam modifications, special (resonator) geometry design, or utilizing certain properties of the nonlinear interaction.

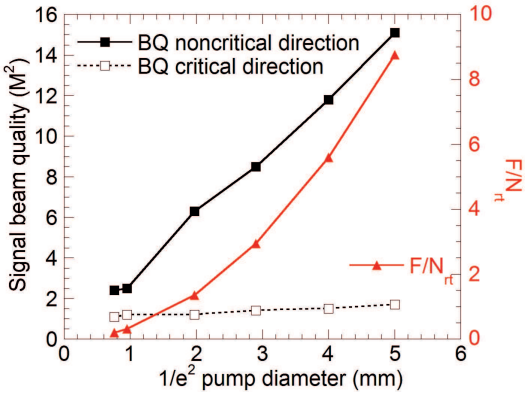

Figure 3.9: Calculated M^2 as function of pump beam diameter (86 % energy in bucket) based on simulation results, showing that the beam quality (BQ) in the critical direction is spatially filtered by the nonlinear interaction. The beam quality in the noncritical plane is determined by the Fresnel number of the resonator scaled by the number of roundtrips necessary for the OPO to reach high conversion, F/N_{rt} following [J2]. The Fresnel number depends on the resonator length and pump beam width, whereas $N_{rt} \simeq 7$ is the number of pump pulse roundtrips in this case. When $F/N_{rt} > 1$, the resonator permits higher order modes. Maximum intracavity fluence was kept between 1.4 J/cm^2 *and* 1.6 J/cm^2.

3.2.1 Pump beam modifications

The quality of the pump beam strongly influences the beam generated by the nonlinear process. Knowledge regarding the nonlinear interaction properties can be used to modify the input pump beam in order to improve the OPO output. For example, a top-hat pump will reduce back conversion compared to a Gaussian pump beam at high pump conversion. Similarly, a smooth single-longitudinal mode (SLM) pulse will more efficiently generate a high beam quality signal than a multi-longitudinal mode (MLM) pump pulse with considerable frequency bandwidth.

More sophisticated yet is the use of an asymmetric pump beam in order to overcome the asymmetric divergence of a critically phasematched nonlinear frequency conversion. If such an OPO is pumped by an elliptical beam, whose ordinary polarization is along the minor semiaxis, it compensates for the larger divergence accepted by the nonlinear interaction in the noncritical plane. The elliptic pump beam should have the same area as the circular pump to keep the fluence at acceptable levels. Such an OPO was simulated, see [R4, Section 4.1.4.2]. To obtain a symmetric divergence, a 2 mm × 20 mm pump beam should be

used. This approach has low practical importance as crystals for type 2 phase matching with 20 mm aperture size are hardly available.

3.2.2 Resonator geometry measures

Methods that improve beam quality by means of resonator geometry, regardless of the phase matching properties, are for example a master oscillator power amplifier (MOPA) and unstable resonators.

Master oscillator power amplifier

The strategy of the MOPA is to generate a signal pulse with high beam quality in an OPO by using a narrow pump beam. The pulse energy therefore has to be low, typically less than 10 mJ is picked off the available pump. The high beam quality signal from the master oscillator is amplified in a subsequent OPA stage using the remaining pump energy and sufficiently wide beams to avoid optical damage. The seed OPO conversion efficiency and pulse energy are less imortant for the total conversion efficiency and the output energy of the MOPA. This method gives good results in terms of beam quality and conversion efficiency at the expense of more optical components and more complicated spatial and temporal alignment. Arisholm *et.al.* demonstrated the conversion of 6 ns pulses at 1064 nm and 500 mJ pulse energy to 138 mJ at 2.1 μm in a beam with M^2=2.3 [63].

Seeded OPO

Instead of using a master oscillator to generate the signal seed, an externally generated seed beam may be used. This is stricly not a geometric measure, however, it is mentioned here as the working principle is equivalent to the MOPA approach. Seeding the OPO with a high quality signal or idler beam, will improve signal beam quality by increasing the gain of the OPO for the modes of high beam quality. A proper seed will also enhance the efficiency of the conversion by shortening signal build-up time. On the other side, a seeded OPO approach also adds complexity. The seed has to be perfectly overlapped with the pump both spatially and temporally, as well as being close to diffraction limited and have sufficient energy. Seeding at signal wavelength means there will be substantial losses as the seed has to enter the OPO through the outcoupling mirror. Simulations of a standing wave OPO seeded at idler wavelength, which may be entered without loss through the input or the output mirror, resulted in a seed requirement of approximatly 5 μJ pulse energy to achieve a near symmetric beam quality [R4]. This would have to be a MOPA system for all practical purposes, however due to

the added complexity of the setup, this method was not pursued in the current work.

Unstable resonator

In an unstable resonator, modes that are close to the optic axis both in terms of position and angle, are stable during many roundtrips. However, transversally offset modes, or rays divergent to the resonator axis, are unstable in the sense that they will propagate out of the resonator after a small number of roundtrips, and this way enhance the beam quality of the output. Unstable resonators are commonly used in high power lasers emitting higher beam quality than would a stable resonator [40]. The magnification in a confocal cavity restricts the divergence, and the well collimated forward pass is suitable for nonlinear conversion. However, the relatively large angular spectrum of the return pass does not allow efficient two-pass pumping when using critical phase matching. Two-pass pumping is often necessary in order to achieve rapid signal build-up time when converting nanosecond pulses [63]. In order to avoid asymmetric divergence, one could possibly use an astigmatic resonator, unstable in only one direction. Simulation results of an astigmatic OPO show that symmetric beam quality is achievable when the magnification is approximately 1.4 in the noncritical direction. However, the conversion efficiency is low because only single pass pumping is possible [R4].

3.2.3 Spatial filtering by way of the nonlinear interaction

In Section 3.1 we looked at collinear type 2 critical phase matching in the much used birefringent material KTP. We saw how the phase mismatch varied when the angle of the signal beam was changed from perfect phase matching. In particular, the phase mismatch increased significantly with the signal beam angle in the critical plane compared to a similar change of angle in the noncritical plane. The coupled wave equations (Equation (2.17) for collinear beams) depend on the phase mismatch, which influences the generated wave. Consequently, the generated signal wave is spatially filtered by way of the properties of the nonlinear material. In our case this means that the divergence will be constricted in the critical plane.

Another way of viewing this spatial filtering, is how the different parts of the signal and idler beams correlate owing to their lateral walk-off, as explained in conjunction with acceptance intervals in Section 2.5.1. The phase between the signal and idler become correlated in the walk-off direction because idler and signal Poynting vectors are nonparallell. The length in which they become correlated will be on the order of the walk-off distance through the nonlinear material. However, in an OPO, multiple passes increase the correlation distance.

This mechanism may be taken advantage of in both transverse directions by rotating the image before each pass through the nonlinear material. This is called intracavity image rotation. If instead the polarizations of the signal and pump beams are rotated, also the critical plane will be rotated, and the effect is the same as in intracavity image rotation. This is the working principle in the orthogonal critical planes OPO. The premise for this effect is lateral walk-off between signal and idler. This is the case in type 2 and type 3 collinear mixing, however type 1 noncollinear mixing also implies walk-off between signal and idler waves.

Intracavity image rotation

Smith and Bowers [68] were the first to suggest to rotate the image of the signal beam within the resonator to improve signal beam quality. They proposed and simulateted a number of different resonator geometries and configurations and explained how different sections of the beam are spatially correlated through intracavity rotations of the beam. This work also led to the development of the rotated-image, singly resonant, twisted-rectangle (RISTRA) OPO, which is commercially available, [69], and described below.

Perhaps the most intuitively comprehensible image rotating OPO, is the OPO which includes an image rotating prism [68]. In a three mirror ring OPO, an image rotating dove prism is placed between two of the mirrors, and rotates the image by 90° for each pass. A half-wave plate in front of the prism rotates the (linear) signal polarization to one of the eigenpolarizations of the prism; and a second half-wave plate after the prism realigns the polarization with that before the first half-wave plate, thus depolarization is avoided. This setup effectively rotates the intensity distribution of the signal beam by 90° for each roundtrip while leaving the polarization state unaltered. The RISTRA cavity is another configuration using image rotation to improve signal and idler beam quality, principally the same as the OPO with an image rotating prism. However, the 90° image rotation per roundtrip is ensured by means of four mirrors forming a nonplanar ring resonator [70]. The RISTRA has the advantages of ring resonators in general, such as reduced feedback into the pump (and seed) laser and lower probability of optical damage as compared to a standing wave resonator. Most importantly, however, are the advantages related to the image rotation; by spatially correlating the signal and idler through signal-idler walk-off, and that the signal beam averages pump beam inhomogeneities both by (signal) image rotation and signal-pump walkoff. The RISTRA geometry also allows a relatively short ring resonator, and its polarization properties allow the use of a half-wave plate. Another advantage is its alignment properties as the cavity is insensitive to mirror tilts. The RISTRA OPO is a ring resonator and two pass pumping is not applicable.

Nabors and Frangineas [71] used non-collinear phase matching in both directions to obtain two-pass pumping, and a Porro prism in the non-critical plane to rotate the image. The BBO OPO was type 1 phase matched, singly resonant and the beam quality improved by a factor of approximately 10 compared to a standard resonator. On the other side, the generated beam had a wide bandwidth.

OPO using orthogonal critical planes

The OPO using orthogonal critical planes is one of the major findings of this work. The OCP-OPO takes advantage of the small accetance angle of signal divergence in the walk-off plane of type 2 phase matching . Spatial filtering is achieved using an OPO configuration which consists of two crystals that have orthogonal critical planes. This can be accomplished in several ways. Perhaps the most intuitive is the use of two identical crystals which are rotated 90° relative to each other about an axis parallell to the propagation direction, and separated by a half-wave plate, as sketched in Figure 3.10. This has to be a half-wave plate at both signal

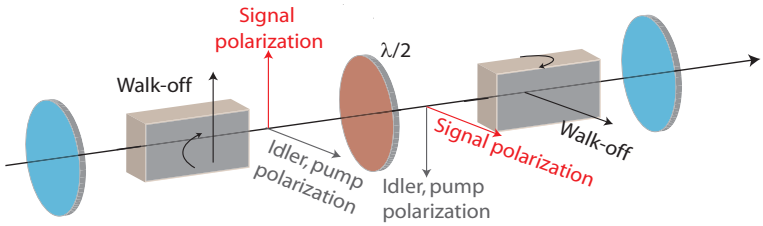

Figure 3.10: Sketch of an OCP-OPO. Identical KTP-crystals separated by halfwave plate and oriented with orthogonal critical planes. Arrow on crystal face indicates rotation for wavelength tuning.

and pump wavelengths, and it has to be oriented to rotate both polarizations by 90°. The idler polarization rotation is of less importance. A poor performance at idler wavelength could also be an advantage as removing parts of the idler wave at the phase matched polarization can reduce back conversion. This OPO can be used with double pass pumping. Keeping in mind the importance of a short resonator for rapid build-up of signal and the quest for high efficiency, a linear, two-pass pumped OPO is preferential. This configuration allows high conversion efficiency by making the resonator short and thus rapid build-up of signal. OPOs using this configuration were demonstrated experimentally in [**III**].

Another configuration of an orthogonal critical planes OPO is by way of two different nonlinear crystals phase matched for the same process, however with orthogonal critical planes. This lifts the need for a multiwavelength half-wave

plate (see Figure 3.10). Such an OPO can be designed even shorter as there is no need for extra cavity-length for the wave plate. On the other side, this configuration requires a pair of crystals which can be phase matched for the same nonlinear process, but with orthogonal walk-off planes. This means that if one of the crystals has walk-off for the slow polarization, the other must have walk-off for the fast polarization. When a suitable crystal pair has been identified, their phase matching angles and the nonlinear coupling coefficients are determined. The final parameter to adjust is crystal lengths. The restriction of the divergence in the critical plane is determined by walk-off in combination with the strength of the nonlinear coupling. The length of one crystal relative to the other should therefore be selected such that a symmetrical far field is obtained. This is easiest achieved with crystals that have approximately the same walk-off angle and d_{eff}. A positive uniaxial crystal and a negative uniaxial crystal have orthogonal critical planes. This is also the case for the combination of the biaxial KTP cut for propagation in the XZ-plane and the uniaxial BBO for a 1064 nm (or 532 nm) pumped OPO for the generation of $\sim$1.7 μm (or $\sim$0.65 μm) pulses. Results from experimental demonstrations and discussion of this OPO configuration were presented in [**I**] and [**II**].

Compared to other methods employed to achieve a symmetrical far field, the main advantage of the orthogonal critical planes method is its compactness and simplicity in terms of the optical path and alignment. Additionally, a linear resonator and thus two-pass-pumping can be used.

Idler absorption

Under certain circumstances, it is possible to take advantage of idler absorption to increase signal beam quality and conversion efficiency in an OPO. The mechanism for the enhanced performance is reduction of back conversion by removing the idler. Idler removal is a known technique, usually implemented by coupling the idler out by means of dichroic mirrors in the resonator. The effect of significant idler absorption in a plane mirror resonator, singly resonant single pass pulsed pump OPO was studied in [J2], triggered by simulations of the OCP-OPO. This paper showed that the signal from such an OPO may have better performance than it would without idler absorption. Both beam quality and signal conversion efficiency could be improved. Idler absorption is of course disadvantageous to the idler beam. Unfavourable thermal effects also come into play at high duty cycles and wide beams. Another important result of this publication was the beam quality dependence on pump pulse length. In particular, an OPO with large Fresnel number may result in high beam quality provided the number of round-trips is comparable to or larger than the resonator Fresnel number in the signal build-up time.

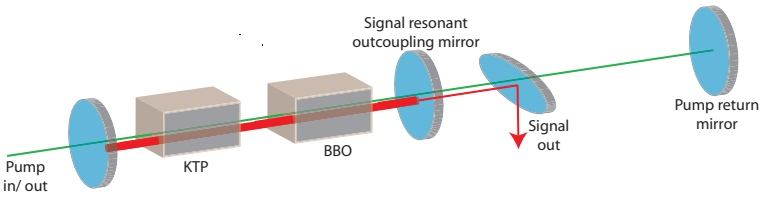

Figure 3.11: Sketch of two-pass pump OCP-OPO using separate pump return mirror. The signal is resonant between the two leftmost mirrors, whereas the pump is returned by a third mirror placed in appropriate distance to the resonator. The signal may be extracted using a dichroic mirror outside the OPO.

3.3 Increased conversion efficiency

For high conversion efficiency of short pulses, the signal has to build rapidly for efficient depletion of the pump beam. The signal growth, proportional to χ_{eff} and the field strengths according to (2.17), is limited by the available nonlinear coefficient on one side, and allowable fluence on the other side. The former is a material property, whereas the latter restrains the maximal permissible pump field strength.

Taking these constraints into account, the most effective way to reduce the build-up time is to seed the OPO as discussed in Section 3.2.2 at the cost of increased complexity. Another approach aiming for rapid signal build-up in a two-pass pumped linear OPO using plane mirrors, is by use of a separate pump return mirror located in appropriate position behind the mirror which couples out the signal, see sketch in Figure 3.11. The method is proposed in [C5]. The idea was to delay the pump return pulse until a macroscopic signal had been developed in the signal cavity due to the forward pump pass, and this way "seed" the backward pump pass. A setup investigating this type of OPO was simulated, and a few experiments were carried out [C5]. Although the experiment was not successful in terms of increased conversion efficiency, simulations predicted a slight benefit using this resonator geometry. The deviation is probably due to lower fluence in the three mirror OPO than in an ordinary OPO when the same beam size is used, because the intracavity fluence decreases when the forward and return pump pulse passes are temporally separated. A smaller pump beam was not tested experimentally. Another interesting effect is that the setup allowed for elongation of the generated pulse, see Figure 3.12. Sometimes it may be helpful to be able to vary the pulse length of an OPO output. This could be the case when sum frequency mixing the output of the OPO with the fundamental or one of the harmonics of a nanosecond laser pulse, because the buildup time of the OPO often becomes a non-negligible part of the pump pulse, meaning the OPO

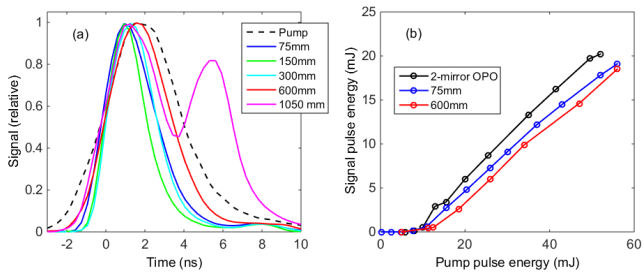

Figure 3.12: Experimental results of three mirror OPO used to elongate the generated signal pulse by delaying the pump return pulse. (a) Measured pulse length for different pump return mirror positions. (b) Signal pulse energy for different pump return mirror positions (from [C5]).

pulse is shorter than the pump.

3.4 Summary

The inherent properties of high energy, nanosecond OPOs lead to high divergence in both or one transversal direction of the signal beam. The high Fresnel number reonator necessary in such OPOs results in resonator modes with high divergence. Walk-off between the signal and idler, for example in type 2 critical birefringent phase matching, restricts divergence in the walk-off plane, and may therefore lead to highly asymmetric beams. The asymmetry in type 2 OPOs can be lifted by several methods, perhaps most prominent by image rotation, or as proposed herein, by introducing orthogonal critical planes using two crystals in the same OPO. Reducing signal build-up time increases the conversion efficiency. Two-pass pumping, a doubly resonant cavity or seeding the OPO will reduce build-up time.

Chapter 4

SFG of high-energy, nanosecond UV-pulses

The work on sum frequency generation (SFG) represents a limited part of this dissertation, with one paper published [**IV**]. Nevertheless, quite a lot of effort was put into the development of a compact, high performance UV source. The subsequent Section presents the background and requirements which lead to the development of a compact, high performance UV source based on SFG in BBO. Section 4.2 considers the phase matching properties of the SFG process, which are important in the selection of appropriate parameters of the device. These parameters were optimized by means of simulations, whose results are given in Section 4.3. The experimental results are summarized in Section 4.4. The experimental results did not quite match expectations based on the simulations. This discrepancy is discussed in Section 4.5.

4.1 Background and requirements

The bioaerosol standoff detection was the driver of the current work. This application required high energy (>10 mJ), nanosecond pulses in the UV around 290 nm delivered in a small cross section up to 1 km away from the instrument. This brightness requirement translates into a beam parameter product of a few millimeter-milliradians. The purpose was to use the UV source in an instrument for field, or "out-of-lab" use, calling for a compact and fairly robust light source. Commercially available sources with appropriate performance in terms of pulse energy and beam quality are offered at the third (355 nm) and fourth (266 nm) harmonics of the Nd:YAG laser. This type of laser is the natural choice of pump

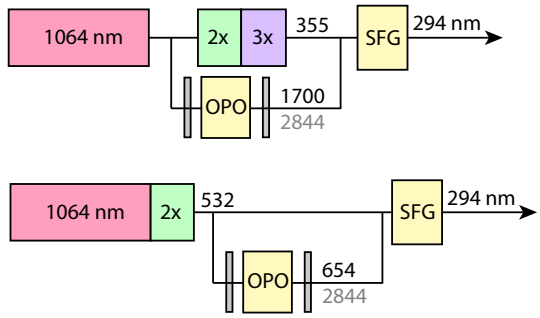

Figure 4.1: The two SFG architectures studied.

for making pulses with several tens of millijoule. Keeping this in mind, the most obvious solution to a 290 nm source was arguably a chain of nonlinear frequency conversion processes. Commercially available laser light sources in this spectral region and relevant published work were reviewed in [R3]. The shortlist of the most promising candidates consisted of:

1. Sum frequency mixing the third harmonic (355 nm) with a pulse around 1.7 μm, which was the signal generated in an OPO pumped at 1064 nm. The available pulse energy at 1064 nm had to be optimally shared between pumping the OPO, and generating the third harmonic.

2. Sum frequency mixing the second harmonic (532 nm) with a pulse around 650 nm, which was generated in an OPO pumped by parts of the second harmonic pulse. All the available laser pulse energy was used to make the second harmonic, which had to be distributed optimally between pumping the OPO and the SFG.

Both approaches aimed at using the very same Nd:YAG laser to pump the harmonic module(s) and the OPO. Subsequently, the two pulses were sum frequency mixed. The two architectures are sketched in Figure 4.1.

The orthogonal critical planes OPO was presented in Section 3.2.3, whereas performance and properties of architecture 1 and architecture 2 OPOs were discussed in **[I, II]**, respectively. The frequency conversion efficiency differs with choice of crystal type and length, phase matching type and pump beam parameters such as beam width. The discussion in [R3] landed on the nonlinear material BBO because the absorption is negligible and BBO has high damage threshold in the wavelength range of interest. In addition, BBO has acceptable nonlinear coupling and is available at moderate cost. Nonetheless, important factors for efficient conversion in terms of pulse energy and beam quality of the UV-beam

are discussed in the following. An SFG process has two input waves, thus there are less parameters available for the optimization of the process than in an OPO. In architecture 1, the properties of the low frequency input wave of the sum frequency mixing (with wavelength 1.7 µm) are determined by the pump laser and the OCP-OPO. The high frequency input wave of the sum frequency mixing (with wavelength 355 nm) is determined by the SHG as well as the third harmonic modules. In architecture 2, both input waves depend on the pump laser and SHG module, which directly determines the high frequency SFG pump (at wavelength 532 nm). The low-frequency SFG pump (at wavelength 650 nm) is influenced also by the OCP-OPO.

4.2 Phase matching considerations for SFG using BBO

When adjusting parameters to optimize frequency conversion, it is important to know the phase matching properties and d_{eff} of the nonlinear material. BBO is a negative uniaxial crystal, thus the index of refraction depends on the polar angle θ of the propagation direction only, and the fast polarization is the extraordinary. However, the nonlinear coupling coefficient d_{eff} depends also on the azimuthal angle ϕ. In line with the discussion in Section 3.1.1, d_{eff} is calculated for the SFG process 1700 nm + 355 nm → 293 nm. The BBO crystal belongs to point group $3m$ [64, p. 5]. Using contracted notation ($d_{il} = \frac{1}{2}\chi_{ijk}$) and symmetry properties for this point group according to Reference [11, Section 1.5] the second order nonlinear susceptibility can be described by the four independent tensor components, d_{15}, d_{22}, d_{31} and d_{33}:

$$d_{il} = \begin{bmatrix} 0 & 0 & 0 & 0 & d_{15} & -d_{22} \\ -d_{22} & d_{22} & 0 & d_{15} & 0 & 0 \\ d_{31} & d_{31} & d_{33} & 0 & 0 & 0 \end{bmatrix}.$$

The values of the independent components are according to [64, 65] and references therein:

$$\begin{aligned} d_{15} &= -0.03 \text{ pm/V} \\ d_{22} &= 2.2 \text{ pm/V} \\ d_{31} &= -0.04 \text{ pm/V} \\ d_{33} &= 0.04 \text{ pm/V} \end{aligned} \tag{4.1}$$

All values were measured for the interaction 1064 nm + 1064 nm → 532 nm. Scaling the coefficients to the frequencies of the current set of waves is carried out according to Miller's rule [11, p. 27]. This is an empirical rule, however proven

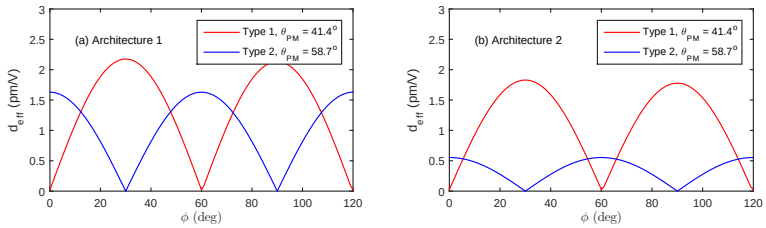

Figure 4.2: d_{eff} for type 1 (ssf) and type 2 (fsf) phase matching in BBO for (a) architecture 1 and (b) architecture 2. Numerical values of the different coefficients are retrieved from [64], and scaled by means of Miller's rule.

Table 4.1: Wave 1 and wave 2 acceptance angles for the different architectures and phase matching types using 5 mm BBO, according to (2.22).

	Architecture 1		Architecture 2	
	Type 1 PM	Type 2 PM	Type 1 PM	Type 2 PM
$\Delta\theta_{\text{wave 1}}$ $(mrad)$	± 1.2	± 9.6	± 0.42	± 4.5
$\Delta\theta_{\text{wave 2}}$ $(mrad)$	± 0.24	± 0.23	± 0.34	± 0.40

to be suitable for KTP, BBO and other commonly used nonlinear crystals by Alford *et. al.* [65]. The calculated values of d_{eff} as function of the azimuthal angle for type 1 and 2 phase matching of the current SFG process are shown in Figure 4.2.

We assume that the two input beams are collinear, and that the crystal is oriented for perfect phase matching. We get a picture of the acceptable divergence of the input beams by calculating the phase mismatch as function of the misalignment of the input beams while allowing the sum frequency beam to adapt freely. Because BBO is uniaxial, divergence in the azimuthal direction does not dramatically increase the mismatch. However, we expect larger mismatch when the beams are misaligned in the polar direction. The non-collinear phase mismatch for type 1 and 2 phase matching are shown in Figure 4.3 for both architectures. The figure shows that significantly less divergence is accepted from the higher frequency wave 2 (laser harmonic), than from wave 1 (OPO signal). This is expected as $\vec{k_2}$ is significantly longer than $\vec{k_1}$. For the same reason, the sensitivity to misalignment will be more similar between waves 1 and 2 in architecture 2. In BBO the fast polarization is extraordinary, thus the generated UV wave is extraordinary for both phase matching types. Because of this, it compensates phase mismatch well by adapting its direction. Using Equation (2.22), we find acceptance angles according to Table 4.1. The table shows that the divergence of the

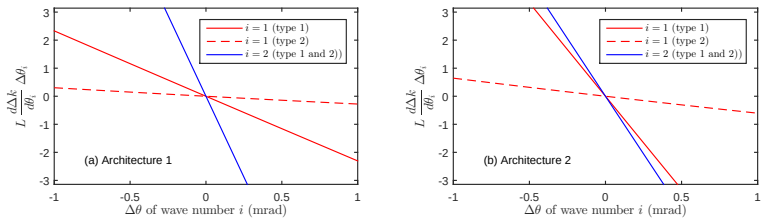

Figure 4.3: Noncollinear phase mismatch for type 1 and type 2 phase matching in 5 mm BBO for the SFG-process of (a) architecture 1, 1700 nm + 355 nm → 293 nm*, and (b) architecture 2,* 654 nm + 532 nm → 293 nm*. The mismatch is shown when wave number 1 is kept in the phase matching direction while wave 2 is varied in the critical direction (blue curves for both phase matching types), and the opposite (red curves). Wave 2 is ordinary irrespective of phase matching type. The generated wave is always extraordinary. It can therefore compensate phase mismatch quite well by adapting direction.*

laser harmonic is more critical than the divergence of the OPO wave. Moreover, the SFG process is more sensitive to high divergence of wave 2 in architecture 1, because this wave has significantly higher frequency than the corresponding wave in architecture 2.

4.3 Simulations

The optical layouts of architecture 1 and 2 are sketched in Figure 4.4. A number of simulations were carried out for both. The results are summarized in [R4]. A short resume of the results is given below. Both architectures were simulated using BBO crystals, cut for type 1 and type 2 phase matching. Type 1 has higher nonlinearity in both cases, see Figure 4.2. Consequently, optimal operation using type 2 phase matching requires longer crystals than type 1 for comparable fluence levels. The simulated outputs of the OPO were used as inputs to the SFG process. The laser beam was assumed to be spatially distributed according to a super Gaussian profile of order four. The temporal profile was assumed to be Gaussian with full width at half maximum (FWHM) pulse length of 5 ns. Both single-longitudinal mode (SLM) and multi-longitudinal mode (MLM) laser pulses, the latter with 20 GHz FWHM frequency bandwidth, were simulated. Whether the pump beam was SLM or MLM was insignificant to the OPO conversion efficiency. This seems reasonable because OPOs operating well above threshold suppress amplitude modulation and are thus prone to produce phase modulated light even when unseeded [72]. However, for the two-beam input SFG, the SLM

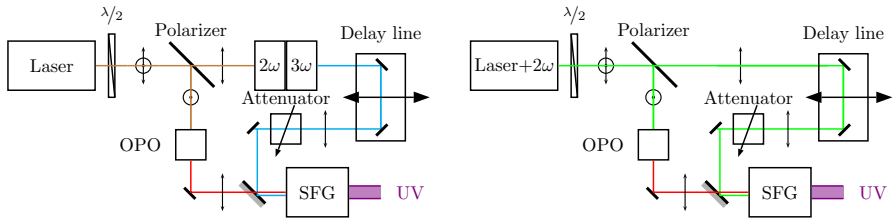

(a) Architecture 1 (b) Architecture 1

Figure 4.4: Sketch of optical layout of (a) architecture 1 and (b) architecture 2. The attenuator consists of a half-wave plate followed by a polarizer, thus the SFG input polarization of wave 2 may be varied by using the appropriate output of the polarizer. Wave 2 pulse may be delayed by moving the mirror assembly closer to or further away from the output of the laser harmonic.

pump performs significantly better. Up to twice the conversion efficiency and beam quality $M^2_{SLM} \sim 2$ compared to $M^2_{MLM} \sim 3$ near maximum conversion was achieved using SLM. It seems reasonable that SLM pumping the system consisting of both an OPO and a sum frequency mixing stage results in higher total conversion efficiency because both pump beams' intensities are more evenly distributed. This is discussed in Section 4.5.

The OPO build-up time should also be considered because the very same laser (or second harmonic) is used to pump the OPO as is used to generate the third (or second) harmonic that is mixed with the OPO signal output. The simulations imply that the harmonic of the pump should be delayed relative to the OPO output before sum frequency mixing; SLM pumping being more sensitive than MLM pumping. Moreover, the longer build-up time of the 1064 nm pumped OPO requires almost 3 ns delay for optimal performance, twice that of architecture 2.

Another important factor for optimal conversion efficiency is the distribution of the laser pulse energy. A total pulse energy of 600 mJ at 1064 nm (or 200 mJ at 532 nm) was available, and distributed optimally between pumping the OPO and for the generation of the high frequency pump beam in the SFG process. The combined maximum intracavity fluence was kept below approximately 2 J/cm^2. The key figures of the best results in the optimization of crystal length are reported in Table 4.2. In practice, the crystal length is selected and by adjusting other parameters, such as beam width and pump energy, a similar conversion efficiency should be within reach.

[1]Total optical conversion efficiency $\eta_{opt}^{arch.1} = \frac{E(SFG)}{E(1064\text{ nm})}$, $\eta_{opt}^{arch.2} = \frac{E(SFG)}{E(532\text{ nm})} \cdot \eta_{SHG}$.

Table 4.2: UV pulse energy and beam quality (BQ) following SFG simulations of different configurations according to [R4]. η_{opt} is the optical conversion efficiency.

	Architecture 1				Architecture 2			
	Type 1 PM		Type 2 PM		Type 1 PM		Type 2 PM	
Simulated UV beam	mlm	slm	mlm	slm	mlm	slm	mlm	slm
Pulse energy (mJ)	55	80	55	75	45	80	45	70
BQ (M^2)	1.5	1.5	1.5	1.5	3	2	3	2
η_{opt} [1]	9%	13%	9%	13%	11%	20%	11%	18%

4.4 Experiments

BBO crystals cut for type 1 and 2 phase matching of both architectures were acquired, see Table 4.3 for phase matching angles and crystal lengths. BBO's low nonlinear coefficient for type 2 phase matching in architecture 2 was compensated for by choosing a longer crystal. OCP-OPOs making use of KTP and BBO,

Table 4.3: BBO crystal parameters used in SFG experiments. d_{eff} calculations according to method described in Section 4.2.

	Architecture 1		Architecture 2	
Type of phase matching	1	2	1	2
Polar angle θ	30.9°	33.5°	41.1°	59°
Azimuthal angle ϕ	90°	0°	90°	0°
d_{eff}(pm/V)	2.2	1.6	1.8	0.5
Crystal length (mm)	5	5	5	10

were used to generate the lower frequency pump wave. The performance of these OPOs in terms of signal pulse energy as function of pump pulse energy are shown in Figure 4.5. Unfortunately, the idler reflection of the resonator mirrors were sufficiently high for the OPOs to run slightly doubly resonant when the laser was seeded for SLM operation. Consequently, the OPOs were sensitive to resonator length changes at sub-wavelength scale, particularly the OCP-OPO pumped at 532 nm. For this reason, only a few SFG results were obtained during SLM pumping, and there is reason to question whether the best possible SFG results were captured. Nonetheless, the SLM experiments gave the best result in terms of UV pulse energy (maximum 32 mJ), which was reported during early stages of the experiments [C6], see Figure 4.6. These results were not published in

[1] $E(1064\text{ nm}) = 600$ mJ and $E(532\text{ nm}) = 200$ mJ, which is low because our laser SHG module was optimized for maximum energy at 355 nm. If it were optimized for SHG, we would expect ~ 350 mJ. A conservative η_{SHG} =0.5 is assumed.

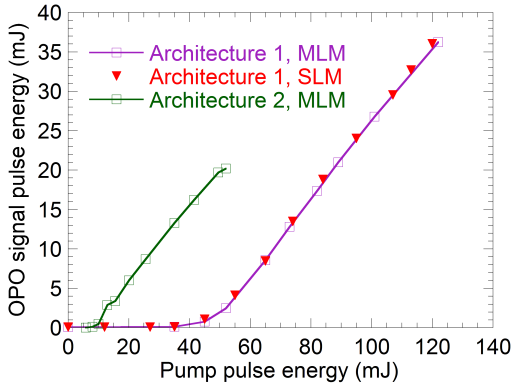

Figure 4.5: Experimental results of OPOs used to generate the low-frequency input wave of the SFG experiments. The slope efficiencies are similar for both architectures ($\eta \sim 0.5$).

paper **[IV]** as we found the output was too unstable, and no more efforts were made to mitigate the double resonance of the OPO. For this reason SLM results for architecture 2 are not reported here. Experimental results were obtained also using type 2 and a combination of type 1 and type 2 phase matching in architecture 1. When combining both phase matching types, the crystals were lined up in the propagation direction. The type 2 crystal was rotated by 90° around the axis of propagation relative to the type 1 crystal. This ensured that the polarization of the lowest frequency wave was phase matched in both crystals, whereas the 355 nm wave was phase matched for orthogonal polarizations in the two crystals. The generated sum frequency beam polarizations in the two crystals were also orthogonal in this configuration. During the experiment, the 355 nm pump polarization was rotated using a half-wave plate to optimize the UV output pulse energy. The performance of these experiments were not as good as expected. They were therefore not published, but are included herein for completeness, see Figure 4.7. Architecture 2 experiments, the generation of UV pulses by mixing 532 nm with 665 nm were also done experimentally for unseeded laser operation only, see Figure 4.7. However, these MLM results should not be compared with the SLM results of architecture 1 in the same figure. The architecture 2 experiments were also acquired at lower OPO output pulse energies and smaller pump beam sizes. The conversion efficiencies as function of pulse energy of wave 2 (i.e. 355 nm for architecture 1 and 532 nm for architecture 2) incident on the SFG crystal for different pulse energies of wave 1 (i.e. OPO signal output) are shown in Figure 4.8. Architecture 1 performs best, and as expected,

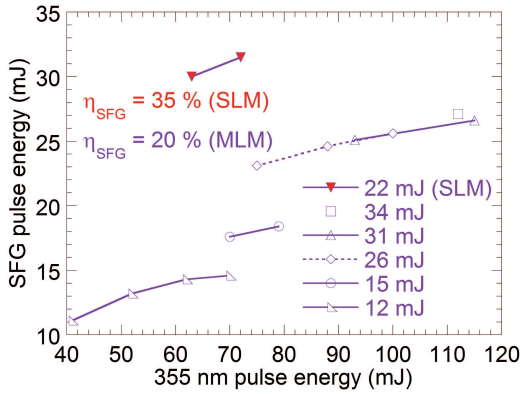

Figure 4.6: UV pulse energy generated under type 1 phase matching as function of 3ω *pulse energy for OPO signal pulse energies of* 12 , 15 , 26 , 31 *and* 34 mJ *(MLM shown using unfilled markers) and* 22 mJ *(SLM shown using red markers). The SFG conversion efficiency (*$\eta_{SFG} = \frac{E_{UV}}{E_{3\omega}+E_{1.7\mu m}}$*) was far better when the laser was operated in SLM than in MLM.*

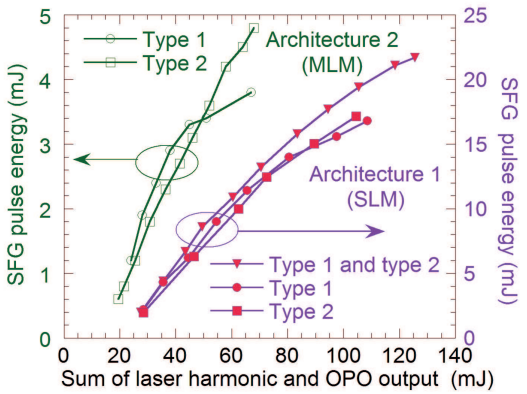

Figure 4.7: Experimental SFG results using BBO crystals according to Table 4.3. Architecture 1 measurements during SLM pumping are shown with purple graphs and markers filled with red. Two crystals for both type 1 and type 2 phase matching were also used successively (see text for details). 22.5 mJ *OPO signal pulse energy was used. Architecture 2 results using MLM pumping and* 17 mJ *OPO signal pulse energy are shown with green curves. Architecture 1 results were acquired during seeded operation of the laser, and are thus not comparable to architecture 2 results captured with MLM operation of the pump laser.*

SLM-pumping is superior.

The experimental results so far were presented as function of the laser harmonic pump pulse energy. This approach is natural because the conversion from the laser fundamental frequency to its harmonics were given by the manufacturer of the laser and harmonic modules. Moreover, the OPO output was given. However, the ultimate key figure is the overall optical conversion efficiency from laser fundamental to UV. Figure 4.9 presents a calculation of total optical conversion. In this calculation, the measured OPO slope efficiency was used. In the estimation of the conversion from the laser fundamental to the third harmonic, a measured slope of approximately 0.3 and zero threshold were used. Our laser was optimized for maximum pulse energy at the third harmonic, thus the second harmonic stage only converts about on third of the laser fundamental. In order to get comparable total optical conversion figures, I have assumed $\eta_{2\omega} = 0.5$. This is a conservative estimate for this type of laser. The specified conversion efficiency for a different commercially available laser is 60 %, the Quantel Q-smart 100 [73]. The best SFG conversion efficiencies that were achieved experimentally

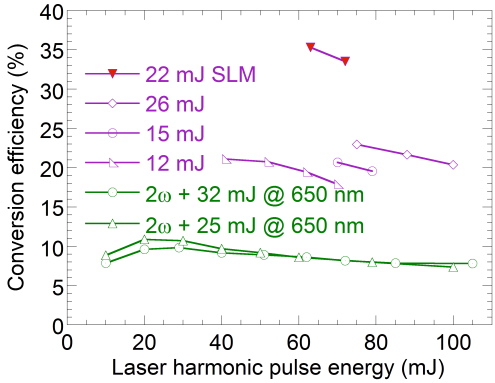

Figure 4.8: Conversion efficiency η from laser harmonic to UV pulse energy as function of laser harmonic pulse energy. $\eta = \frac{E(UV)}{E(harmonic)}$ is shown as function of pulse energy of wave 1. Architecture 1 results are shown with purple curves, and green curves present architecture 2 results. Markers filled with red denote SLM laser operation. All results were obtained during type 1 phase matching.

are summarized and compared to simulations in Table 4.4. The experimental and simulated conversion efficiencies compare acceptably for architecture 1. The conversion effieciency of the architecture 2 experiment was significantly poorer than the simulated, and architecture 2 results were therefore not published. Considering the almost perfect match between simulations and experiments of the OPO,

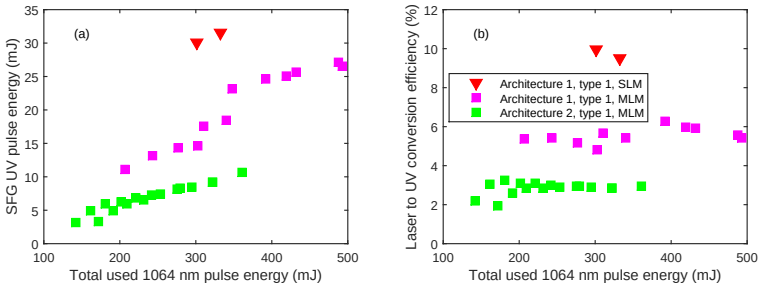

Figure 4.9: (a) Estimated optical conversion from pulse energy at 1064 nm to UV. (b) Corresponding conversion efficiencies ($\eta = \frac{E(UV)}{E(1064\ \mathrm{nm})}$). The best results are presented, and they occured for type 1 phase matching in both architectures. See text for details.

Table 4.4: Total optical conversion efficiencies of the best experimental results compared to simulations. Type 1 phase matching was used for both architectures.

	Architecture 1		Architecture 2
Parameter	mlm	slm	mlm
$\eta_{\mathrm{opt}}^{\mathrm{exp}}$	6%	10%	3%
$\eta_{\mathrm{opt}}^{\mathrm{sim}}$	9%	13%	11%

see [**I**], a discussion of the discrepancy between SFG simulations and experiments is necessary.

4.5 Discussion

The pump laser spatial intensity profile was simulated as a super Gaussian of order four. The time invariant intensity distribution was scaled temporally as a Gaussian pulse. However, the Quantel Brilliant B laser uses an output coupler with a radially variable reflectivity mirror (VRM) with the highest reflection at the center of the VRM. Such lasers are known to have a spatial profile developing throughout the pulse [74], peaking first in the middle and growing radially in a doughnut-shaped manner. This effect will be more pronounced in the harmonics of the laser than in a resonator, because the pump beam passes only once in the harmonic modules. In the two pass pump OPO the pump beam is passed twice and the generated signal has a number of roundtrips during a single pulse. The result is a smoother temporal development of the OPO signal than the harmonics of the laser.

Furthermore, operating the laser in MLM, the natural amplitude modulated beam will result in hot-spots of higher intensities than elsewhere. Conversion in the hot-spot location will be more effective, but back-conversion will start earlier than in areas of lower intensity. These hot spots will amplify during the SHG and SFG stages for the generation of laser harmonics, whereas the effect is somewhat smeared out in the OPO due to the resonator. In the subsequent SFG stage overlap between hot-spots in both pump beams is less likely to occur, thus conversion is expected to be less efficient. Also spatial walk-off will limit the interaction length of the narrow high intensity hot-spot regions [9, p. 84]. See also the discussion in the simulation report [R4, p. 53]. If the real spatiotemporal profile differs significantly from the super Gaussian, these effects may become more pronounced.

Another effect disfavoring architecture 2 is that the OCP-OPO divergence is limited by the nonlinear material walk-off, which scales with the crystal length. The conversion scales with crystal length and frequency, thus architecture 1 requires approximately twice the crystal length of architecture 2. At the same time, the beam quality M^2 is inversely proportional to the wavelength. Recalling the importance of beam quality for conversion efficiency, it is clear that architecture 1 is beneficial if the beam quality restricts the SFG conversion efficiency. However, this is taken into account in the simulations, and can not explain the poor experimental results of architecture 2.

The near and far fields of the laser and its harmonics were measured. The measured irradiance patters of the second harmonic were far from top-hat or super Gaussian. In fact, the third harmonic near field irradiation pattern seemed

to be considerably better than the second harmonic. This is somewhat odd as the second harmonic is used to generate the third. This may be attributed to an optical damage which was found on the input polarizer of the SHG module. It is unknown if this damage was present during the experiments of architecture 1, which were conducted before the architecture 2 experiments.

A combination of these effects most probably gives ground for the low conversion in the case of architecture 2. It was, however out of the scope of this dissertation to quantify these effects by further simulations.

Chapter 5

Standoff detector using UV laser induced fluorescence

For the purpose of detecting biological aerosols dispersed in the air at several hundred meters standoff distance, a handful candidate technologies are of current interest. UV-LIF is held to be one of the most promising techniques [4]. Using a light detection and ranging (lidar) instrument, a short laser pulse is sent towards an unknown target, whose scattered light is collected by the lidar collecting optics. The distance to the target is calculated by measuring the time-of-flight of the light pulse. In a UV-LIF based lidar for bioaerosol detection, a nanosecond laser pulse is fired towards the aerosol cloud, which scatters the light both elastically (i.e. without changing the excitation wavelength) and inelastically (i.e. by absorption and reemitting at a different wavelength). When the scattered light is recollected by the instrument telescope, the elastically scattered part is used to find the distance to and the depth of the aerosol cloud. Both of these parameters are used to set the gating of the detector which captures the inelastically scattered fluorescence signal. The fluorescence signal is analyzed spectrally, and the intention is to discriminate different biological materials.

In this context, the starting point was the biolidar emitting at 355 nm. The experiments carried out and results accomplished with this instrument are described in [J1, C1–C4, R1, R2] and references therein. A short description of the principle of detection is given in Section 5.1 to explain the potentially improved performance using a different excitation wavelength. The lidar instrument with the additional excitation source at a shorter wavelength is briefly described in Section 5.2. Experiments using a standoff detector requires a dedicated test range, which is described in Section 5.3. The results of the comparison between 355 nm and 293 nm excitation are presented and discussed in [**V**], see Section 6.3

and [R5], and is therefore not repeated in the current Chapter.

5.1 Principle of detection

An incident photon absorbed by a moleule may lead to an electron transistion. The relaxation back into the molecule's initial state involves several processes. We have fluorescence when the relaxation process includes the reemission of a photon in combination with nonradiative processes. Thus the emitted photon has lower energy, hence lower frequency than the absorbed photon. The fluorescence depends on the electronic structure, and the fluorescent absorption varies with frequency [75, Chapter 1]. Among the molecules that are typical for biological aerosols, only a few dominate the fluorescence. These fluorophores are tryptophan, which is an amino acid, one of the building blocks of proteins, and NADH which is related to cell metabolism. Other less important fluorophores in this context are flavins and dipicolinic acid [6, 75]. Biological molecules are large and may have complicated structures compared to simpler molecules, like for example those of gases. The cocktail of fluorophores and the structure of the biomolecules and aggregate particles determine the fluorescence spectra of the different biological aerosols. The spectral features of aggregates like bioaerosols are in general coarser than in gases. An analysis of measurements on a number of relevant bioaerosols showed that the 7 nm spectral resolution of the FFI 355 nm lidar was significantly higher than necessary to discriminate these bioaerosols based on the fluorescence spectra [J1]. A dual excitation wavelength lidar would significantly improve the ability to discriminate [76, 77].

In order to optimize instrument design, the detection process should be quantified. The standoff detection system is a lidar, and the lidar equation [78, Section 7.3], [R1] can readily be used:

$$\underbrace{\frac{dE}{d\lambda_{is}}}_{\text{Energy at detector}} = \overbrace{E_0(\lambda_0)}^{\text{Energy delivered}} \cdot \overbrace{\xi(r)\frac{A_0}{r^2}}^{\text{Geometry factors}} \cdot \overbrace{t_{oe}(\lambda_0)t_{oc}(\lambda)}^{\text{Optics transmission}} \cdot \underbrace{t_{ac}(\lambda_0,r)t_{ac}(\lambda,r)}_{\text{Atmospheric transmission}} \cdot \underbrace{\Delta r N_{is}(r)}_{\text{Scatter column}} \cdot \underbrace{\frac{d^2\sigma}{d\Omega d\lambda_{is}}(\lambda_0,\lambda)}_{\text{Scatter properties}} \quad (5.1)$$

In this equation λ_0 and λ are the laser and scattered wavelengths, respectively, r is the distance between the instrument and the aerosols, A_0 and ξ are the area and obscuration factor of the collecting optics. $\Delta r N_{is}$ is the area density of the inelastic scatterers, and the last term is the scattering cross section per solid angle

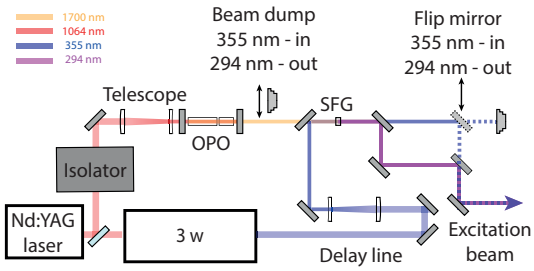

Figure 5.1: Excitation pulse generation with dual wavelength capability. Wavelength selection by flipping mirror and toggling beam dump at the OPO output.

of the inelastic scattering ('is') particles in consideration. Details regarding the different factors are explained in [J1, R1]. In this context we are concerned about the possible improvements by changing the excitation wavelength. First of all, the detected signal will be proportional to the laser pulse energy. Secondly, the atmospheric transmission is wavelength dependent. Finally, the fluorescence cross sections of the interesting biological agents depend on excitation wavelength.

5.2 Selection of excitation wavelength

The excitation source of a biological UV-LIF lidar is normally the third (355 nm) or fourth harmonic (266 nm) of the Nd:YAG laser for convenience; high laser pulse energies are readily available for nanosecond pulse durations. However, mainly two of the noncontrollable factors in Equation (5.1) change significantly in the wavelength interval between 266 nm and 355 nm. As discussed in Section 1.1, the fluorescence cross section of tryptophan peaks around 280 nm, where it is several times higher than at either of the harmonics. Moreover, atmospheric transmission is significantly lower at the fourth than at the third harmonic, in particular when there is ozone in the line of sight. This leads to an optimal excitation wavelength in the $290 - 300$ nm range. Given that we already had a 355 nm instrument, the implementation of a $\sim$ 294 nm source as described in Chapter 4 had small implications on the instrument setup in terms of complexity, because both excitation wavelengths use the same pump laser. At the same time, our spectrograph and camera were suitable also at the shorter wavelength excitation. The additional components for the generation of the shorter excitation wavelength were incorporated such that excitation wavelength could be selected by flipping in a mirror and inserting a beam-dump at the output of the OPO as illustrated in Figure 5.1. Any wavelength around 290 nm would suffice. We ended up with $\sim$ 294 nm as a consequence of the available optical components

Table 5.1: Dual wavelength biolidar key figures.

Parameter	Value	
Excitation wavelength	355 nm	294 nm
Laser pulse length	5 ns	4 ns
Maximum pulse energy	30 mJ	5 mJ
(used in comparative experiment)		
Pulse repetition rate	10 Hz	
Laser beam divergence	0.3 mrad	
Telescope diameter	250 mm	
Telescope field of view	0.8 mrad	
Spectral resolution	7 nm	
Camera minimum gate width	100 ns	
Camera maximum gain	500	

used in the architecture 1 OPO. The main parameters of the dual-wavelength lidar used during the experiments are summarized in Table 5.1. Raman scattering by atmospheric constituents also has to be considered when finding the optimal excitation wavelength. This is particularly important regarding nitrogen which has a Raman shift of 2330.7 cm^{-1} [78], but also water vapour and oxygen Raman shifts have to be assessed. The excitation wavelength should be selected to avoid that the inevitable Raman shifted return disturbs the most important part of the fluorescence spectrum from the bioaerosol being analyzed. This constraint may be regarded once the fluorescence spectra of the bioaersols in consideration are available. For 294 nm excitation, the nitrogen Raman shift peaks at $\sim$ 297 nm, and will not interfere the main parts of the biological aerosol spectra considered in our experiments.

5.3 Standoff detection test range

A semi-closed container system was developed in collaboration between FFI and Totalförsvarets forskningsintitut (FOI), Sweden. The release chamber was a twenty feet long container with built-in walls which had square holes of approximately 1 m^2 functioning as optical apertures. A strong laminar flow was directed from the top of the apertures and collected at the bottom. The collected air was filtered using hepa-filters before being released to the environment. This way a very small fraction of the biological agents that were released inside the container escaped to the surroundings. Also, the laser beam was allowed to pass undisturbed through the aerosol cloud. This is important considering the fluorescence scattering cross section ($\sim 10^{-13}$), which is low even compared to the

returned scattered light from an AR-coated window. The equipment was used in a field trial in Umeå, Sweden. The semi-closed chamber allowed for standoff measurements with controlled biological agent concentration in a well defined depth within the field of view, and compared to reference measurements. The experiments and semi-closed chambers are described in [C3].

A test range located at FFI was prepared. There was a free line of sight between the lidar stand and the semi-closed chamber. The containers were placed more than two hundred meters apart. The release container was equipped with a ventilation duct to reduce the volume that had to be filled with dispersed aerosols. A fan was installed inside the duct to spread the aerosols. Seven different bioagents were disseminated inside the duct, one at a time. An aerodynamic particle sampler (APS) was used for reference measurements, and gave the concentration of particles in size intervals as function of time. Photos of the test range are shown in Figures 5.2 - 5.3. Detailed decription of the experiment and the results thereof are given in Reference [R5] and **[V]**.

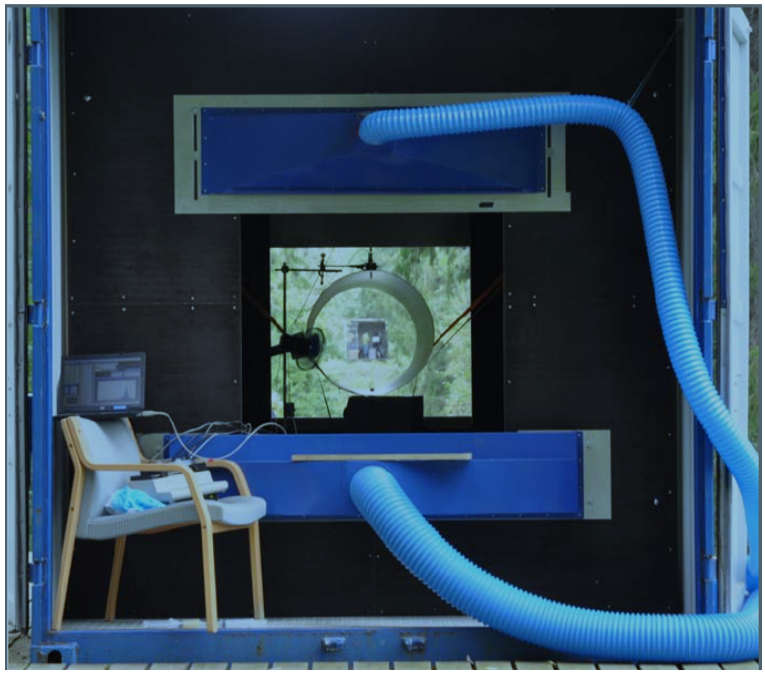

Figure 5.2: The aerosols were released inside the ventilation duct in the release chamber. The laser cross section diameter filled less than a quarter of the diameter of the duct. The air curtains accomodated for a laminar flow across the aperture, confining the aerosols within the chamber without scattering windows in the optical path. The lidar stand can be seen through the ventilation duct along the optical path.

Figure 5.3: The dual wavelength lidar.

Chapter 6

Summary of papers

This Chapter summarizes the papers of this thesis [**I, II, III, IV, V**] and puts them in context. The underlying aim of the work presented herein, was the attempt to build a compact, reliable source, generating high energy UV-pulses with beam quality sufficient to deliver most of the pulse energy within a small solid angle. Moreover, the application requires nanosecond pulse durations. The starting point was therefore to use a single compact laser source with high performance in terms of pulse energy and compactness, and convert the frequency of this laser to the UV region. The selected way of generating UV-pulses was based on a study of state-of-the-art UV-sources as discussed in [R3]. Three of the papers deal with the generation of high quality beams in OPOs with short resonators and wide pump beams [**I, II, III**], and one paper was published on SFG [**IV**]. Another cross-disciplinary paper including an experimental application of one of the proposed UV-sources was published [**V**]. The papers are reprinted in App. I-V.

6.1 OPOs with orthogonal critical planes

Paper [**I**] describes an orthogonal critical planes optical parametric oscillator (OCP-OPO), reached by the use of two different nonlinear crystals, type 2 phase matched for the same process and placed within the same resonator. The essential part of this configuration is to find a pair of crystals that may be type 2 phase matched for the same nonlinear process, and that the signal walk-off takes place in orthogonal planes in the two crystals. In practice, this demands that the extraordinary refractive index is greater than the ordinary in one of the crystals, and vice versa in the second; “positive” and “negative” in terms of uniaxial crystals. A number of possible crystals are found, and essential pa-

rameters retrieved from [45] are listed and compared. Based on the parameter values and material availability, an OPO with $KTiOAsO_4$, potassium titanyl arsenate (KTA) and $\beta - BaB_2O_4$, beta-barium borate (BBO) was realized. KTA behaves as a positive uniaxial crystal when waves of the studied process propagate in the XZ-plane, thus $n_e > n_o$. BBO on the other sida, has $n_e < n_o$ and both crystals may be phase matched for the spectral range in consideration. OPO parameters such as crystal lengths, mirror specifications and pump beam parameters were optimized with respect to beam quality and pulse energy by way of simulations. For a 1064 nm pumped OPO, KTA has significantly higher gain than BBO, which also absorbs somewhat at idler frequencies. BBO's main function in this OPO was to obtain a symmetric far field. This happens when the relative crystal lengths are such that the walk-off is almost the same in both crystals; however this is not trivial, as the spatial filtering induced by signal-idler walk-off depends also on the nonlinear interaction between the waves. In order to get the OPO running, the pump energy was adjusted towards the higher end in terms of fluence level, and the characteristic asymmetric far field of a KTA OPO was observed. Following this, the BBO was angle tuned (in the orthogonal direction of the KTA tuning plane). Once the crystals were phase matched for the same process, the far field shrinked to form a symmetric spot, and the pulse energy increased significantly. This confirmed the effect of the orthogonal critical planes, and that the crystals were tuned correctly. This observation also makes wavelength tuning of this type OPO rather simple. It should be noted that the OPO will easily run with KTA only. On the contrary, an OPO with just the BBO will not run at acceptable fluence levels. A symmetric far field and corresponding beam quality were accomplished. There was excellent agreement between simulations and experiments in terms of beam quality, conversion efficiency and pulse energy. Precursors to this paper were presented at conferences [C7, C8].

In paper [**II**], the results of experiments from an orthogonal critical planes OPO for 532 nm pumping were presented. In these experiments, KTA and BBO cut for collinear critical type 2 phase matching (532 nm $\rightarrow$ 665 nm + 2660 nm) and appropriately coated were used. Because the nonlinear interaction is proportional to the frequencies of the interacting beams, shorter crystals yield the same gain as compared to the OPO pumped at half the frequency. Experiments with KTA only were carried out for comparison, and the results showed favorable beam quality, pulse energy and conversion efficiency in the OCP-OPO. An interesting observation in the laboratory, was made when tuning the crystals to support the same nonlinear process. First, the OPO ran at the process defined by the tuning angle of the KTA. When the BBO was inserted in the OPO, two processes were running simultaneously, easily observed using a spectrometer, which showed two discrete peaks in the spectral domain. At this point, the far field consisted of two discrete spots, even though both crystals contribute to the conversion of the

pump. This happened as the two processes adapted by running in a noncollinear manner. As one of the crystals were tuned to match the process of the other, the two spots in the far field collapsed into one symmetric. Simultaneously, the two signal peaks in the spectral domain also collapsed to form one peak of higher intensity. This observation confirmed that the OCP-OPO was tuned appropriately.

A drawback with the OCP-OPOs described in [**I**] and [**II**] is the need for a pair of matching crystals. The crystal pair has to match not only in terms of orthogonal critical planes, but also have similar walk-off and sufficient nonlinear coupling (d_{eff}). The requirement ties the use of this method to a confined selection of the already limited availability of nonlinear materials. One way to lift this restriction, is to use two identical crystals that are rotated 90° relative to each other in such a way that the critical plane in one crystal is orthogonal to that of the other. However, for the nonlinear interaction to be phase matched in both crystals, the polarizations of the signal and pump waves must both be rotated between the crystals accordingly. A disadvantage is that another component has to be added to the OPO, namely a half-wave plate oriented such that both signal and pump polarizations are rotated by 90°. This method was demonstrated in paper [**III**], by means of two KTP crystals in an OPO for 1064 nm pumping and two BBO crystals in a 532 nm pumped OPO. Commercially available broadband zero-order half-wave plates were used to rotate the polarizations. This method is also beneficial compared to the use of two different crystals, because d_{eff} and walk-off are identical in both transversal directions leaving the OPO with a symmetrical gain. Pulse energies up to 60 mJ at 1600 nm and 75 mJ at 670 nm with symmetrical far fields were observed. Part of this work was presented in [C9].

Another effect demonstrated in paper [**III**] was the beam quality enhancing effect that takes place in OPOs under particular circumstances in combination with idler absorption. This was discussed in other publications [J2, C10]. This came out of the work leading to paper [**I**]. Idler absorption in the crystal removes the idler continuously as it is generated as the beams propagate through the nonlinear crystal. The idler removal prevents, or at least hampers back conversion by reducing idler intensity even when signal intensity becomes significant. In the experiment using 532 nm pumping of an OPO with two BBO crystals, the idler absorption was varied from negligible to significant by wavelength tuning the signal from 700 nm to 650 nm. The beam quality was increased according to predictions presented in [J2].

6.2 SFG of high energy nanosecond pulses

Paper [**IV**] describes the experimental results of the second stage of the nonlinear frequency conversion from the 1064 nm to UV pulses. Sum frequency mixing the

1064 nm pumped OCP-OPO output and the third harmonic of the laser, resulted in a beam with wavelength in the $290 - 300$ nm range. Simulations of the SFG stage formed the basis for the choice of experimental parameters such as nonlinear material and crystal lengths, phase matching, distribution of 1064 nm energy, as well as expected performance at different operating conditions. The simulation results were not part of paper [**IV**].

The experimental results were beneficial in terms of setup compactness in combination with beam quality, as compared to other reported results [79, 80]. The experimental challenges in our setup, including several nonlinear frequency conversion stages, was to achieve a good spatial and temporal overlap between the two beams and pulses to be mixed. This is essential for efficient conversion, in addition to the "usual" requirements of uniform intensity distribution and high beam quality. Another important element of this multiple conversion stage setup, was how to distribute the primary pulse energy at 1064 nm between OPO pump and 3ω generation, and the timing of the pulses. Timing is important as the OPO pulse length tends to be on the order of 0.8 that of the 3ω pulse, which was generated by the commercial harmonic stages (frequency doubling to 532 nm, and subsequent SFG to 355 nm).

Beam widths were adjusted using Galilean telescopes, and optimal temporal overlap was ensured by means of an adjustable delay line, which consisted of two mirrors in the third harmonic optical path. The two beams were combined at a dichroic mirror placed in front of the SFG nonlinear material, a BBO crystal cut for type 1 phase matching.

The experimental results given in paper [**IV**], showed the UV pulse energy output as function of the 3ω pulse energy, for different OPO pulse energies. The experimental results were poor compared to the simulation result, first of all in terms of pulse energy. The discrepancy can be attributed to a number of reasons, as discussed in Section 4.5. The results of paper [**IV**] were nonetheless sufficient to be used in a standoff detection application as discussed below.

6.3 Standoff bioaerosol detection using UV-LIF

Armed with a coherent 294 nm source emitting nanosecond pulses with energy in the millijoule range and high beam quality, the standoff biological aerosol detection application was tested experimentally as described in paper [**V**]. This application was also the main motivation for starting the work presented in this thesis. The contents of paper [**V**] was multidisciplinary. The work spanned from building a breadboard instrument suitable for field use, incorporating the setups described in paper [**I**] and paper [**IV**] into the biolidar based on the third harmonics of the Nd:YAG laser, to preparing biological agents, operating the biological aerosol test range and interpreting spectral data.

The objective of the experiments was to compare 294 nm to 355 nm excitation using UV-laser induced fluorescence (LIF) of standoff biological aerosol detection, under the hypothesis that the shorter wavelength excitation had higher fluorescence cross section for the most interesting biological agents. Before comparing the results, the fluorescence spectra were normalized with respect to aerosol concentration measured by the APS, excitation pulse energy and instrument spectral response. The experimental findings showed that the response was proportional to bio-agent concentration. At low agent concentrations, the Raman scattering of the atmospheric constituents N_2, O_2 and H_2O are strong compared to the fluorescence and therefore influence the fluorescence spectra. The experiments also confirmed the hypothesis concerning the excitation wavelength. In particular, it was found that the biological agents that were simulants for anthrax, which is considered among the most harmful threats, had almost an order of magnitude higher cross section at the deeper UV wavelength. However, more importantly in perspective of biological standoff detection, the fluorescence spectra were profoundly more distinct at 294 nm excitation wavelength than at 355 nm at the instrument spectral resolution ($\Delta\lambda \sim 7$ nm). This finding indicates that more reliable classification can be expected at 294 nm excitation than at 355 nm, see Figure 6.1. Even at 355 nm excitation, reliable classification is possible [C1]. With a compact source e.g. as demonstrated in the experiments, a dual wavelength instrumentent may be implemented with limited extra effort. A biological standoff detector utilizing both excitation wavelengths holds promise for even better performance [76, 77, 81, 82]. At the end of the day, a sufficiently low false alarm rate is the most important instrument parameter from an operational point of view.

The agent fluorescence spectra compared well with other publications, however, these describe single particle fluorescence spectra of close-up measurements, and not standoff detection [81, 83, 84]. The results of paper **[V]** were also presented in the article *Advances in standoff detection make the world safer* in Photonics Spectra [85].

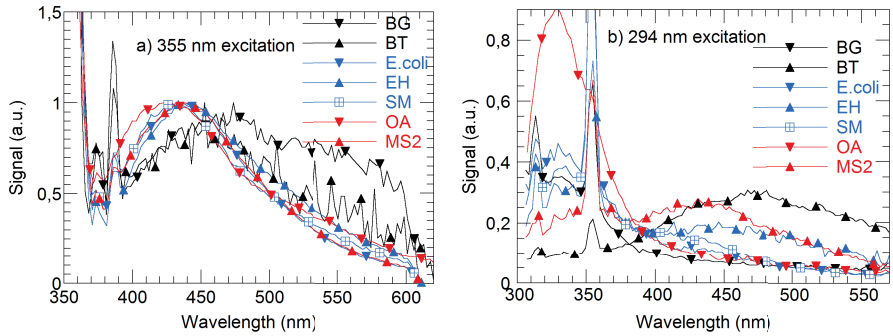

Figure 6.1: Fluorescence spectra following (a) 355 nm *and (b)* 294 nm *excitation for the seven agents used in the experiments (Figure 10 of paper* ***[V]****, see this reference for further explanation).*

Chapter 7

Conclusion

The objective of the work leading to this dissertation was to generate high energy nanosecond laser pulses in the UV spectral region between 280 nm and 300 nm. The application was detection of biological aerosols using UV-LIF at several hundred meters standoff distance. FFI had already built a bioidar with an excitation wavelength of 355 nm. This was achieved using the third harmonic of a commercially available Nd:YAG laser. However, the fluorescence cross sections of the most relevant biological agents are significantly higher around 280 nm. At the same time, optical transmission through several hundred meters of atmosphere becomes an issue below 300 nm. This led to the development of a laser source between the third and fourth harmonic of the Nd:YAG laser. This spectral region can be reached in several different ways. With the additional requirement of building a compact source suitable for field testing, two alternative architectures were appointed. Both architectures involved the previously used Nd:YAG laser and its harmonic modules to pump an OPO whose signal output was sum frequency mixed with either the second or third harmonic of the laser.

High beam quality of the OPO output is essential for efficient sum frequency mixing. Effort was therefore put into the design, construction and experimental testing of a simple and robust OPO which generates waves of high beam quality when pumped by high energy, nanosecond pulses. We have come up with an OPO, termed "orthogonal critical planes" OPO (OCP-OPO). The OCP-OPO generates a signal beam with symmetrical far field and has far better beam quality than ordinary OPOs which are characterized by short resonators and wide beams, with Fresnel numbers typically larger than ~ 25 [**I, II, III**]. The OCP-OPO relies on Poynting vector walk-off between the signal and idler beams, by restricting the beam divergence. This takes place in type 2 (and type 3) phase matching when collinear critical birefringent phase matching is applied. The critical plane

is spanned by the direction of propagation and walk-off direction in the nonlinear crystal. The pulse energy and damage threshold of the optics determine the maximum allowed beam width, which is typically around 5 mm for pump pulse energies on the order of 100 mJ. The OCP-OPO was realized either by using two identical nonlinear crystals in the same resonator [**III**], or by using two different crystals that have orthogonal critical planes when phase matched for the same process [**I, II**]. If two identical crystals in the same resonator are used, they must be separated by a half-wave plate which rotates by 90° the polarizations of both the pump and signal. The crystals must be oriented equivalently. This way the critical plane of the two crystals are orthogonal. As a result of two orthogonal critical planes, the signal divergence will be limited in both transversal directions, because the phase mismatch increases rapidly with angle between the pump beam and the propagation direction of perfect (collinear) phase matching in the critical plane. The effect increases with walk-off, and vanishes with no walk-off, such as in noncritical birefringent phase matching. The OCP-OPO uses the same mechanism as used in various image-rotating OPOs, such as the RISTRA. However, the OCP-OPO rotates the polarization instead of the image. The effect is enhanced by double pass pumping in a linear resonator, which reflects the image before the return pass. The OCP-OPO has proven to be reliable during field testing and long time laboratory use.

Sum frequency generation (SFG) have fewer design parameters to play with, as SFG requires two input beams. On the other side, input beam parameters, such as narrow spectrum, low divergence, smooth and uniform intensity profile and pulse power are important for efficient conversion. Moreover, spatial and temporal overlap between the beams are important for high conversion efficiency. The optimization of several of these parameters was out of scope of this work, which was limited to using a given commercially available pump laser and its modules for the generation of second and third harmonics. This was also the reason why the SFG performed considerably poorer than the simulations, which were based on smooth intensity profiles and smooth pulse shapes. Local hot-spots tend to be smeared out in a resonator with multiple passes. In sum frequency mixing, the two beams copropagate throughout the nonlinear medium, and amplify inhomogeneities in the intensity profiles, or reduce the beam quality by back conversion in (spatially and temporally) local hot-spots. The best SFG results were achieved by frequency mixing the 1.7 μm signal from a 1.06 μm pumped OCP-OPO with the third harmonic of the same pump laser [**IV**].

The 294 nm laser source comprising the OPO and SFG was incorporated in the already built biolidar based on third harmonic excitation. Either of the 294 nm or 355 nm excitation wavelengths could easily be selected without the need for realignment. The dual wavelength biolidar was tested in the field during controlled dissemination of biological aerosols. The measurements on a num-

ber of different biological agents, of which a few were biological warfare agent simulants, showed that the shorter wavelength excitation not only resulted in stronger fluorescence, but the fluorescence spectra were also more different [**V**]. This increased discrepancy is beneficial in terms of improved ability to classify the detected bioaerosols. However, the advantages in terms of fluorescence come at the cost of lower total optical conversion efficiency from the laser fundamental to 294 nm than to the third harmonic. The benefits must be traded off against increased complexity and lower optical conversion efficiency.

Outlook

Back conversion and slow signal buildup time are two of the most important intrinsic factors of high energy, nanosecond OPOs that reduce signal output in terms of beam quality and pulse energy. These are general restrictions, and not specific to the orthogonal critical planes variant of a bulk OPO. Measures that reduce the spatial inhomogeneity of, and postpone the onset of back conversion, will contribute to increased beam quality and efficient conversion. One example is to shape the pump to a spatially uniform top hat beam and temporally smooth pulses. Another measure would be to remove the idler, either between several crystals or inside. Actions that reduce signal buildup time enable conversion of the initial parts of the pump pulse and increases overall conversion. Seeding the OPO with a high quality beam is such a measure.

The SFG of UV pulses presented herein certainly has potential for improvements. First of all by shaping the input beam intensity profiles to smooth top-hat distributions and narrow bandwidth in combination with high beam quality. Also, OPOs running stably using SLM pumping sum frequency mixed with SLM laser harmonic pulses will probably result in conversion efficiencies that come closer to simulations. Alternatively, realistic beam parameters could be input in Sisyfos for better resemblance with the experiments.

A standoff biological lidar instrument based on UV-LIF would first of all profit on a simultaneous dual wavelength capacity, which would be a minor modification to the FFI built biolidar instrument. An aerosol cloud is not expected to change rapidly. In this respect, alternating 355 nm and 294 nm excitation on a shot to shot basis ($\sim$10 Hz) would qualify as simultaneous in this respect. Improving the SFG stage would increase the magnitude of the fluorescence signal proportionally. The spectral resolution may also be reduced without degrading the ability to discriminate between bioaerosols. A lower spectral resolution would be beneficial in terms of a higher signal to noise ratio of the fluorescence spectra. An enhanced standoff detector potentially lowers the false alarm rate, which is the most important parameter of an operational instrument.

Chapter 8

List of publications

8.1 Publications included in the thesis

[I] O. Farsund, G. Arisholm, and G. Rustad. "Improved beam quality from a high energy optical parametric oscillator using crystals with orthogonal critical planes". In: *Opt. Express* 18.9 (2010), pp. 9229–9235. DOI: 10.1364/OE.18.009229.

[II] G. Rustad and O. Farsund. "High pulse energy and symmetrical far field from an optical parametric oscillator in the red spectral range". In: *Journal of the European Optical Society - Rapid publications* 6.0 (2011). DOI: 10.2971/jeos.2011.11058.

[III] O. Farsund and G. Rustad. "High-pulse-energy, linear optical parametric oscillator with narrow and symmetrical far field". In: *Opt. Express* 21.17 (2013), pp. 20171–20178. DOI: 10.1364/OE.21.020171.

[IV] O. Farsund and G. Rustad. "Sum-Frequency Generation of High-Energy and High-Beam-Quality Ultraviolet Pulses". In: *International Journal of Optics* 2011 (2011). DOI: 10.1155/2011/737684.

[V] O. Farsund, G. Rustad, and G. Skogan. "Standoff detection of biological agents using laser induced fluorescence - a comparison of 294 nm and 355 nm excitation wavelengths". In: *Biomed. Opt. Express* 3.11 (2012), pp. 2964–2975. DOI: 10.1364/BOE.3.002964.

8.2 Publications not included in the thesis

8.2.1 Journal papers

[J1] O. Farsund et al. “Required Spectral Resolution for Bioaerosol Detection Algorithms Using Standoff Laser-Induced Fluorescence Measurements”. In: *IEEE Sensors Journal* 10.3 (2010), pp. 655–661. ISSN: 1530-437X. DOI: 10.1109/JSEN.2009.2037794.

[J2] G. Rustad, G. Arisholm, and O. Farsund. “Effect of idler absorption in pulsed optical parametric oscillators”. In: *Opt. Express* 19.3 (2011), pp. 2815–2830. DOI: 10.1364/OE.19.002815.

8.2.2 Conference contributions

[C1] R. Nyhavn et al. “Optimal classification of standoff bioaerosol measurements using evolutionary algorithms”. In: ed. by A. W. Fountain and P. J. Gardner. Vol. 8018. Proc. SPIE. 2011. ISBN: 978-0-81948-592-2. DOI: 10.1117/12.883919.

[C2] T. V. Haavardsholm, O. Farsund, and G. Rustad. *Biological aerosol standoff detection and agent discrimination based on experimental UV laser induced fluorescence data*. U.S. Algorithm Workshop (Baltimore, MD). 2008.

[C3] P. Jonsson et al. “Evaluation of biological aerosol stand-off detection at a field trial”. In: vol. 7484. Proc. SPIE. 2009. DOI: 10.1117/12.830401.

[C4] O. Farsund. “FFI standoff biological aerosol detection demonstrator based on UV laser induced fluorescence”. In: *2008 International Symposium on Spectral Sensing Research Technical Digest*. 2008, p. 114.

[C5] O. Farsund and G. Rustad. “OPO pulse elongation using separate pump return mirror”. In: *50 Years of Nonlinear Optics International Symposium*. Barcelona, Spain, 2012.

[C6] O. Farsund, G. Arisholm, and G. Rustad. “Sum Frequency Generation of High Energy, Low Divergence UV pulses”. In: *Advances in Optical Materials*. Optical Society of America, 2011, ATuB15. DOI: 10.1364/ASSP.2011.ATuB15.

[C7] O. Farsund, G. Arisholm, and G. Rustad. “Novel Concept for Generating High Beam Quality from High Pulse Energy Optical Parametric Oscillators”. In: *Lasers, Sources and Related Photonic Devices*. Optical Society of America, 2010, AWD2. DOI: 10.1364/ASSP.2010.AWD2.

[C8] G. Rustad, Øystein Farsund, and G. Arisholm. "Optical parametric oscillators with high pulse energy and beam quality". In: *Solid State Lasers and Amplifiers IV, and High-Power Lasers*. Vol. 7721. Proc. SPIE. 2010, 77210J–77210J–7. DOI: 10.1117/12.854958.

[C9] O. Farsund and G. Rustad. "Improved beam quality from a large-beam optical parametric oscillator with a linear resonator". In: *Advanced Solid-State Lasers Congress*. Optical Society of America, 2013, JTh2A.52. DOI: 10.1364/ASSL.2013.JTh2A.52.

[C10] G. Rustad, O. Farsund, and G. Arisholm. "Optical Parametric Oscillators with Idler Absorption". In: *Advances in Optical Materials*. Optical Society of America, 2011, AWA25. DOI: 10.1364/ASSP.2011.AWA25.

8.2.3 Tecnical reports

[R1] G. Rustad and Ø. Farsund. "Standoff detection of biological aerosols by UV-laser induced fluorescence". FFI-rapport 2008-02025. 2008.

[R2] Ø. Farsund and G. Rustad. "Standoff detection of biological aerosols by means of UV-laser induced fluorescence - results from Umeå trial 2006". FFI-rapport 2008-01990. 2008.

[R3] G. Rustad and Ø. Farsund. "Evaluation of methods and materials for optical generation of high pulse energies at 290 nm". FFI-rapport 2008-02107. 2008.

[R4] G. Rustad and Ø. Farsund. "Design of a high pulse energy coherent ultraviolet source - simulations and experimental design". FFI-rapport 2013/00372. 2013.

[R5] Ø. Farsund, G. Rustad, and G. Skogan. "Comparison of 294 nm and 355 nm excitation wavelengths in UVLIF standoff detection of biological aerosols released in a semi-closed chamber". FFI-rapport 2012-00211. 2012.

Chapter 9

Contribution in publications

In this chapter, I summarize my contribution in the papers which are included in the thesis. This corresponds with the co-authorship declarations accompanying the filing of the thesis. Responsible for writing means the actual writing of the main part of the paper, as well as incorporating comments and discussions regarding the paper into the text. Moreover, the resonsible person has managed the contact with the journal editor and referees.

Paper I

Improved beam quality from a high energy optical parametric oscillator using crystals with orthogonal critical planes. O. Farsund, G. Arisholm, G. Rustad, Opt. Express, Vol. 18, pp. 9229-35 (2010).

My contribution:

- Idea of using two different crystals with orthogonal critical planes for the same nonlinear process, to improve the beam quality
- Simulated the OPO (Sisyfos) to optimize parameters and test the idea.
- Design of experiments and optimization of critical optical components, such as mirrors and nonlinear crystals through simulations
- Procurement of optical components
- Realization and implementation of experiments
- Data analysis

- Responsible for writing the article

The co-authors helped to find available crystals, including calculation of crystal properties. They also helped to make the simulation model. Co-authors supervised the writing, including discussing theory and results. In particular, G. Rustad helped to specify the optical components and to build the experimental setup, as it was the first OPO setup operated by the candidate. He also helped solving problems during the experiment phase.

Paper II

High pulse energy and symmetrical far field from an optical parametric oscillator in the red spectral range. G. Rustad, Ø. Farsund, JEOS:RP Vol. 6, paper 11058 (2011).

My contribution:

- Design of experiments and optimization of critical optical components, such as mirrors and nonlinear crystals through simulations
- Procurement of optical components
- Realization and implementation of experiments
- Data analysis

Co-author G. Rustad carried out the simulations including the building of the simulation model, in addition to being responsible for the writing of the article.

Paper III

High-pulse-energy, linear optical parametric oscillator with narrow and symmetrical far field. O. Farsund, G. Rustad, Opt. Express, Vol. 21, pp. 20171-78 (2013).

My contribution:

- Design of experiments
- Realization and implementation of experiments
- Data analysis
- Responsible for writing

Co-author G. Rustad carried out the simulations. Discussed and contributed to the writing of the paper.

Paper IV

Sum frequency generation of high energy and high beam quality ultraviolet pulses. O. Farsund, G. Rustad, International Journal of Optics special issue on Optical Parametric Processing, paper 737684 (2011).

My contribution:

- Design of experiments and optimization of critical optical components, such as mirrors and nonlinear crystals through simulations
- Procurement of optical components
- Realization and implementation of experiments
- Data analysis
- Responsible for writing

Co-author Gunnar Rustad supervized the use of Sisyfos simulations and contributed to problem solving during experimental phase. He also contributed to the text and the paper contents through discussions.

Paper V

Standoff detection of biological agents using laser induced fluorescence - a comparison of 294 nm and 355 nm excitation wavelengths. O. Farsund, G. Rustad, G. Skogan, Biomed. Opt. Express, Vol. 3, pp. 2964-75 (2012).

My contribution:

- Responsible for design and realization optical setup with two laser wavelengths before field test
- Design and realization of field experimental setup
- Carry out field experiment
- Responsible for data analysis
- Responsible for writing

Co-author Gunnar Rustad's contribution:

- Design and realization of field experimental setup

- Carry out field experiment
- Discussion and contribution to the analysis and writing of the paper

Co-author Gunnar Skogan's contribution:

- Prepared and disseminated biological samples
- Setup of aerosol reference measurement (aerodynamic particle sizer, APS), APS data acquisition and results

Bibliography

[1] O. Svelto and D.C. Hanna. *Principles of Lasers (3rd ed.)* New York: Plenum Press, 1989.

[2] S. D. Mayor et al. "Lidars: A key component of urban biodefence". In: *Biosecur. Bioterror.* 6 (2008), pp. 45–56.

[3] J. Ho. "Future of biological aerosol detection". In: *Analytica Chimica Acta* 457.1 (2002), pp. 125–148. ISSN: 0003-2670. DOI: 10.1016/S0003-2670(01)01592-6.

[4] "Laser Based Stand-Off Detection of Biological Agents, final report of task group SET-098/RTG-55". NATO Research and Technology Group technical report RTO-TR-SET-098 AC/323(SET-098)TP/265. 2010.

[5] T. Vo-Dinh, ed. *Biomedical Photonics Handbook*. New York, New York: CRC Press, 2003.

[6] M. Sletmoen and G. Rustad. "Vekselvirkning mellom lys og biologisk materiale". FFI-notat 2008-00828. 2008.

[7] N. Bloembergen. *Nonlinear optics*. Singapore: World Scientific, 1996. ISBN: 981-02-2599-7.

[8] A. Yariv. *Quantum electronics*. New York, New York: John Wiley and Sons Inc., 1967.

[9] Y.R. Shen, ed. *Principles of Nonlinear Optics*. New York, New York: Wiley, 1984.

[10] P. B. Butcher and D. Cotter. *The Elements of Nonlinear Optics*. Cambridge University Press, 1990.

[11] R. W. Boyd. *Nonlinear optics*. San Diego, Calif.: Academic Press, 1992.

[12] N. Bloembergen. "Nonlinear optics: Past, present, and future". In: *IEEE Journal of Selected Topics in Quantum Electronics* 6.6 (2000), pp. 876–880. ISSN: 1077-260X. DOI: 10.1109/2944.902137.

[13] E. Garmire. "Nonlinear optics in daily life". In: *Opt. Express* 21.25 (2013), pp. 30532–30544. DOI: 10.1364/OE.21.030532.

[14] B. Boulanger et al. "Focus issue introduction: nonlinear optics". In: *Opt. Mater. Express* 1.7 (2011), pp. 1393–1398. DOI: 10.1364/OME.1.001393.

[15] *50 Years of Nonlinear Optics International Symposium*. 50 Years of Nonlinear Optics International Symposium. Barcelona, Spain, 2012. URL: http://www.nlo50.icfo.es/index.html.

[16] B. Saleh and M. C. Teich. *Fundamentals of photonics*. New York: Wiley, 1991. ISBN: 0-471-83965-5.

[17] J. Kerr. In: *Phil. Mag. J. Sci.,* ser fourth 50 (1875).

[18] R. W. Boyd. *History of research in nonlinear optics at the institute of optics*. url date: 2014-03-13. URL: http://www.optics.rochester.edu/~stroud/BookHTML/ChapVII_pdf/VII_56.pdf.

[19] T. Maiman. "Stimulated optical radiation in ruby". In: *Nature* 187.4736 (1960), pp. 493–494. ISSN: 0028-0836. DOI: 10.1038/187493a0.

[20] *Laser*. url date: 2014-03-13. 2014. URL: https://en.wikipedia.org/wiki/Laser.

[21] P.A. Franken et al. "Generation of optical harmonics". In: *Physical Review Letters* 7.4 (1961), pp. 118–&. ISSN: 0031-9007. DOI: 10.1103/PhysRevLett.7.118.

[22] J. A. Armstrong et al. "Light waves in a nonlinear dielectric". In: *Phys. Rev.* 127 (1962), pp. 1918–1939.

[23] J.A. Giordmaine. "Mixing of light beams in crystals". In: *Phys. Rev. Lett.* 8 (1962), pp. 19–20.

[24] M. Bass et al. "Optical mixing". In: *Phys. Rev. Lett.* 8 (1962), p. 18.

[25] S. A. Akhmanov et al. "Observation of parametric amplification in the optical range". In: *Journal of Experimental and Theoretical Physics Letters* 2 (1965), pp. 191–193.

[26] J.A. Giordmaine and R.C. Miller. "Tunable coherent parametric oscillation in $LiNbO_3$ at optical frequencies". In: *Phys. Rev. Lett.* 14 (1965), pp. 973–976.

[27] S. A. Akhmanov et al. "Generation of coherent radiation in the infrared band by nonlinear-optics methods". In: *Journal of Experimental and Theoretical Physics Letters* 4 (1966), pp. 14–17.

[28] S. A. Akhmanov et al. "Nonstationary nonlinear optical effects and ultrashort light pulse formation". In: *IEEE J. Quantum Electron.* 4 (1968), pp. 598–605. DOI: 10.1109/JQE.1968.1074933.

[29] S. A. Akhmanov, R. V. Khokhlov, and A. P. Sukhorukov. "Self-Focusing, Self-Defocusing and Self-Modulation of Laser Beams". In: *Laser Handbook*. Ed. by F.T. Arecchi and E.O. Schulz-Dubois. Vol. 2. North-Holland, 1972, pp. 1151–1228.

[30] R. L. Byer. *Fifty years of nonlinear optics, tunable sources from OPOs to coherent X-rays*. DOI: 10.1364/NLO.2011.NWB2.

[31] Amnon Yariv. *Celebrating the 50th anniversary of nonlinear optics*. url date: 2014-04-01. 2014. URL: https://www.osapublishing.org/view_article.cfm?gotourl=https%3A%2F%2Fwww%2Eosapublishing%2Eorg%2FDirectPDFAccess%2FC4CADA6D%2DB7BE%2DEF74%2DD9E756DC1225F5D3%5F224090%2Fome%2D1%2D7%2D1393%2EPDF%3Fda%3D1%26id%3D224090%26seq%3D3%26mobile%3Dno&org=.

[32] R. Trebino et al. "Measuring ultrashort laser pulses in the time-frequency domain using frequency-resolved optical gating". In: *Rev. Sci. Instrum.* 68.9 (1997), 3277–3295. DOI: 10.1063/1.1148286.

[33] A. Yariv and P. Yeh. *Optical waves in crystals - propagation and control of laser radiation*. Hoboken, New Jersey: Wiley-interscience, 2003. ISBN: 0-471-43081-1.

[34] John David Jackson. *Classical Electrodynamics*. Second. New York: Wiley, 1975.

[35] L. D. Landau and E. M. Lifshitz. *Electrodynamics of continuous media*. Second. Oxford: Pergamon Press, 1960.

[36] Charles Kittel. *Introduction to Solid State Physics*. 6th ed. New York: Wiley, 1986.

[37] P.E. Powers. *Fundamentals of nonlinear optics*. New York, USA: CRC Press, 2011. ISBN: 978-1-4200-9351-3.

[38] G. Arisholm and H. Fonnum. "Simulation System For Optical Science (SISYFOS) - theoretical background". To be published as FFI report. 2015.

[39] M. Born and E. Wolf. *Principles of Optics, 4th ed.* Pergamon Press, 1970.

[40] R. Paschotta. *RP Photonics Encyclopedia*. url date: 2014-03-11. 2014. URL: http://www.as-photonics.com/encyclopedia.html.

[41] A. V. Smith, D. J. Armstrong, and W. J. Alford. "Increased acceptance bandwidths in optical frequency conversion by use of multiple walk-off-compensating nonlinear crystals". In: *J. Opt. Soc. Am. B* 15.1 (1998), pp. 122–141. DOI: 10.1364/JOSAB.15.000122.

[42] F. Blanchard et al. "Generation of Intense Terahertz Radiation via Optical Methods". In: *Selected Topics in Quantum Electronics, IEEE Journal of* 17.1 (2011), pp. 5–16. ISSN: 1077-260X. DOI: 10.1109/JSTQE.2010.2047715.

[43] G. Arisholm. "Numerical modelling of optical parametric frequency conversion and self-focusing". PhD thesis. University of Oslo, 1999.

[44] D.A. Roberts. "Simplified characterization of uniaxial and biaxial nonlinear optical crystals: A plea for standardization of nomenclature and conventions". In: *IEEE J. Quantum Electron.* 28 (1992), pp. 2057–2074.

[45] V. G. Dmitriev, G. G. Gurzadyan, and D. N. Nikogosyan. *Handbook of nonlinear optical crystals*. Second edition. Heidelberg: Springer-Verlag, 1997.

[46] G. Arisholm and G. Rustad. "Review of theory and materials for optical parametric oscillators in the infrared". FFI/RAPPORT-97/02589. 1997.

[47] Norman P. Barnes and Vincent J. Corcoran. "Parametric generation processes: spectral bandwidth and acceptance angles". In: *Appl. Opt.* 15.3 (1976), pp. 696–699. DOI: 10.1364/AO.15.000696.

[48] D. J. Armstrong et al. "Parametric amplification and oscillation with walkoff-compensating crystals". In: *J. Opt. Soc. Am. B* 14 (1997), pp. 460–474.

[49] G. Arisholm. "Quantum noise initiation and macroscopic fluctuations in optical parametric oscillators". In: *J. Opt. Soc. Am. B* 16 (1999), pp. 117–127.

[50] W.R. Bosenberg et al. "Continuous-wave singly resonant optical parametric oscillator based on periodically poled $LiNbO_3$". In: *Opt. Lett.* 21.10 (1996), pp. 713–715. DOI: 10.1364/OL.21.000713.

[51] M. Ebrahim-Zadeh et al. "Breakthroughs in Photonics 2012: Breakthroughs in Optical Parametric Oscillators". In: *Photonics Journal, IEEE* 5.2 (2013), pp. 0700105–0700105. ISSN: 1943-0655. DOI: 10.1109/JPHOT.2013.2255268.

[52] A. Aadhi et al. "All-periodically poled, high-power, continuous-wave, single-frequency tunable UV source". In: *Opt. Lett.* 40.1 (2015), pp. 33–36. DOI: 10.1364/OL.40.000033.

[53] D. T. Reid, M. Ebrahim-Zadeh, and W. Sibbett. "Design criteria and comparison of femtosecond optical parametric oscillators based on $KTiOPO_4$ and $RbTiOAsO_4$". In: *J. Opt. Soc. Am. B* 12.11 (1995), pp. 2168–2179. DOI: 10.1364/JOSAB.12.002168.

[54] Magnus W. Haakestad et al. “Intracavity trace molecular detection with a broadband mid-IR frequency comb source”. In: *J. Opt. Soc. Am. B* 30.3 (2013), pp. 631–640. ISSN: 0740-3224.

[55] Magnus W. Haakestad et al. “Five-cycle pulses near $\lambda = 3\,\mu m$ produced in a subharmonic optical parametric oscillator via fine dispersion management”. In: *Laser & Photonics Reviews* 7.6 (2013), pp. L93–L97. ISSN: 1863-8880. DOI: 10.1002/lpor.201300112.

[56] “Lasers and laser-related equipment – Test methods for laser beam parameters – beam widths, divergence angle and beam propagation factor”. ISO 11146:1999(E). Geneva, CH, 1999.

[57] A. E. Siegman. “How to (Maybe) Measure Laser Beam Quality”. In: *DPSS (Diode Pumped Solid State) Lasers: Applications and Issues*. Optical Society of America, 1998, MQ1. DOI: 10.1364/DLAI.1998.MQ1.

[58] G.T. Moore and K. Koch. “Phasing of tandem crystals for nonlinear optical frequency conversion”. In: *Optics Communications* 124.3-4 (1996), pp. 292–294. ISSN: 0030-4018. DOI: 10.1016/0030-4018(95)00652-4.

[59] G. Arisholm. “General numerical methods for simulating second order nonlinear interactions in birefringent media”. In: *J. Opt. Soc. Am. B* 14 (1997), pp. 2543–2549.

[60] G. Arisholm and K. Stenersen. “Optical parametric oscillator with non-ideal mirrors and single- and multi-mode pump beams”. In: *Opt. Express* 4 (1999), pp. 183–192.

[61] G. Arisholm et al. “Efficient conversion from 1 µm to 2 µm by a KTP-based ring optical parametric oscillator”. In: *Opt. Lett.* 27 (2002), pp. 1336–1338.

[62] G. Arisholm and H. Fonnum. “Simulation System For Optical Science (SISYFOS) - tutorial”. FFI-report 2012-02042. 2012.

[63] G. Arisholm, Ø. Nordseth, and G. Rustad. “Optical parametric master oscillator and power amplifier for efficient conversion of high-energy pulses with high beam quality”. In: *Opt. Express* 12 (2004), pp. 4189–4197.

[64] D.N. Nikogosyan. *Nonlinear optical crystals: a complete survey*. New York, NY, USA: Springer, 2005.

[65] W. J. Alford and A. V. Smith. “Wavelength variation of the second-order nonlinear coefficients of $KNbO_3$, $KTiOPO_4$, $KTiOAsO_4$, $LiNbO_3$, $LiIO_3$, $\beta - BaB_2O_4$, KH_2PO_4, and LiB_3O_5 crystals: a test of Miller wavelength scaling”. In: *J. Opt. Soc. Am. B* 18.4 (2001), pp. 524–533. DOI: 10.1364/JOSAB.18.000524.

[66] K. Kato and E. Takaoka. "Sellmeier and thermo-optic dispersion formulas for KTP". In: *Applied Optics* 41.24 (2002), pp. 5040–5044. ISSN: 1559-128X. DOI: 10.1364/AO.41.005040.

[67] V. G. Dmitriev and D. N. Nikogosyan. "Effective nonlinearity coefficients for 3-wave interactions in biaxial crystals of mm2 point group symmetry". In: *Optics Communications* 95.1-3 (1993), pp. 173–182. ISSN: 0030-4018. DOI: 10.1016/0030-4018(93)90066-E.

[68] A. V. Smith and M. S. Bowers. "Image-rotating cavity designs for improved beam quality in nanosecond optical parametric oscillators". In: *J. Opt. Soc. Am. B* 18 (2001), pp. 706–713.

[69] AS-Photonics LLC. *RISTRA Overview*. url date: 2014-02-18. 2014. URL: http://www.as-photonics.com/ristra-opo/overview.

[70] A. V. Smith and D. J. Armstrong. "Nanosecond optical parametric oscillator with 90 degrees image rotation: design and performance". In: *J. Opt. Soc. Am. B* 19.8 (2002), pp. 1801–1814. ISSN: 0740-3224. DOI: 10.1364/JOSAB.19.001801.

[71] C.D. Nabors and G. Frangineas. "Optical parametric oscillator with binoncolinear, porro prism cavity". In: *Advanced Solid State Lasers, Trends in Optics and Photonics*. Ed. by R. Pollock and W.R. Bosenberg. Vol. 10. Optical Society of America. 1997, pp. 90–93.

[72] D. J. Armstrong and A. V. Smith. "Tendency of nanosecond optical parametric oscillators to produce purely phase-modulated light". In: *Opt. Lett.* 21 (1996), pp. 1634–1636.

[73] *Quantel Q-smart 100 data sheet*. url date: 2015-12-14. URL: http://www.quantel-laser.com/tl_files/client/MY\%20QUANTEL\%20SPACE/Sales\%20Literature/Q-smart100_Specs_EN_012014.pdf.

[74] G. Anstett and R. Wallenstein. "Experimental investigation of the spectro-temporal dynamics of the light pulses of Q-switched Nd:YAG lasers and nanosecond optical parametric oscillators". In: *Applied Physics B-Lasers and Optics* 79.7 (2004), pp. 827–836. ISSN: 0946-2171. DOI: 10.1007/s00340-004-1620-5.

[75] Joseph R. Lakowicz. *Principles of Fluorescence Spectroscopy*. Second. New York: Kluwer Academic/Plenum Publishers, 1999.

[76] V. Sivaprakasam et al. "Multiple UV wavelength excitation and fluorescence of bioaerosols". In: *Opt. Express* 12.19 (2004), pp. 4457–4466. DOI: 10.1364/OPEX.12.004457.

[77] V. Sivaprakasam et al. “Spectral characterization of biological aerosol particles using two-wavelength excited laser-induced fluorescence and elastic scattering measurements”. In: *Opt. Express* 19.7 (2011), pp. 6191–6208. DOI: 10.1364/OE.19.006191.

[78] R. M. Measures. *Laser remote sensing: Fundamentals and applications*. Malabar, Florida: Krieger Publishing Company, 1992.

[79] A Fix and G Ehret. “Intracavity frequency mixing in pulsed optical parametric oscillators for the efficient generation of continuously tunable ultraviolet radiation”. In: *Applied Physics B-Lasers and Optics* 67.3 (1998), pp. 331–338. ISSN: 0946-2171. DOI: 10.1007/s003400050512.

[80] D. J. Armstrong and A. V. Smith. “All solid-state high-efficiency tunable UV source for airborne or satellite-based ozone DIAL systems”. In: *IEEE Journal of Selected Topics in Quantum Electronics* 13.3 (2007), pp. 721–731. ISSN: 1077-260X. DOI: 10.1109/JSTQE.2007.896600.

[81] Y. L. Pan et al. “Fluorescence spectra of atmospheric aerosol particles measured using one or two excitation wavelengths: Comparison of classification schemes employing different emission and scattering results”. In: *Opt. Express* 18.12 (2010), pp. 12436–12457. DOI: 10.1364/OE.18.012436.

[82] Y. L. Pan, H. Huang, and R. K. Chang. “Clustered and integrated fluorescence spectra from single atmospheric aerosol particles excited by a 263 - and 351 nm laser at New Haven, CT, and Adelphi, MD”. In: *Journal of Quantitative Spectroscopy and Radiative Transfer* 113.17 (2012), pp. 2213–2221. ISSN: 0022-4073. DOI: 10.1016/j.jqsrt.2012.07.028.

[83] P. H. Kaye et al. “Bio-aerosol fluorescence”. In: *Optics of Biological Particles*. Ed. by A. Hoekstra, V. Maltsev, and G. Videen. Vol. 238. NATO science series, Series II, Mathematics, Physics and Chemistry. 2007, pp. 63–164.

[84] H. C. Huang et al. “Real-time measurement of dual-wavelength laser-induced fluorescence spectra of individual aerosol particles”. In: *Opt. Express* 16.21 (2008), pp. 16523–16528. DOI: 10.1364/OE.16.016523.

[85] V. C. Coffey. “Advances in Standoff Detection Make the World Safer”. In: *Photonics Spectra* (2013), pp. 44–47. URL: http://www.photonicsspectra-digital.com/photonicsspectra/201304/?pg=44#pg44.

Acronyms

APS aerodynamic particle sampler.

AR anti-reflective.

BBO $\beta - BaB_2O_4$, beta-barium borate.

BQ beam quality.

CCD charge-coupled device.

CW continuous wave.

DFG difference frequency generation.

DRO doubly resonant OPO.

FFI Norwegian Defence Research Establishment.

FOI Totalförsvarets forskningsintitut.

FROG frequency-resolved optical gating.

FWHM full width at half maximum.

FWM four wave mixing.

ICCD intensified charge-coupled device.

IR infrared.

KDP KH_2PO_4, potassium dihydrogen phosphate.

KTA $KTiOAsO_4$, potassium titanyl arsenate.

KTP $KTiOPO_4$, potassium titanyl phosphate.

Laser light amplification by stimulated emission of radiation.

LIBS laser induced breakdown spectroscopy.

lidar light detection and ranging.

LIF laser induced fluorescence.

MLM multi-longitudinal mode.

MOPA master oscillator power amplifier.

NADH the reduced form of nicotinamide adenine dinucleotide.

NATO North Atlantic Treaty Organization.

NCPM noncritical phase matching.

Nd:YAG Nd:$Y_3Al_5O_{12}$, neodymium-doped yttrium aluminium garnet laser crystal.

OCP-OPO orthogonal critical planes optical parametric oscillator.

OPA optical parametric amplifier.

OPG optical parametric generation.

OPO optical parametric oscillator.

PCR polymerase chain reaction.

PMT photo multiplier tube.

PPKTP periodically poled KTP.

QPM quasi phase matching.

RISTRA rotated-image, singly resonant, twisted-rectangle.

SBS stimulated Brillouin scattering.

SFG sum frequency generation.

SHG second harmonic generation.

Sisyfos simulation system for optical science.

SLM single-longitudinal mode.

SRO singly resonant OPO.

SRS stimulated Raman scattering.

UV ultraviolet.

VRM variable reflectivity mirror.

Paper I

Improved beam quality from a high energy optical parametric oscillator using crystals with orthogonal critical planes

Published in Optics Express.

DOI: 10.1364/OE.18.009229

Improved beam quality from a high energy optical parametric oscillator using crystals with orthogonal critical planes

Øystein Farsund,* Gunnar Arisholm, and Gunnar Rustad

Norwegian Defence Research Establishment (FFI), PO Box 25, NO-2027 Kjeller, Norway
**Oystein.Farsund@ffi.no*

Abstract: We demonstrate with simulations and experiments that an optical parametric oscillator using two different crystals with orthogonal walk-off planes can generate a symmetric, high-quality beam even if the resonator has a high Fresnel number. In the experiments we used KTA and BBO crystals to convert 5 ns pulses at 1.06 μm to 1.7 μm pulses with more than 10 mJ energy and beam quality $M^2 \approx 2$.

OCIS codes: (190.2620) Harmonic generation and mixing; (190.4410) Nonlinear optics, parametric processes; (190.4970) Parametric oscillators and amplifiers.

References and links

1. A. V. Smith, D. J. Armstrong, and W. J. Alford, "Increased acceptance bandwidths in optical frequency conversion by use of multiple walk-off-compensating nonlinear crystals," J. Opt. Soc. Am. B **15**, 122–141 (1998).
2. A. V. Smith, and M. S. Bowers, "Image-rotating cavity designs for improved beam quality in nanosecond optical parametric oscillators," J. Opt. Soc. Am. B **18**, 706–713 (2001).
3. C. D. Nabors, and G. Frangineas, "Optical parametric oscillator with bi-noncolinear, porro prism cavity," in *Advanced Solid State Lasers*, Trends in Optics and Photonics, (Optical Society of America, Washington, DC, Orlando, FL, 1997), Vol. 10, pp. 90–93.
4. G. Anstett, G. Goritz, D. Kabs, R. Urschel, R. Wallenstein, and A. Borsutzky, "Reduction of the spectral width and beam divergence of a BBO-OPO by using collinear type-II phase matching and back reflection of the pump beam," Appl. Phys. B **72**, 583–589 (2001).
5. D. J. Armstrong, and A. V. Smith, "All solid-state high-efficiency tunable UV source for airborne or satellite-based ozone DIAL systems," IEEE J. Sel. Top. Quantum Electron. **13**, 721–731 (2007).
6. Y. Ehrlich, S. Pearl, and S. Fastig, "High brightness tunable tandem optical parametric oscillator at 8-12 μm," in *Advance Solid State Lasers* (2004), Vol. **94**, 398–402.
7. G. Arisholm, "General numerical methods for simulating second-order nonlinear interactions in birefringent media," J. Opt. Soc. Am. B **14**, 2543–2549 (1997).
8. G. Arisholm, "Advanced numerical simulation models for second-order nonlinear interactions," Proc. SPIE **3685**, 86–97 (1999).
9. W. J. Alford, R. J. Gehr, R. L. Schmitt, A. V. Smith, and G. Arisholm, "Beam tilt and angular dispersion in broad-bandwidth, nanosecond optical parametric oscillators," J. Opt. Soc. Am. B **16**, 1525–1532 (1999).
10. D. D. Lowenthal, "CW periodically poled $LiNbO_3$ optical parametric oscillator model with strong idler absorption," IEEE J. Quantum Electron. **34**, 1356–1366 (1998).
11. G. Rustad, Ø. Farsund, and G. Arisholm, Manuscript in preparation (2010).
12. D. N. Nikogosyan, *Nonlinear optical crystals: a complete survey* (Springer, New York, 2005).
13. G. Arisholm, and K. Stenersen, "Optical parametric oscillator with non-ideal mirrors and single- and multi-mode pump beams," Opt. Express **4**, 183–192 (1999).
14. D. J. Armstrong, W. J. Alford, T. D. Raymond, A. V. Smith, and M. S. Bowers, "Parametric amplification and oscillation with walkoff-compensating crystals," J. Opt. Soc. Am. B **14**, 460–474 (1997).

1. Introduction

Designing an optical parametric oscillator (OPO) with both high energy and beam quality leads to conflicting demands. First, high energy operation implies that the beams must be wide in order to avoid optical damage. Second, the nanosecond pump pulses available from high energy, Q-switched lasers require a short resonator to allow rapid signal buildup for efficient conversion. However, a short resonator with wide beams has high Fresnel number

#126039 - $15.00 USD Received 26 Mar 2010; accepted 13 Apr 2010; published 19 Apr 2010

and poor suppression of higher-order transverse modes. This leads to poor beam quality unless a method can be found to restrict the divergence of the generated beams.

Walk-off is normally considered a detrimental process in nonlinear crystals because it reduces the overlap between the beams. However, walk-off between the signal and idler beams increases the spatial coherence, and hence the beam quality, in the walk-off plane. The angular acceptance interval for two interacting beams of orthogonal polarization is inversely proportional to the walk-off distance [1]. In collinear, critically type 2 phase matched OPO's, the beam quality therefore tends to be asymmetric since the angular acceptance interval of the nonlinear interaction is very different in the critical and noncritical direction [2].

Several approaches to reduce the asymmetry exist, for example using a prism reflector to flip higher-order beam components out of the noncritical plane [3,4], intracavity image rotation [2,5], or employing a confocal unstable resonator [2,6].

2. OPO with orthogonal critical planes

Our approach to attain a symmetric, high-quality beam in an OPO with large Fresnel number is to employ two different nonlinear crystals with orthogonal critical planes. Both crystals are critically, type 2 phase matched, so that either the signal or the idler beam has walk-off. The polarization of the pump does not matter in principle, but to avoid the need for waveplates it is important that each beam can have the same polarization direction in both crystals. Because the pump must always have the fast polarization (for phase matching in crystals with normal dispersion), one crystal must have walk-off for the slow polarization (e.g. positive uniaxial crystal) and the other must have walk-off for the fast polarization (e.g. negative uniaxial crystal). Biaxial crystals can of course also be used; the important point is only to have walk-off for the slow polarization in one crystal and for the fast polarization in the other. The proposed OPO configuration is shown in Fig. 1.

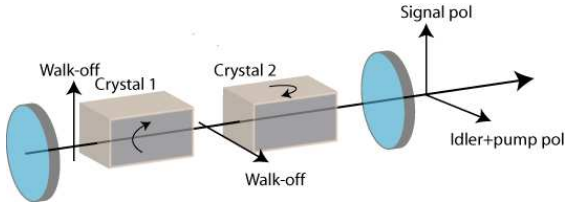

Fig. 1. Sketch of directions of polarization in the OPO with orthogonal critical planes for collinear type 2 phase matching. The walk-off direction in crystal 1 is perpendicular to the walk-off direction in crystal 2. This leads to increased beam quality for the beams generated in a resonator containing both crystal types compared to a resonator with only one type of crystal.

This design has the advantages that it requires mirrors and crystals only, and it allows for simple angle tuning of the crystals. Although walk-off is essential for limiting the angular acceptance interval, a walk-off distance comparable to the beam width can also reduce the gain severely. The optimal walk-off distance is a compromise between beam quality and efficiency, and it depends on beam width and gain. In some cases, a single, long crystal of each type may be optimal, in other cases walk-off compensating pairs. The two types of crystals will in general have different walk-off angles and nonlinear coupling coefficients. Both these parameters must be taken into account to find a length ratio that leads to a symmetric beam.

A similar configuration was proposed in [2], however, the OPO was based on two equal crystals separated by a retarder plate which rotates the polarizations (but not the field intensity pattern) of all beams by $\pi/2$.

3. Simulations

In order to study the effects of orthogonal critical planes, an OPO was first simulated with parameters which were not restricted to those of existing crystals. We assumed two materials

#126039 - $15.00 USD Received 26 Mar 2010; accepted 13 Apr 2010; published 19 Apr 2010

which differed only in the direction of walk-off and had otherwise identical parameters. A simulation model accounting for all relevant effects [7,8] was used, and the pump beam was modeled as a 6th order super-Gaussian single-longitudinal-mode (SLM) beam, corresponding to $M^2 \approx 1.3$.

We simulated a single-pass pumped, singly resonant, linear OPO containing four crystals. The first and second crystal pairs correspond to crystal 1 and 2 in Fig. 1, and each of the crystal pairs is configured for walk-off compensation, which suppresses beam tilt and angular dispersion [9]. The parameters for the simulated OPO are listed in Table 1.

Table 1. OPO parameters used in the simulations.

Parameter		Value		Unit
Index of refraction	Pump (1.06 μm)	1.79		
	Signal (1.7 μm)	1.81		
	Idler (2.8 μm)	1.76		
d_{eff}		4		pm/V
Walk-off angle		2.3		°
Crystal length		5		mm
Air gaps		2		mm
Fresnel number		62		
Mirror reflectance		input	output	
	Pump (1.06 μm)	0	0	
	Signal (1.7 μm)	1	0.5	
	Idler (2.8 μm)	0	0	
Pump beam diameter	(FWHM)	3		mm
Pump pulse duration	(FWHM)	5		ns
Peak fluence		< 2		J/cm^2

Two configurations were simulated and compared: crystal pairs with either parallel or orthogonal walk-off planes. The energy and beam quality as functions of pump energy are shown in Fig. 2.

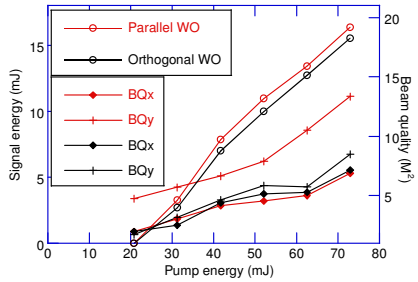

Fig. 2. Energy (open circles) and beam quality in both directions (diamonds and crosses) for the OPO containing crystal pairs with parallel (red) and orthogonal critical planes (black).

The threshold and signal output energy are approximately the same for both configurations. The OPO with orthogonal critical planes generates an almost symmetric beam, in contrast to the OPO with parallel critical planes.

The walk-off distance through one of the crystals used in the simulations was only 0.2 mm, corresponding to 7% of the beam diameter. A greater walk-off distance leads to improved beam quality by reducing the acceptance angle. This effect was studied by varying

#126039 - $15.00 USD Received 26 Mar 2010; accepted 13 Apr 2010; published 19 Apr 2010

the walk-off angle in the simulations, while the other parameters were chosen to keep the nonlinear coupling constant. Figure 3 shows the calculated pulse energy and beam quality as functions of walk-off distance relative to the beam diameter for an OPO with orthogonal walk-off planes.

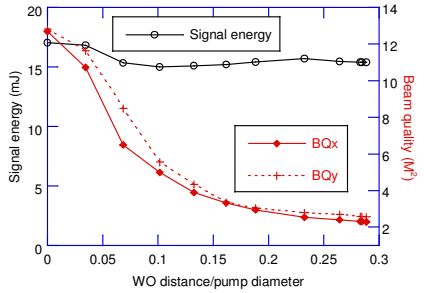

Fig. 3. Simulated performance of the OPO with orthogonal critical planes as function of the walk-off distance relative to the beam diameter. The pump energy was 70 mJ.

We notice that the walk-off distance relative to the beam size has significant effect on the beam quality. Therefore, in an actual experiment, it is important to choose crystal type and length to get a suitable walk-off distance compared to the beam size.

The crystals in our experimental realization of the OPO have some idler absorption, which can reduce back conversion [10] and therefore affect the beam quality. In order to study the effects of orthogonal critical planes and idler absorption independently, we also simulated both OPO configurations with idler absorption 150 m^{-1}. The results in Fig. 4 show that both idler absorption and orthogonal critical planes contribute to improved beam quality, and they work well in combination. The effect of idler absorption is investigated in detail in a separate paper [11].

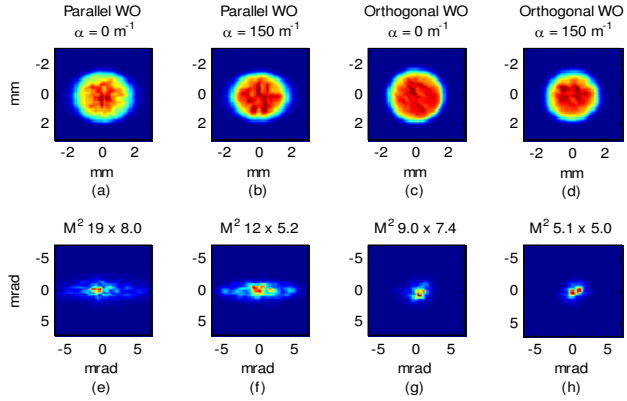

Fig. 4. The effect of idler absorption at 70 mJ pump energy (3.5 times threshold) for the two OPO configurations. Near and far fields for parallel critical planes without idler absorption are shown in (a) and (e) respectively, whereas the same case including idler absorption at 150 m^{-1} are shown in (b) and (f). Near and far fields for orthogonal critical planes without idler absorption are shown in (c) and (g), whereas the orthogonal critical planes configuration including idler absorption at 150 m^{-1} are shown in (d) and (h).

#126039 - $15.00 USD Received 26 Mar 2010; accepted 13 Apr 2010; published 19 Apr 2010

4. Choice of crystals

Table 2 compares the most common nonlinear materials that can be used in an OPO for conversion from 1.064 µm to about 1.7 µm with type 2 critical phase matching.

Table 2. Materials for type 2 phase matched OPO for 1.06 µm to 1.7 µm conversion. S/F wo lists whether slow or fast beam has walk-off, U/B lists whether the material is uniaxial or biaxial, $L{\cdot}\Delta\theta_2$ is the product of crystal length and acceptance angle for the signal, and WO is the walk-off angle. The crystal data and acronyms for the crystal names are given in [12].

Material	S/F wo	U/B	θ/φ	d_{eff}	$L{\cdot}\Delta\theta_2$	WO
			°	pm/V	mm·mrad	°
KTP	Slow (XZ)	B	46/0	2.6	17.4	2.8
KTA	Slow (XZ)	B	43/0	2.9	20.7	2.3
BBO	Fast	U	30	1.6	13.2	3.5
BiBO	Slow (XZ)	B	42/0	2.6	10.0	4.8
YCOB	Fast (XY)	B	90/42	1.3	70	0.9
LNO	Fast	U	58	0.6	17.6	2.2
LBO	Slow (YZ)	B	44/90	0.5	101	0.5

To have orthogonal walk-off directions, we need one crystal where the slow beam has walk-off and another crystal with walk-off for the fast beam. We note that while there are several good materials with walk-off for the slow beam, there are fewer and less obvious candidates with walk-off for the fast beam. BBO has high idler absorption, YCOB has low walk-off, and LNO has a small effective nonlinearity for type 2 phase matching. As discussed in the previous section, some idler absorption may in fact be advantageous for the OPO performance, so we chose to use BBO. The idler absorption varies rapidly with wavelength, so by tuning the OPO we can effectively adjust the absorption to a suitable value. We used a signal wavelength of 1.68 µm, corresponding to an idler wavelength around 2.9 µm and an approximate absorption of 250 m^{-1}. We used KTA for the crystal with walk-off for the slow beam. It was chosen because of its higher nonlinearity, but it is likely that both KTP and BiBO would perform similarly.

5. Experiments

A sketch of the experimental setup including mirror specifications is given in Fig. 5. The resonator is not perfectly singly resonant because of the considerable idler reflection at the input mirror. The effect of the idler reflection is reduced by the idler absorption and the use of multi-longitudinal-mode (MLM) pump pulses [13]. The Fresnel number of the experimental setup was approximately 50.

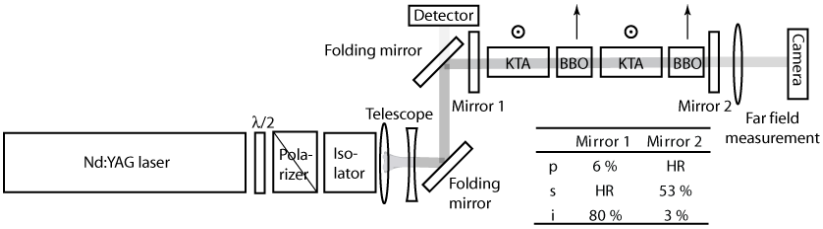

Fig. 5. The experimental setup. The half wave plate and polarizer were used to attenuate the pump energy. The telescope reduced the pump beam diameter to 4 mm. KTA and BBO crystals were 15 mm and 10 mm long, respectively. Wavelength tuning was accomplished by rotating the KTA crystals about an axis normal to the plane of the paper, and the BBO crystals about an axis in the plane of the paper, as indicated above the crystals. Mirror reflectances at pump, signal and idler wavelengths are shown in the table.

#126039 - $15.00 USD Received 26 Mar 2010; accepted 13 Apr 2010; published 19 Apr 2010

5.1 Pump beam

The pump source was a Quantel Brilliant b Q-switched Nd:YAG laser operating in MLM at 10 Hz pulse repetition rate. The pulses were approximately 5 ns long, and had 20 GHz bandwidth. The beam diameter out of the laser was approximately 8 mm, and after the telescope it was measured to 4 mm at $1/e^2$ of the peak fluence. The pump energy was limited to 70 mJ in order to keep total fluence (pump plus signal and idler) below 2 J/cm^2. The near and far fields were measured using a CCD camera. The beam quality was estimated to (M_x^2, M_y^2) = (1.8, 1.4) after removing the noise as explained in the subsequent section.

5.2 OPO

Two different OPO configurations with equal resonator length were tested:

- Two KTA crystals in walk-off compensating configuration (denoted KTA-KTA')
- Two KTA crystals in walk-off compensating configuration and two BBO crystals without walk-off compensation (denoted KTA-BBO-KTA'-BBO). The reason for not orienting the BBO crystals for walk-off compensation is that the available BBO crystals were identically cut with respect to the crystallographic axes, so for an interaction with two extraordinary waves, walk-off compensation would reverse the sign of the nonlinear coupling coefficient [14].

First, the KTA-KTA' OPO was tuned to 1.68 μm signal wavelength and optimized with respect to output signal energy. Then the BBO crystals were inserted and tuned without tuning the previously installed crystals. The near and far fields of the signal beam were measured with a pyroelectric camera with 100 μm pitch, at 60 mJ pump energy. The pump energy was monitored behind the final folding mirror by a thermopile detector and the signal pulse energy was measured by another similar detector placed behind a filter removing idler and residual pump. The experimental OPO configurations were also simulated using the same parameters as in the experiments, except for the pump beam which was modeled as a 6th order super-Gaussian MLM beam. Figure 6 shows measured and simulated energy curves for both OPO configurations.

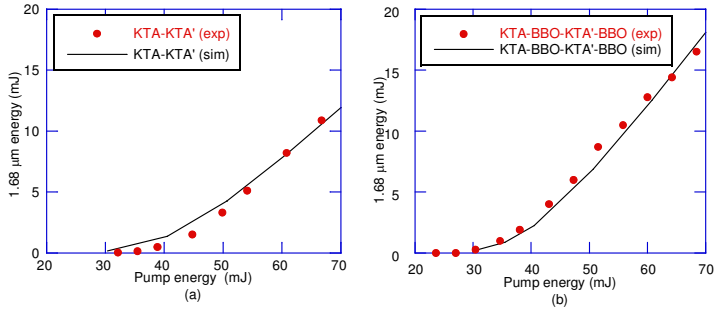

Fig. 6. Measured (red) and simulated (black) signal energy as function of pump energy for the OPO-configurations investigated: KTA-KTA' (a), and KTA-BBO-KTA'-BBO (b). The pump energy is the energy at 1.06 μm impinging the first crystal.

The measured and simulated near and far field beam profiles for both OPO-configurations are shown as contour plots in Fig. 7.

#126039 - $15.00 USD Received 26 Mar 2010; accepted 13 Apr 2010; published 19 Apr 2010

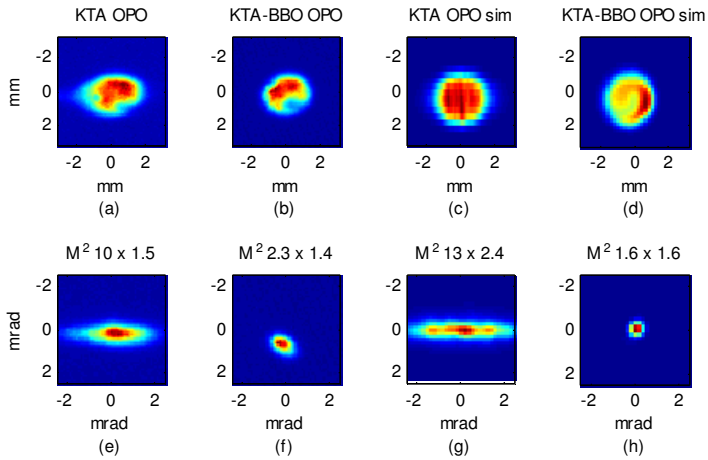

Fig. 7. Images of the signal beam. Measured near (a) and far (e) fields for the KTA-KTA OPO. Corresponding simulated near (c) and far (g) fields. Measured near (b) and far (f) fields for the KTA-BBO-KTA'-BBO OPO. Corresponding simulated near (d) and far (h) fields. The far field measurements are carried out in the focal plane of an f = 1.00 m lens.

The qualitative features agree with those in Fig. 4. The M^2 beam quality measure is based on the second moments of the fluence distributions, which are very sensitive to noise. The data were filtered by an aperture at least twice as wide as the beam and the resulting estimates of M^2 are also shown in Fig. 7. We have used the same apertures for the two OPO configurations, so even if the M^2 estimates are inaccurate, they should at least give a fair comparison of the beam quality from the two OPO's. We notice that inclusion of the BBO crystals strongly reduces the asymmetry of the generated signal beam.

6. Conclusion

We have demonstrated the generation of nearly symmetric, high-quality, high-energy nanosecond pulses using a linear, singly resonant optical parametric oscillator with Fresnel number > 50. The beam quality is achieved by means of nonlinear crystals with orthogonal walk-off planes. Idler absorption also contributes to improved beam quality in the experiment, but the simulations show that the orthogonal critical planes represent the most important mechanism.

Acknowledgments

The authors would like to acknowledge Knut Stenersen, FFI, for valuable comments and discussions concerning the manuscript.

Paper II

High pulse energy and symmetrical far field from an optical parametric oscillator in the red spectral range.

Published in Journal of the European Optical Society Rapid Publications.

DOI: 10.2971/jeos.2011.11058

High pulse energy and symmetrical far field from an optical parametric oscillator in the red spectral range

Gunnar Rustad
gunnar.rustad@ffi.no
Norwegian Defence Research Establishment (FFI), P.O.Box 25, NO-2027 Kjeller, Norway

Øystein Farsund
Norwegian Defence Research Establishment (FFI), P.O.Box 25, NO-2027 Kjeller, Norway

Red pulses with >30 mJ energy and < 0.6 nm bandwidth have been demonstrated using a type 2 phase matched optical parametric oscillator pumped at 532 nm. A symmetrical signal beam with beam diameter-divergence product of 3 mm·mrad was obtained by applying KTA and BBO crystals in the same resonator [DOI: http://dx.doi.org/10.2971/jeos.2011.11058]

Keywords: Optical parametric processes, high energy, beam quality, walk-off

1 INTRODUCTION

Remote sensing applications often require high energy laser-like beams with narrow bandwidth and low divergence at wavelengths that cannot be reached directly with ordinary laser materials. The common way of generating such wavelengths is through optical parametric oscillators (OPOs), sum- or difference frequency generators, or a combination of these. For the new beam to be generated with high conversion efficiency and good beam quality, careful design of the nonlinear optical conversion stage is necessary, in particular with respect to beam size, nonlinear crystal length, and in the case of an OPO, resonator length and output coupling. For an OPO with narrow beams it is usually possible to obtain a good beam quality with a simple resonator because the small gain region provides enough spatial filtering to suppress higher order modes. The interplay between pump beam size and crystal length also is important both for the conversion efficiency and the beam quality. The pump beam size affects the pump intensity, and if this is reduced, the nonlinear crystal must be longer to have sufficient conversion. On the other hand, if the crystal is too long or the pump intensity is too high, then back-conversion (the reverse of the desired nonlinear process) will reduce both the conversion efficiency and the beam quality. For a plane-wave (or top-hat) pump beam it is fairly straight-forward to find the optimal combination of beam size and crystal length, but as most pump beams have a strong transversal and temporal variation of their intensity, finding the optimal OPO parameters becomes increasingly difficult.

For higher pulse energies, the beams need to be larger to keep the intracavity fluence below the threshold for optical damage. It is difficult to obtain good beam quality from such OPOs because the wide gain region offers little spatial filtering. Previously, we have found [1] that for an OPO with flat mirrors pumped by a pulsed beam, the gain and resonator provide sufficient spatial filtering to obtain good beam quality if the resonator Fresnel number, F, is less than or approximately equal to the number of round-trips in the OPO resonator during the pump pulse, N_{rt},

$$\frac{F}{N_{rt}} = \frac{\omega^2/\lambda L}{\tau_p c/2L} \leq 1 \Rightarrow \omega \leq \sqrt{\frac{\tau_p c \lambda}{2}} \qquad (1)$$

where ω is the beam radius, λ is the wavelength of the resonating wave, L is the mirror spacing, τ_p is the pump pulse length and c is the speed of light. For a given pump beam, Eq. (1) can be used to estimate if a good OPO beam quality is possible without additional spatial filtering. In this work, the pump pulse length is ≈5 ns, and the OPO signal wavelength is 665 nm. The maximum pump beam radius for good beam quality is then ≈0.7mm. If the pump fluence is restricted to 1 J/cm^2 to avoid optical damage, we find that good beam quality can be expected from this OPO only if the pump energy is limited to ≈15 mJ.

There are various methods to obtain high beam quality even for higher pump energies. The master-oscillator power-amplifier (MOPA) geometry uses a low energy oscillator to generate good beam quality at the expense of a considerably increased complexity. Unstable resonators can improve the beam quality at the expense of the conversion efficiency [2]. Another approach is to use the natural filtering of the signal far field that is a result of the limited acceptance angle of the nonlinear process in the OPO. This acceptance angle is usefully small only if there is walk-off between the signal and idler beams in the nonlinear crystal, hence type 2 phase matching (PM) is required for collinear phase matching. As the acceptance angle for type 2 PM is highly asymmetric (much larger in the direction of noncritical PM than in the direction of critical PM), the far field of the signal beam from a type 2 phase matched OPO with a large beam diameter is highly asymmetric. Means to work around this include the RISTRA geometry [3] and the use of non-collinear phase

Received November 16, 2011; published December 16, 2011

matching [4]–[6]. In this work we have used another approach in which the far field is improved in both directions (and hence the beam asymmetry is reduced) by using two different nonlinear crystals in the same OPO [7]. Both crystals are type 2 phase matched for the same set of wavelengths, but with orthogonal critical planes the far field narrowing occurs in both directions.

2 Experiment

A major challenge in designing an OPO using the principle of orthogonal critical planes is to find adequate nonlinear crystals, both in terms of nonlinearity and the magnitude and direction of walk-off. Different from most other OPOs, a large walk-off angle is desirable in this design because the acceptance angle is inversely proportional to the walk-off angle. The walk-off direction is either parallel to the slow (signal) or the fast (idler) axis. Crystals in the KTP-family are good choices for the slow-axis walk-off as they both have high nonlinearities and large walk-off angles. In this work we have used a 16 mm long KTA crystal. This length was chosen after simulations of the OPO. There are less good alternatives to choose from for the fast-axis walk-off crystal, but BBO has both a fairly high effective nonlinearity for type 2 phase matching **and** a large walk-off angle. To have a symmetrical signal beam far field, the acceptance angle should be approximately the same in both directions. For the wavelengths in consideration in this work (532 nm pump and 665 nm signal), the acceptance interval for the signal angle in BBO is approximately equal to that of KTA at ≈6 mm · mrad ($L\delta\theta$, crystal length x acceptance angle). Hence we chose a BBO crystal of the same length as the KTA crystal (16 mm) in the experiment. The main draw-back of BBO it that it has significant absorption at the 2660 nm idler wavelength, but we have previously shown that for low pulse rate lasers, this can actually be an advantage for the signal beam quality [1].

The pump laser was a frequency-doubled flash-lamp pumped Nd:YAG laser (Quantel Brilliant B) delivering 5 ns pulses at 10 Hz pulse rate. The pump beam was resized to 4 mm diameter with a telescope, and the pump energy was varied from 0-100 mJ with a half-wave plate and a polarizing beam-splitter. The KTA and BBO crystals both had 8 x 8 mm^2 cross sections. The 40 mm long singly resonant OPO consisted of flat mirrors, the pump was double-passed and the signal output coupling was 42%. The OPO setup is sketched in Fig. 1. For comparison and initial alignment, the OPO was also run with the same mirror spacing, but without the BBO crystal.

3 Results

The signal output energies of the OPO with only the KTA crystal and with both KTA and BBO crystals are shown in Figure 2. Up to 30 mJ was obtained for the KTA-BBO OPO when the OPO was pumped with 100 mJ. It is interesting to note that the BBO crystal clearly contributes to the performance of the OPO although the absorption at the 2660 nm idler is

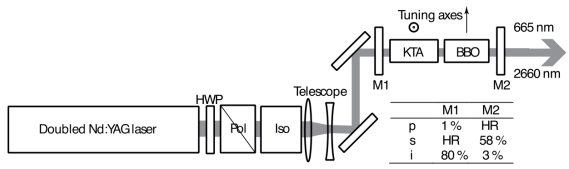

FIG. 1 OPO experimental setup. Pol: Polarizer, Iso: Optical isolator, HWP: Half-wave plate. The directions of the tuning axes are indicated above the KTA and BBO crystals. The table lists the reflectivities of the OPO mirrors at the wavelengths of the pump (p), signal (s) and idler (i)

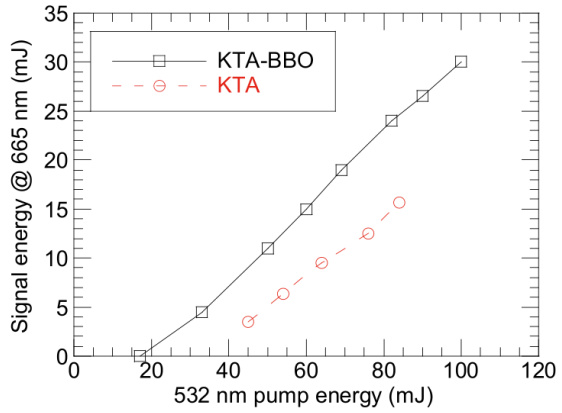

FIG. 2 Signal energy at 665 nm vs. pump energy for the OPO with and without the BBO crystal

70 m^{-1}. The width of the signal spectrum was narrow and the measurement was limited by the 0.6 nm spectral resolution of the Thorlabs CCS175 spectrometer.

The near and far fields of the pump and signal beams were measured with a CCD camera, the far field in the focal plane of a 2 m focal length lens. The images are shown in Fig. 3, and Table 1 lists the calculated beam diameter divergence product measured with 85% energy in bucket. The enhancement in beam quality between the KTA OPO and the KTA-BBO OPO is notable. The beam quality is limited by the width of the far field. This width is about 1 mrad for the KTA-BBO OPO, which is in reasonable agreement with the 0.4 mrad signal acceptance angle in 16 mm KTA and BBO. This divergence is a kind of intrinsic property for this OPO. The beam quality will therefore depend strongly on the pump beam diameter; if the pump beam diameter doubles the mm·mrad product and hence the M^2 value can be expected to be doubled, and vice versa for a smaller pump beam. Further improvement in beam quality with this technique could be obtained by using longer crystals.

TABLE 1 Calculated beam diameter divergence products calculated with 85% energy in bucket from the images in Fig. 3

	532 nm Pump	665 nm KTA-BBO OPO	665 nm KTA OPO
mm·mrad	1.1 × 1.2	3 × 2.6	3 × 12

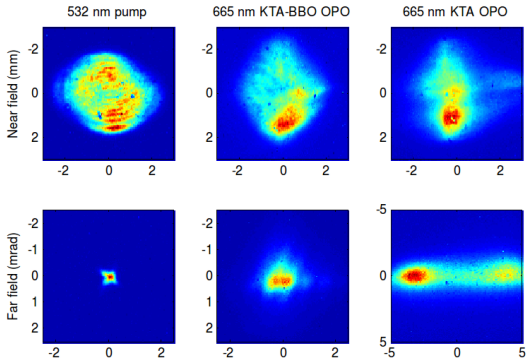

FIG. 3 Measured near (top row) and far (bottom row) fields of the pump (left column) and signal beams from both the KTA-BBO OPO (middle column) and the KTA OPO (right column). Note the different scale in the lower right hand figure.

4 Conclusions

In summary, more than 30 mJ in a symmetrical beam with narrow spectral bandwidth at 665 nm has been obtained from an OPO with two type 2 phase matched crystals with orthogonal critical planes. The beam quality of ≈3 mm · mrad compares favorably with commercial products, e.g. [8]. Scaling to higher pulse energies is possible by using larger pump beams, while maintaining the narrow signal beam far field divergence angle.

References

[1] G. Rustad, G. Arisholm, and O. Farsund, "Effect of idler absorption in pulsed optical parametric oscillators" Opt. Express **19**, 2815-2830 (2011).

[2] S. Pearl, Y. Ehrlich, S. Fastig, and S. Rosenwaks, "Nearly Diffraction-Limited Signal Generated by a Lower Beam-Quality Pump in an Optical Parametric Oscillator" Appl. Optics **42**, 1048-1051 (2003).

[3] A. V. Smith and M. S. Bowers, "Image-rotating cavity designs for improved beam quality in nanosecond optical parametric oscillators" J. Opt. Soc. Am. B **18**, 706-713 (2001).

[4] G. Anstett, G. Goritz, D. Kabs, R. Urschel, R. Wallenstein, and A. Borsutzky, "Reduction of the spectral width and beam divergence of a BBO-OPO by using collinear type-II phase matching and back reflection of the pump beam" Appl. Phys. B **72**, 583-589 (2001).

[5] C. D. Nabors and G. Frangineas, "Optical parametric oscillator with bi-noncolinear, porro prism cavity" in *OSA Trends in Optics and Photonics vol 10*, C. R. Pollock and W. R. Bosenberg, eds., 90-93 (Optical Society of America, Washington, DC, 1997).

[6] V. Pasiskevicius, H. Karlsson, F. Laurell, R. Butkus, V. Smilgevicius, and A. Piskarskas, "High-efficiency parametric oscillation and spectral control in the red spectral region with periodically poled $KTiOPO_4$" Opt. Lett. **26**, 710-712 (2001).

[7] O. Farsund, G. Arisholm, and G. Rustad, "Improved beam quality from a high energy optical parametric oscillator using crystals with orthogonal critical planes" Opt. Express **18**, 9229-9235 (2010).

[8] Ekspla, "NT340 series", www.ekspla.com, 2011.

Paper III

High-pulse-energy, linear optical parametric oscillator with narrow and symmetrical far field

Published in Optics Express.

DOI: 10.1364/OE.21.020171

High-pulse-energy, linear optical parametric oscillator with narrow and symmetrical far field

Øystein Farsund[*] and Gunnar Rustad

Norwegian Defence Research Establishment (FFI), PO Box 25, NO-2027 Kjeller, Norway
[*]*Oystein.Farsund@ffi.no*

Abstract: A new method to obtain a narrow and symmetrical far field from a high-pulse-energy optical parametric oscillator (OPO) with a linear resonator has been tested. The OPO employs two identical nonlinear crystals that are cut for type II phase matching, rotated such that their walk-off planes are orthogonal, and separated by a broadband half-wave plate. The OPO has a simple geometry, can be double-pass pumped, is wavelength tunable and operates stably with high conversion efficiency. The method has been demonstrated in a KTP-based OPO pumped at 1064 nm and a BBO-based OPO pumped at 532 nm, with output pulse energies up to 60 mJ and 75 mJ, respectively.

OCIS codes: (190.4410) Nonlinear optics, parametric processes; (190.4420) Nonlinear optics, transverse effects in; (190.4970) Parametric oscillators and amplifiers.

References and links

1. G. Rustad, G. Arisholm, and Ø. Farsund, "Effect of idler absorption in pulsed optical parametric oscillators," Opt. Express **19**(3), 2815–2830 (2011).
2. C. D. Nabors and G. Frangineas, "Optical parametric oscillator with bi-noncolinear, porro prism cavity," in Advanced Solid State Lasers, OSA Trends in Optics and Photonics, Vol. **10**, (Optical Society of America, Orlando, FL, 1997), 90–93.
3. A. V. Smith and M. S. Bowers, "Image-rotating cavity designs for improved beam quality in nanosecond optical parametric oscillators," J. Opt. Soc. Am. B **18**(5), 706–713 (2001).
4. D. J. Armstrong and A. V. Smith, "Demonstration of improved beam quality in an image-rotating optical parametric oscillator," Opt. Lett. **27**(1), 40–42 (2002).
5. O. Farsund, G. Arisholm, and G. Rustad, "Improved beam quality from a high energy optical parametric oscillator using crystals with orthogonal critical planes," Opt. Express **18**(9), 9229–9235 (2010).
6. W. J. Alford, R. J. Gehr, R. L. Schmitt, A. V. Smith, and G. Arisholm, "Beam tilt and angular dispersion in broad-bandwidth, nanosecond optical parametric oscillators," J. Opt. Soc. Am. B **16**(9), 1525–1532 (1999).
7. G. Arisholm, "General numerical methods for simulating second-order nonlinear interactions in birefringent media," J. Opt. Soc. Am. B **14**(10), 2543–2549 (1997).
8. G. Arisholm, "Advanced numerical simulation models for second-order nonlinear interactions," Proc. SPIE **3685**, 86–97 (1999).
9. D. Eimerl, L. Davis, S. Velsko, E. K. Graham, and A. Zalkin, "Optical, Mechanical, and Thermal-Properties of Barium Borate," J. Appl. Phys. **62**(5), 1968–1983 (1987).
10. D. J. Armstrong, W. J. Alford, T. D. Raymond, A. V. Smith, and M. S. Bowers, "Parametric amplification and oscillation with walkoff-compensating crystals," J. Opt. Soc. Am. B **14**(2), 460–474 (1997).
11. M. Kaucikas, M. Warren, A. Michailovas, R. Antanavicius, and J. J. van Thor, "Beam patterns in an optical parametric oscillator set-up employing walk-off compensating beta barium borate crystals," Laser Phys. **23**(2), 025401 (2013).

1. Introduction

Optical parametric oscillators (OPOs) provide a powerful and potentially efficient means of producing tunable coherent light. The quality of the beams generated by an OPO depends on the beam quality of the pump beam, the details of the resonator geometry and details of the nonlinear process. For low pulse energies, narrow beams can be used, and a properly designed resonator geometry may lead to excellent beam quality. However, in some applications, in particular within the field of remote sensing, high pulse energy in combination with high beam quality is required. This poses a substantial challenge as the

#192125 - $15.00 USD Received 17 Jun 2013; accepted 16 Jul 2013; published 20 Aug 2013

beam then must be made relatively wide to avoid optical damage, and the resonator geometry is no longer able to ensure a high quality beam. We have previously shown that an OPO pumped with nanosecond pulses has potential for generating high beam quality provided that the diameter of the pump beam is smaller than the limit given by [1] $d_{\max} \approx \sqrt{2\tau_p c\lambda}$, where τ_p is the pump pulse length, c is the speed of light in vacuum and λ is the signal wavelength. For 5 ns pulses and 1.6 μm signal wavelength, this limit becomes ~2 mm. If the peak pump fluence is to be held below, say, 2 J/cm^2, this will limit the maximum pump energy for a Gaussian beam to ~35 mJ. For higher pulse energies (or lower damage thresholds), other means must therefore be used to ensure a good beam quality.

The divergence of the signal and idler beams can be restricted by choosing a nonlinear material and interaction with low angular acceptance for the signal. This occurs when there is spatial walk-off between signal and idler in the nonlinear material, as in type 2 collinear critical phase matching. For type 1 phase matching or for quasi-phase matching, this effect cannot be used for collinear phase matching, but is possible for non-collinear phase matching [2]. For OPOs with large beams, but small signal acceptance angle, the far field of the signal beam typically becomes asymmetric, with a narrow far field (and good beam quality) in the direction of signal-idler walk-off and a (much) wider far field in the other direction [3].

There exist several methods to mitigate this problem and create a symmetrical and narrow far field even from a large beam OPO. In the RISTRA ring resonator, the image of the signal beam (but not the polarization) is rotated 90° each round trip, building up spatial coherence in both directions [3, 4]. Nabors and Frangineas [2] used non-collinear pumping to generate signal-idler walk-off and a resonator with a porro-prism to flip the signal beam image. We have previously demonstrated good and symmetrical beam quality using two different type 2 phase matched crystals with orthogonal critical planes (OCP) in the same linear resonator using two-pass pumping [5]. While all approaches have succeeded in generating good beam qualities, they also have some limitations. The OCP requires two different crystals that match each other in terms of birefringence, nonlinearity and wavelength range. The porro-prism OPO cannot be angle tuned, while the RISTRA geometry require materials with relatively high nonlinear gain as the resonator round-trip path is fairly long and the pump cannot be double-passed through the nonlinear material.

Smith and Bowers proposed and simulated a number of approaches to achieve high beam quality from high energy, nanosecond OPOs [3], including the RISTRA. In this work, we demonstrate experimentally one of the other configurations they propose; two type 2 phase matched crystals with orthogonal critical planes in a standing wave cavity with an inter-crystal half-wave plate which rotates the pump and signal polarizations by 90°. This geometry resembles the OCP, but by introducing the half-wave plate, the need for different crystals in the OCP geometry is lifted. The OPO has a simple geometry and two pass pumping ensures a symmetric signal far field [3] as well as high efficiency. The OPO geometry was tested both with two KTP and with two BBO crystals, with 1064 nm and 532 nm pumping wavelength, respectively, at > 100 mJ pump energies.

2. Experiment

The linear OPO resonator was built as sketched in Fig. 1. The OPO was pumped with either the 1064 nm output from a Q-switched 10 Hz pulse-rate flash-lamp pumped Nd:YAG laser generating 5 ns multi longitudinal mode pulses with approximately 20 GHz linewidth (Quantel Brilliant B), or the frequency doubled output of the same laser. The pump energy could be adjusted from 0 to 270 mJ at 1064 nm (0 to 170 mJ at 532 nm) with a half-wave plate and a polarizer, and the pump beam diameter was varied from 3 mm to 7 mm by changing the lenses in the telescope. The input mirror was highly reflective on the signal wavelength, and had high transmission at the pump and idler wavelengths. Two different pairs of crystals were used, as listed in Table 1.

#192125 - $15.00 USD Received 17 Jun 2013; accepted 16 Jul 2013; published 20 Aug 2013

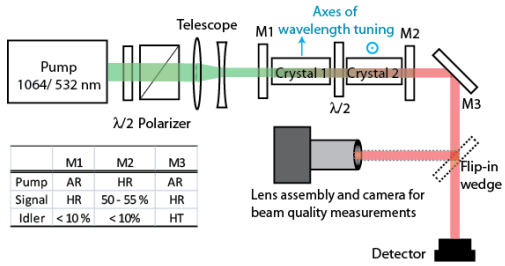

	M1	M2	M3
Pump	AR	HR	AR
Signal	HR	50 - 55 %	HR
Idler	< 10 %	< 10%	HT

Fig. 1. Experimental setup and mirror specifications for the OPOs pumped by either 1064 nm or 532 nm.

Table 1. Nonlinear Crystals Used in the Experiments[a]

Crystal	Length	Cut angle	AR Pump/Signal
BBO	16 mm	23°	532/670
KTP	30 mm	46° (XZ)	1064/1680

[a]All crystals were cut for type 2 phase matching and used in pairs, and the AR-coating also had low loss on the corresponding idler wavelength. The cross sections of the crystals were 8 mm × 8 mm.

A commercial achromatic half-wave plate (Thorlabs AHWP05M-1600 for 1064 nm pump and AHWP05M-600 for 532 nm pump) was placed between the crystals and oriented to give 90° polarization rotation of the pump and signal beams. The output coupler reflected ~50% at the signal wavelength, < 10% at the idler wavelength and was highly reflective at the pump wavelength. Pump reflection was used because the performance of OPOs using nonlinear crystals with relatively low effective nonlinearity benefits strongly from double-pass pumping. Furthermore, two-pass pumping ensures collinear operation even without walk-off compensating crystals [6]. The idler wavelengths, in the 2-3 μm range for the experiments in discussion, were outside the range of the half-wave plate, both in terms of optical transmission and retardation, but they still experienced about 70% transmission and about a half-wave retardation. As shall be seen in Subsection 3.4, the performance of the OPO may still be affected by the half-wave plate because the relative phase of the interacting waves can be changed owing to dispersion of the optical thickness of the half-wave plate.

The crystal lengths, output couplings, and maximum pump energy for each pump beam diameter were determined through extensive simulations using FFI's simulation tool that accounts for all relevant effects [7, 8]. The optimal crystal lengths were found to be 2 × 30 mm KTP for the 1064 nm pumped OPO and 2 × 16 mm BBO for the 532 nm pumped OPO. The main reason for the shorter crystals at the shorter pump wavelength is that the nonlinear optical gain increases with frequency.

3. Results

3.1 Orthogonal vs. parallel critical planes

For a collinear $\chi^{(2)}$ interaction not along one of the crystal axes, there is in general a critical plane, where the phase mismatch varies rapidly with beam direction, and an orthogonal noncritical plane where it does not vary to first order. The OPO with parallel critical planes is equivalent to using one crystal with length equal to the sum of the two crystals, or to a pair of walk-off compensating crystals. The case of orthogonal critical planes (OCP) has the same overall gain; however, the half-wave plate rotates the polarization (but not the image) of the signal and pump beams between the crystals by 90°, thereby creating spatial coherence in both transversal directions [3].

#192125 - $15.00 USD Received 17 Jun 2013; accepted 16 Jul 2013; published 20 Aug 2013

Figure 2 shows the measured near and far fields of the 1680 nm signal beam for both parallel and orthogonal critical planes from a 1064 nm pumped OPO using the KTP crystal pair specified in Table 1. The pump beam diameter was ~4 mm and the pump energy was 80 mJ in this experiment.

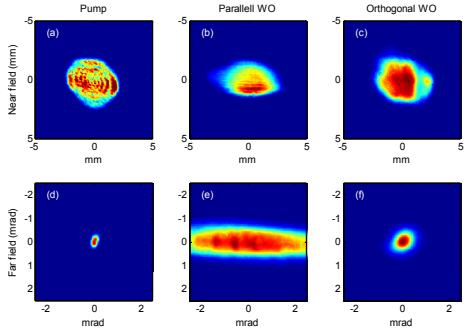

Fig. 2. Near (NF) and far fields (FF) for the 1064 nm pump and OPOs with KTP crystals oriented with parallel or orthogonal critical planes, and about 4 mm pump diameter. The OPO data were acquired at approximately 80 mJ pump energy, corresponding to around 20 mJ pulses at 1680 nm; NF of (a) pump, the case of (b) parallel and (c) orthogonal walk-off planes, FF of (d) pump, the case of (e) parallel and (f) orthogonal walk-off planes.

As expected (and explained above), the far field in the case of OCP is narrowed by the signal acceptance angle in both directions, giving a substantial improvement in beam quality. The output signal pulse energy as function of pump pulse energy is similar for the two configurations, with marginally higher slope and threshold for the case of orthogonal walk-off planes, leading to slightly higher conversion efficiency.

3.2 Pump diameter implication on beam quality

The basic idea of this work, as well as other work described in Section 1, is to use a narrow signal beam acceptance angle to restrict the divergence of the generated beams in an OPO with wide beams. One consequence of this technique is that the size of the far field stays about the same even if the pump diameter is increased, at comparable fluence levels. The beam quality (M^2) therefore increases linearly with the pump diameter; however, it is always much better than in OPOs with comparable beam diameters, but without the far field limiting methods described here [3]. The output signal pulse energy is plotted as function of pump pulse energy and compared for different pump beam diameters in Fig. 3 for the same OPO as described in Subsection 3.1.

#192125 - $15.00 USD Received 17 Jun 2013; accepted 16 Jul 2013; published 20 Aug 2013

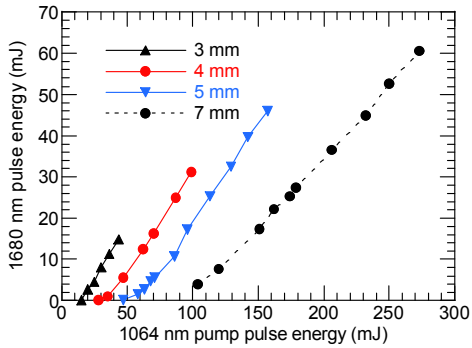

Fig. 3. Signal pulse energy as function of 1064 nm pump pulse energy for KTP OPO with orthogonal critical planes for 3, 4, 5 and 7 mm pump diameter (in terms of 90% energy in bucket).

The slope efficiency is nearly constant, but the threshold pump energy increases with increasing pump beam size. The reduction in slope efficiency for the largest pump beam is due to losses in the limited aperture available in the experiments (slightly below 8 mm × 8 mm). The measured far fields of the signal generated with different pump beam diameters, but at approximately the same pump fluence level (approximately 0.5 J/cm^2), are shown in Fig. 4. We notice that the divergence remains nearly constant, even if the near field diameter changes.

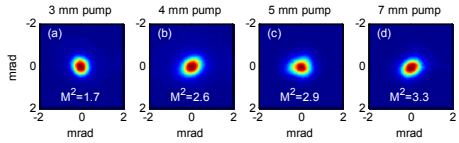

Fig. 4. 1680 nm signal far fields of the 1064 nm pumped OPO with orthogonal critical planes measured for 3 mm to 7 mm pump beam diameters as specified above each image, from (a) smallest to (d) widest pump beam at 25, 62, 96 and 174 mJ pump energy, respectively. The signal far fields are independent of pump beam diameter. The near fields of the signal were approximately 20% narrower than those of the corresponding pump.

3.3 Idler absorption implication on beam quality

The output wavelength of a 532 nm pumped OCP OPO using the BBO crystal pair was varied by angle tuning the BBO crystals (around orthogonal rotation axes). While the nonlinear coupling coefficient is nearly constant at the three wavelengths, the absorption at the idler wavelength varies greatly in BBO. Table 2 lists the idler wavelengths and corresponding absorption.

Table 2. Idler Characteristics at Different Signal Wavelengths[b]

Signal wavelength	Idler wavelength	Idler absorption	Tuning angle
650 nm	2930 nm	283 m^{-1}	23.1°
670 nm	2580 nm	105 m^{-1}	23.6°
720 nm	2037 nm	7 m^{-1}	25.0°

[b]Idler wavelengths and corresponding BBO tuning angles and idler absorption coefficients for signal wavelengths used in Subsection 3.3 [9].

#192125 - $15.00 USD Received 17 Jun 2013; accepted 16 Jul 2013; published 20 Aug 2013

We have previously shown through simulations that at low pulse rates idler absorption may be beneficial for the performance of an OPO [1], as removal of idler prevents detrimental back conversion and makes it possible to operate the OPO at a higher pumping level. Figure 5 shows the output energy as function of the pump energy for the three different wavelengths as well as the beam quality expressed as M^2. Interestingly, increasing the idler absorption from weak (7 m^{-1}) to strong (105 m^{-1} which corresponds to 3.5% single pass transmission) does not affect the output energy from the OPO in a significant manner, but helps to improve the beam quality. This confirms the findings in [1], and originates from less back conversion with higher idler absorption. On the other hand, moving to very strong idler absorption (283 m^{-1}) improves the beam quality further, but at the expense of reduced output energy.

The experiments were carried out using only a 3 mm wide pump beam due to a mechanical damage on one of the BBO crystal faces. We expect a more pronounced effect using a wider pump beam and higher pump energies. During initial experiments, 70-75 mJ of output energy at 670-720 nm was obtained when pumping with 170 mJ in a ~7 mm diameter pump beam.

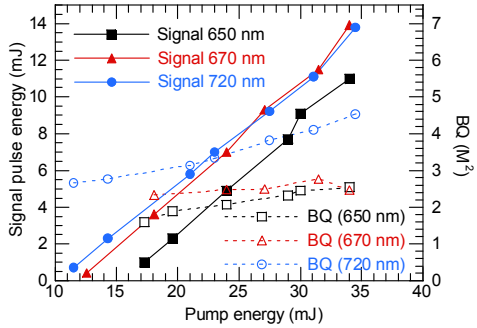

Fig. 5. Measured signal energies (left hand axis) and beam quality (right hand axis) at 650 nm, 670 nm and 720 nm signal wavelengths, corresponding to 283 m^{-1}, 105 m^{-1} and 7 m^{-1} idler absorption in BBO, respectively. The pump beam diameter was approximately 3 mm.

3.4 Effect of relative phase shift in half-wave plate

The different optical thickness of the half-wave plate at the pump, signal and idler wavelengths will result in a shift in the relative phase of the three beams. This may have significant effect on the OPO performance [10, 11], and was studied through simulations. Figure 6 shows the simulated performance of the 1064 nm pumped KTP OPO as function of relative phase shift. It is clear that the signal energy and signal beam quality are strongly affected by this, in particular when the phase shift approaches a half-wave (π).

#192125 - $15.00 USD Received 17 Jun 2013; accepted 16 Jul 2013; published 20 Aug 2013

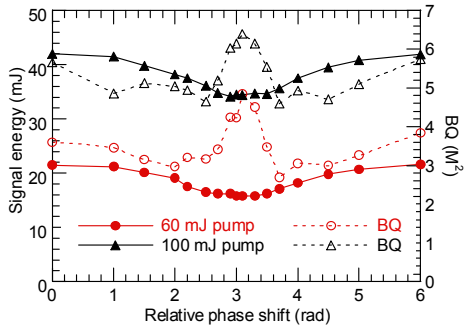

Fig. 6. Simulated performance of a 1064 nm pumped KTP OPO as function of relative phase shift through the half-wave plate. In the simulations, 60 and 100 mJ pump energy in a 4 mm diameter beam were assumed along with the experimental parameters listed in Section 2.

The signal energy is reduced by ~25% in this case when the phase shift is increased from 0 to 2.5 rad, without a reduction in beam quality. However, if the phase shift is further increased towards π, the beam quality is significantly reduced. This happens because the OPO adapts to the phase shift by running on two noncollinear signal modes, as shown in Fig. 7.

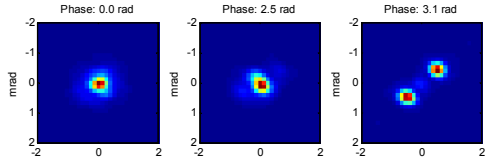

Fig. 7. Far field of simulated KTP OPOs in Fig. 6 at different relative phase shifts.

It was not within the scope of this work to measure the phase shift. However, simulations of the OPO performance show good agreement with experiments when the relative phase shift is about 2.5. In particular, the splitting of the far-field was not observed in the experiment. Figure 8 shows a comparison between experimental results and simulations for 0 and 2.5 rad phase shift for 4 mm pump diameter.

#192125 - $15.00 USD Received 17 Jun 2013; accepted 16 Jul 2013; published 20 Aug 2013

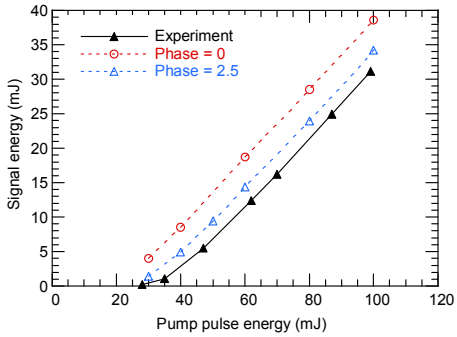

Fig. 8. Comparison of experimental data and simulations for a 1064 nm pumped KTP OPO with 4 mm diameter pump beam. The simulations are for 0 and 2.5 rad relative phase shift in the half-wave plate.

4. Conclusion

The divergence of high-pulse-energy, nanosecond OPOs using type 2 critical phase matching is restricted by the acceptance angle in the walk-off plane. This gives an asymmetric beam quality as long as the crystals in the same cavity are oriented with parallel walk-off planes. However, if two identical crystals oriented with orthogonal walk-off planes are used in the same resonator, and the polarizations of the interacting beams are rotated by 90° (by an achromatic wave plate) between the crystals, the divergence is restricted in both transversal directions, resulting in a symmetric beam with greatly improved beam quality. Two-pass pumping not only increases conversion efficiency, but also consolidates collinear phase matched operation. We have demonstrated this principle by generating a symmetrical beam with pulse energies exceeding 60 mJ at 1680 nm from an OPO with two KTP-crystals, when pumped with 5 ns pulses from a 1064 nm Nd:YAG laser. The same geometry using BBO-crystals was also used to convert 532 nm pulses to 75 mJ pulses in the red. The OPO is easily tunable, and signal wavelengths in the range from 650 nm to 720 nm were demonstrated for the purpose of varying idler absorption in BBO from 283 m^{-1} to 7 m^{-1}. At the 10 Hz pulse rate used in this work, OPOs with high idler absorption perform better than OPOs with low idler absorption, in support of previous simulation results [1]. This is explained by less back conversion in the case of high idler absorption. The relative phase shift induced by the half-wave plate may have substantial effect on the performance of the OPO in terms of conversion efficiency and beam quality, as predicted by simulations. A relative phase shift close to a half-wave should be avoided, since this forces the OPO to run noncollinearly, splitting the far field in two distinct lobes and reducing the beam quality.

Acknowledgments

The authors would like to acknowledge Gunnar Arisholm and Knut Stenersen, FFI, for valuable comments and discussions concerning the manuscript.

Paper IV

Sum frequency generation of high energy and high beam quality ultraviolet pulses

Published in International Journal of Optics.

DOI: 10.1155/2011/737684

Hindawi Publishing Corporation
International Journal of Optics
Volume 2011, Article ID 737684, 4 pages
doi:10.1155/2011/737684

Research Article

Sum-Frequency Generation of High-Energy and High-Beam-Quality Ultraviolet Pulses

Oystein Farsund and Gunnar Rustad

Land and Air Systems Division, Norwegian Defence Research Establishment (FFI), P.O. Box 25, 2027 Kjeller, Norway

Correspondence should be addressed to Oystein Farsund, oystein.farsund@ffi.no

Received 1 July 2011; Accepted 24 August 2011

Academic Editor: Alexandre Kudlinski

Sum-frequency generation of UV pulses exceeding 25 mJ and with beam quality $M^2 \sim 5$ has been demonstrated by mixing the third harmonic pulses of a flash lamp pumped 1.06 μm Nd:YAG laser with 1.7 μm pulses from an optical parametric oscillator pumped by the same laser in a compact setup.

1. Introduction

High-energy ultraviolet (UV) pulses with high beam quality have important lidar applications, such as in standoff detection of biological aerosols and in ozone detection (see, e.g., [1]). While the third (355 nm) and fourth (266 nm) harmonics of the Nd:YAG laser can be used in some applications, the optimal laser wavelength in the above-mentioned applications is close to 290 nm. These applications also demand portable instruments suitable for outdoor experiments and with good beam quality. The topic of this work is generation of high-energy pulses with good beam quality in the 290–300 nm range from a compact setup.

2. Sum-Frequency Generation (SFG) Architecture

There are several ways to reach wavelengths around 300 nm starting out with a single Nd:YAG laser, discussed and demonstrated experimentally for selected UV wavelength ranges by Fix and Ehret [2]. They achieved up to 20 mJ at 320 nm by summing 532 nm radiation with an OPO pumped by 532 nm, starting out with 410 mJ at 1064 nm. The beam quality was not reported; however, the divergence was measured to 0.7 mrad. In our work, ~290 nm is reached by mixing the laser third harmonic with the signal from an optical parametric oscillator (OPO) pumped by the laser's fundamental wavelength in a sum-frequency generation (SFG) process. The output UV wavelength can be varied by tuning the OPO wavelength (and with subsequent tuning of the SFG crystal), but this has not been demonstrated in this work.

Efficient conversion in the SFG stage requires the interacting beams to overlap well both temporally and spatially, and beam divergences smaller than the acceptance angle of the nonlinear interaction. Temporal overlap is ensured by pulse timing and similar pulse lengths. High beam qualities of the interacting beams assure sufficiently low beam divergence in combination with suitable diameters as well as even intensity distributions, which allow for optimal spatial overlap. These matters were discussed in detail in [3], and a remarkable conversion efficiency was demonstrated, however, at the cost of a more complex setup than was the aim of our work. The quality of the UV beam was not reported; however, a far field plot and given beam diameter indicate a UV beam with ~3 mm·mrad at 320 nm, and pulse energy more than 100 mJ.

3. Setup

The experimental setup is depicted and sketched in Figure 1. A flash lamp pumped Nd:YAG laser (Quantel Brilliant B) with 5 ns pulse length (FWHM) was used as laser source in our experiments. The laser was operated in multilongitudinal mode in the experiments. A thin film polarizer located

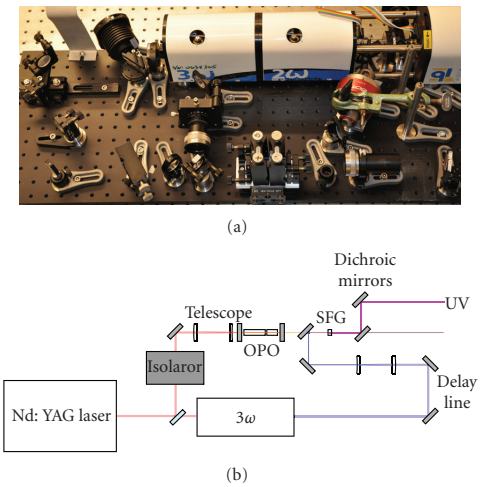

Figure 1: Top view of the experimental setup, depicted (a) and sketched (b). An adequate portion of the pulse energy was split off from the Nd:YAG-laser for OPO pumping. The residual energy generated 3ω using the commercial harmonic generator modules. The OPO signal and 3ω beams were combined in front of the SFG stage.

just after the exit port of the laser cleaned up the polarization state of the pump beam. A beam with adjustable energy was picked off the laser beam by a half-wave plate and another polarizer. This beam was used to pump the OPO, which is described in Section 3.1. The remaining laser energy was passed to the second and third harmonic (3ω) stages (also from Quantel). The two-pass-pumped OPO required an isolator at the pump wavelength to block reflection back to the laser. The pump beam diameter was reduced to ~4 mm by the use of a Galilean telescope (a planoconvex lens, $f = 125$ mm succeeded by a planoconcave lens, $f = -75$ mm). Similarly, a half-wave plate and a thin film polarizer were used to control the 3ω pulse energy, and a Galilean telescope consisting of UV-grade fused silica lenses coated for UV reduced the 3ω beam to approximately the same diameter as the OPO signal beam. Two mirrors allowed the adjustment of spatial overlap (of position and direction) between the 3ω and IR beams. The path length for the 3ω beam could be changed for optimal temporal overlap, and the delay was optimized for maximum output energy by varying the path length during operation of the SFG.

3.1. OPO with Orthogonal Critical Planes. We have previously shown that good beam quality can be obtained from a pulsed OPO if the beam size is small enough that the Fresnel number of the resonator is smaller than the number of roundtrips during the pump pulse [4]:

$$W \leq \sqrt{\frac{\lambda L_r N_{\mathrm{rt}}}{n_r}} = \sqrt{\frac{\lambda t_p c}{2{n_r}^2}}, \quad (1)$$

where W is the beam radius, λ is the resonated wavelength, L_r is the mirror spacing, N_{rt} is the number of resonator round trips during a pump pulse, t_p is the pump pulse length, c is the speed of light in vacuum, and n_r is the average refractive index in the resonator. For a 5 ns pump pulse length and an average refractive index of 1.5, the maximum beam radius is ~0.7 mm. If we restrict the incident pump fluence to 1 J/cm^2 to avoid damage, (1) then limits the maximum pump energy to ~8 mJ. In the high-pulse-energy case studied in this work, the beams need to be significantly larger than the 0.7 mm limit to avoid optical damage, thus other mechanisms are needed to ensure good beam quality.

When using critical type 2 phase matching, the angular spectrum (and hence the beam quality) in the critical direction in the OPO is improved by the limited acceptance angle of the nonlinear interaction. However, since this restriction only occurs in the critical direction, the beams from such OPOs with beams larger than given by (1) often suffer from highly asymmetric beam qualities [5]. Recently, we demonstrated a method to improve the beam quality and symmetry from OPOs with large beams using two different crystals with orthogonal critical planes in the same OPO [6]. By carefully selecting the two nonlinear crystals, narrow acceptance angles in both directions make the far field of the OPO beam symmetrical.

This approach has been used in this work, where the OPO contained one 30 mm long KTP crystal and one 20 mm long BBO crystal, both AR coated and cut for type 2 phase matching of 1.064 μm pumped conversion to 1.7 μm. The crystals had 8 mm × 8 mm apertures, and the pump beam was double passed. A significant part of the 2.84 μm idler wave is absorbed in BBO in this OPO, but as we have previously shown, this idler absorption can actually lead to improved OPO performance for low-pulse-rate OPOs, mainly owing to reduced back conversion in the OPO [4].

In order to reduce the risk of optical damage, the incident pump fluence was restricted to approximately 1.5 J/cm^2, corresponding to 120 mJ pump energy with the given beam diameter (3.6 mm at $1/e^2$ level) and 50% signal output coupling. The OPO was optimized with respect to signal output energy and beam quality, which was measured to $(M_x^2, M_y^2) = (1.6, 2.4)$. The OPO signal energy versus pump energy is shown in Figure 2.

3.2. SFG Stage. Based on simulations of the SFG stage with parameters as described above, a 5 mm long BBO crystal for collinear critical type I phase matching was selected. The crystal was AR coated at 355 nm and 1.7 μm on the input face, and AR coated around 295 nm on the output face. The generated UV beam was separated from the depleted pump beams by means of two dichroic mirrors, and the pulse energies were measured using an Ophir power meter equipped with a 10-AP detector. The near and far fields of the interacting beams were measured with a Spiricon III Pyrocam, the far field in the focal plane of a lens with 2 m focal length.

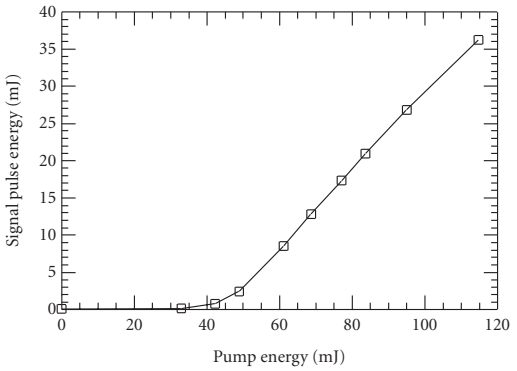

Figure 2: Measured OPO signal energy as function of pump energy.

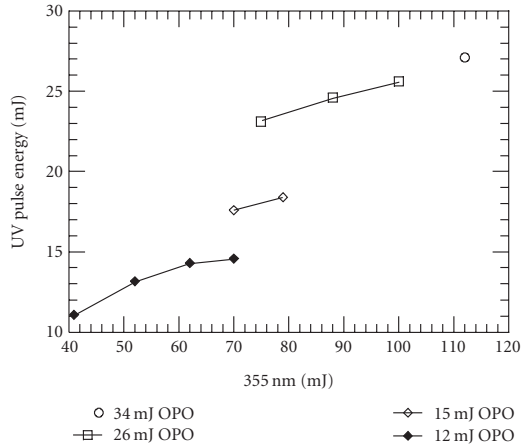

Figure 3: Measured energy of the generated UV pulse for different OPO signal and 3ω pulse energies.

4. SFG Experimental Results

The generated UV pulse energy was measured as function of the 3ω pulse energy while the 1.7 μm pump from the OPO was kept constant. This was repeated for different OPO signal energy levels. The results are summarized in Figure 3, from which we notice that increasing the 1.7 μm pump energy from 12 mJ to 26 mJ increased the UV pulse energy but also that a further increase from 26 mJ to 34 mJ gave only marginally increased output energy, which is mainly attributed to the higher 3ω pulse energy.

The near and far fields of the laser fundamental, OPO signal, 3ω and UV beams were recorded for the purpose of beam quality measurements. Measured near and far field fluence profiles are shown in Figure 4.

Before calculating the (M_x^2, M_y^2) values as given in Table 1, the background was measured and subtracted from the signal. For comparison with other work, we also estimated the diameter-divergence product of the generated UV beam. This was done using the 10%–90% knife-edge values of the measured images in the x- and y-directions. This was found to be 0.76 mm·mrad in the x-direction and 1.2 mm·mrad in the y-direction.

Table 1: Calculated (M_x^2, M_y^2) values (dimensionless) based on measured images of near and far fields.

Beam	M_x^2	M_y^2
Laser fundamental	2.1	2.4
OPO signal (~8 mJ)	1.6	2.4
3ω	3.3	4.7
SFG (~13 mJ)	4.2	5.2

5. Discussion

For a given crystal, local (at a specific point in the beam and a specific time) SFG conversion efficiency depends on the intensity of both incident beams. For 100% conversion, the flux densities of photons must match so that no photons are left over in either beam, and the intensities must be such that there is full conversion at the output end of the crystal. If the intensities are too high, there will be back conversion, which reduces both efficiency and beam quality. High total conversion efficiency requires spatial and temporal overlap of the beams and that each beam has uniform intensity in time and space.

In our experiment, the pulse lengths of the interacting beams are similar. However, as the laser operates in multilongitudinal mode, there will be random spikes on the laser pulse, which will be preserved through the harmonic stages. The OPO signal will also get spikes, but because of the OPO resonator and the nonlinear generation process they will in general not preserve the spike pattern of the pump pulse. Thus, both pulses to the SFG stage have temporal spikes which in general do not overlap, and this reduces conversion efficiency. It should be noted that even if the spikes should overlap, their high intensity might cause back conversion and thus both reduced conversion efficiency and beam quality.

Another limiting factor for the conversion efficiency in our experiment is the nonuniform spatial distributions of the 355 nm and 1.7 μm beams and hence their imperfect spatial overlap. The fluence profile measurements in Figure 4 show the intensity integrated over the entire pulse, so the real mismatch and nonuniformity may be worse if the spatial distribution varies during the pulse. Our laser has a variable reflectivity mirror as output coupler, and it has been shown that such lasers tend to produce beams with time-dependent transverse distribution [7].

For all these reasons, it is predicted that a significant improvement of the efficiency of the SFG process can be obtained with a single-longitudinal mode pump laser and more uniform transversal profiles of the beams incident on the SFG stage.

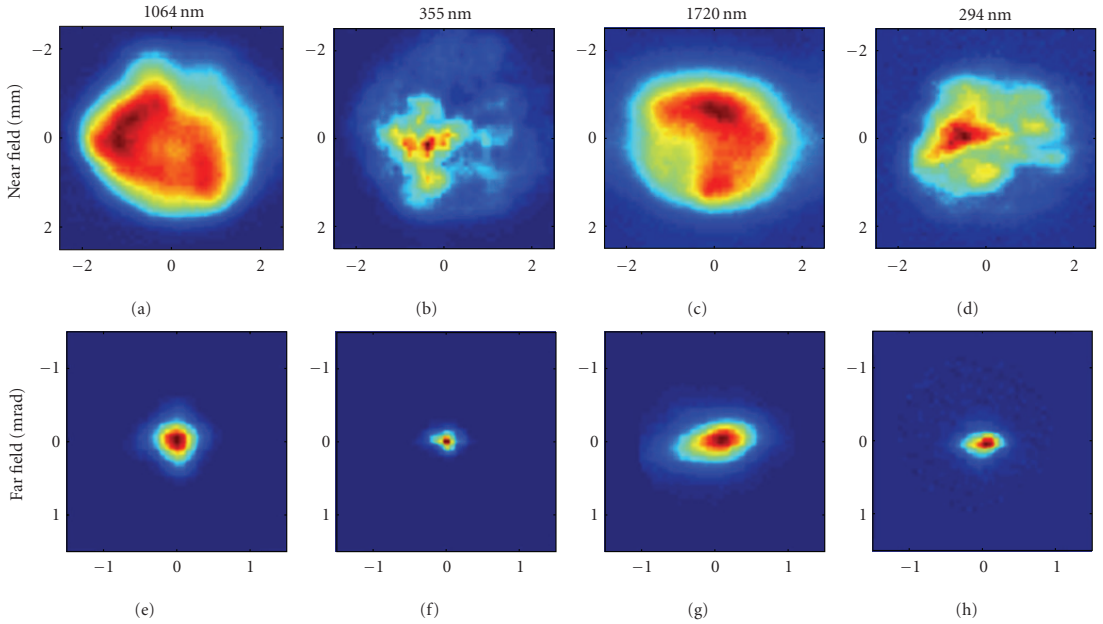

Figure 4: Near- ((a)–(d)) and far-field fluence profiles ((e)–(h)) for a single pulse of the laser fundamental, 3ω, OPO signal, and generated UV beams.

6. Conclusion

In conclusion, we have experimentally demonstrated nanosecond pulses at 294 nm with energy exceeding 25 mJ and beam quality $M^2 \approx 5$ using a single Nd:YAG laser as pump source in a compact setup. The third harmonic of the laser was sum-frequency mixed with the signal from an OPO pumped by the laser fundamental, generating UV pulses in a critical type I collinearly phase matched process. A key to the good beam quality obtained here is the high beam quality of the beam from the OPO. This was obtained using two crystals with orthogonal critical planes in the OPO [6].

References

[1] J. R. Lakowicz, "Protein fluorescence," in *Principles of Fluorescence Spectroscopy*, pp. 446–487, Kluwer Academic/Plenum Publishers, New York, NY, USA, 2nd edition, 1999.

[2] A. Fix and G. Ehret, "Intracavity frequency mixing in pulsed optical parametric oscillators for the efficient generation of continuously tunable ultraviolet radiation," *Applied Physics B*, vol. 67, no. 3, pp. 331–338, 1998.

[3] D. J. Armstrong and A. V. Smith, "All solid-state high-efficiency tunable UV source for airborne or satellite-based ozone DIAL systems," *IEEE Journal on Selected Topics in Quantum Electronics*, vol. 13, no. 3, pp. 721–731, 2007.

[4] G. Rustad, G. Arisholm, and Ø. Farsund, "Effect of idler absorption in pulsed optical parametric oscillators," *Optics Express*, vol. 19, no. 3, pp. 2815–2830, 2011.

[5] A. V. Smith and M. S. Bowers, "Image-rotating cavity designs for improved beam quality in nanosecond optical parametric oscillators," *Journal of the Optical Society of America B*, vol. 18, no. 5, pp. 706–713, 2001.

[6] Ø. Farsund, G. Arisholm, and G. Rustad, "Improved beam quality from a high energy optical parametric oscillator using crystals with orthogonal critical planes," *Optics Express*, vol. 18, no. 9, pp. 9229–9235, 2010.

[7] G. Anstett and R. Wallenstein, "Experimental investigation of the spectro-temporal dynamics of the light pulses of Q-switched Nd:YAG lasers and nanosecond optical parametric oscillators," *Applied Physics B*, vol. 79, no. 7, pp. 827–836, 2004.

Paper V

Standoff detection of biological agents using laser induced fluorescence - a comparison of 294 nm and 355 nm excitation wavelengths

Published in Biomedical Optics Express.

DOI: 10.1364/BOE.3.002964

Biomedical Optics EXPRESS

Standoff detection of biological agents using laser induced fluorescence—a comparison of 294 nm and 355 nm excitation wavelengths

Øystein Farsund,* Gunnar Rustad, and Gunnar Skogan

FFI (Norwegian Defence Research Establishment), Instituttveien 20, Kjeller, NO-2007, Norway
**oystein.farsund@ffi.no*

Abstract: Standoff detection measuring the fluorescence spectra of seven different biological agents excited by 294 nm as well as 355 nm wavelength laser pulses has been undertaken. The biological warfare agent simulants were released in a semi-closed aerosol chamber at 210 m standoff distance and excited by light at either of the two wavelengths using the same instrument. Significant differences in several of the agents' fluorescence response were seen at the two wavelengths. The anthrax simulants' fluorescence responses were almost an order of magnitude stronger at the shorter wavelength excitation. However, most importantly, the fluorescence spectra were significantly more dissimilar at 294 nm than at 355 nm excitation with ~7 nm spectral resolution. This indicates that classification of the substances should be possible with a lower error rate for standoff detection using 294 nm rather than 355 nm excitation wavelength, or even better, utilizing both.

OCIS codes: (170.6280) Spectroscopy, fluorescence and luminescence; (280.1100) Aerosol detection; (280.1415) Biological sensing and sensors; (280.3640) Lidar; (300.2530) Fluorescence, laser-induced.

References and links

1. S. D. Mayor, P. Benda, C. E. Murata, and R. J. Danzig, "Lidars: a key component of urban biodefense," Biosecur. Bioterror. **6**(1), 45–56 (2008).
2. J. Ho, "Future of biological aerosol detection," Anal. Chim. Acta **457**(1), 125–148 (2002).
3. "Laser Based Stand-Off Detection of Biological Agents. Final Report of Task Group SET-098/RTG-55," RTO-TR-SET-098 AC/323(SET-098)TP/265 (2010). *http://www.cso.nato.int/Pubs/rdp.asp?RDP=RTO-TR-SET-098*
4. R. Nyhavn, H. J. F. Moen, Ø. Farsund, and G. Rustad, "Optimal classification of standoff bioaerosol measurements using evolutionary algorithms," Proc. SPIE **8018**, 801806, 801806-13 (2011).
5. K. Baxter, M. Castle, S. Barrington, P. Withers, V. Foot, A. Pickering, and N. Felton, "UK small scale UVLIF lidar for standoff BW detection," Proc. SPIE **6739**, 67390Z, 67390Z-10 (2007).
6. T. Vo-Dinh, *Biomedical Photonics Handbook* (CRC Press, Boca Raton, FL, 2003).
7. J. R. Lakowicz, *Principles of Fluorescence Spectroscopy* (Kluwer Academic/Plenum, New York, 1999).
8. G. W. Faris, R. A. Copeland, K. Mortelmans, and B. V. Bronk, "Spectrally resolved absolute fluorescence cross sections for bacillus spores," Appl. Opt. **36**(4), 958–967 (1997).
9. Y. L. Pan, J. D. Eversole, P. H. Kaye, V. Foot, R. G. Pinnick, S. C. Hill, M. W. Mayo, J. R. Bottiger, A. L. Huston, V. Sivaprakasam, and R. K. Chang, "Bio-aerosol fluorescence," in *Optics of Biological Particles*, NATO science series, Vol. 238 of Series II, Mathematics, Physics and Chemistry, A. Hoekstra, V. Maltsev, and G. Videen, eds. (Springer, Dordrecht, 2007), pp 63–164.
10. P. Jonsson, F. Kullander, C. Vahlberg, P. Jelger, M. Tiihonen, P. Wasterby, T. Tjarnhage, and M. Lindgren, "Spectral detection of ultraviolet laser induced fluorescence from individual bioaerosol particles," Proc. SPIE **6398**, 63980F, 63980F-12 (2006).
11. Ø. Farsund, G. Rustad, I. Kåsen, and T. V. Haavardsholm, "Required Spectral Resolution for Bioaerosol Detection Algorithms Using Standoff Laser-Induced Fluorescence Measurements," IEEE Sens. J. **10**(3), 655–661 (2010).
12. P. Jonsson, M. Elmqvist, O. Gustafsson, F. Kullander, R. Persson, G. Olofsson, T. Tjarnhage, O. Farsund, T. V. Haavardsholm, and G. Rustad, "Evaluation of biological aerosol stand-off detection at a field trial," Proc. SPIE **7484**, 748400I (2009).
13. O. Farsund and G. Rustad, "Sum-Frequency Generation of High-Energy and High-Beam-Quality Ultraviolet Pulses," Int. J. Opt. **2011**, 737684 (2011).
14. G. G. Guilbault, *Practical Fluorescence* (M. Dekker, New York, 1990).

#175155 - $15.00 USD Received 30 Aug 2012; revised 15 Oct 2012; accepted 16 Oct 2012; pub. 24 Oct 2012

15. R. M. Measures, *Laser Remote Sensing—Fundamentals and Applications* (Krieger, Malabar, FL, 1992).
16. J. R. Simard, G. Roy, P. Mathieu, V. Larochelle, J. McFee, and J. Ho, "Standoff sensing of bioaerosols using intensified range-gated spectral analysis of laser-induced fluorescence," IEEE Trans. Geosci. Rem. Sens. **42**(4), 865–874 (2004).
17. S. C. Hill, R. G. Pinnick, S. Niles, Y.-L. Pan, S. Holler, R. K. Chang, J. Bottiger, B. T. Chen, C.-S. Orr, and G. Feather, "Real-time measurement of fluorescence spectra from single airborne biological particles," Field Anal. Chem. Technol. **3**(4-5), 221–239 (1999).
18. C. Laflamme, J. R. Simard, S. Buteau, P. Lahaie, D. Nadeau, B. Déry, O. Houle, P. Mathieu, G. Roy, J. Ho, and C. Duchaine, "Effect of growth media and washing on the spectral signatures of aerosolized biological simulants," Appl. Opt. **50**(6), 788–796 (2011).
19. M. Jerrett, R. T. Burnett, C. A. Pope 3rd, K. Ito, G. Thurston, D. Krewski, Y. L. Shi, E. Calle, and M. Thun, "Long-term ozone exposure and mortality," N. Engl. J. Med. **360**(11), 1085–1095 (2009).
20. D. B. Wetlaufer, *Ultraviolet Spectra of Proteins and Amino Acids*, Vol. 17 of Advances in Protein Chemistry (Academic, 1962), pp. 303–390.
21. MODTRAN, Air Force Research Labs, Hanscom AFB, MA, 2008.
22. Ø. Farsund, G. Arisholm, and G. Rustad, "Improved beam quality from a high energy optical parametric oscillator using crystals with orthogonal critical planes," Opt. Express **18**(9), 9229–9235 (2010).
23. S. Buteau, J.-R. Simard, and S. Rowsell, "Bioaerosols standoff detection simultaneously refereed with particle concentration (ppl) and viability units (ACPLA)," Proc. SPIE **7484**, 748408, 748408-12 (2009).
24. A. Furiga, G. Pierre, M. Glories, P. Aimar, C. Roques, C. Causserand, and M. Berge, "Effects of ionic strength on bacteriophage MS2 behavior and their implications for the assessment of virus retention by ultrafiltration membranes," Appl. Environ. Microbiol. **77**(1), 229–236 (2011).
25. International Standardisation Organisation, "Water Quality—Detection and Enumeration of Bacteriophages—Part 1: Enumeration of F-Specific RNA Bacteriophages," EN ISO 10705–1 (International Standardisation Organisation, Geneva, Switzerland, 1995).
26. V. Sivaprakasam, H. B. Lin, A. L. Huston, and J. D. Eversole, "Spectral characterization of biological aerosol particles using two-wavelength excited laser-induced fluorescence and elastic scattering measurements," Opt. Express **19**(7), 6191–6208 (2011).
27. V. Sivaprakasam, A. Huston, C. Scotto, and J. Eversole, "Multiple UV wavelength excitation and fluorescence of bioaerosols," Opt. Express **12**(19), 4457–4466 (2004).
28. C. Laflamme, J.-R. Simard, S. Buteau, P. Lahaie, D. Nadeau, B. Déry, O. Houle, P. Mathieu, G. Roy, J. Ho, and C. Duchaine, "Effect of growth media and washing on the spectral signatures of aerosolized biological simulants," Appl. Opt. **50**(6), 788–796 (2011).
29. Y. L. Pan, S. C. Hill, R. G. Pinnick, H. Huang, J. R. Bottiger, and R. K. Chang, "Fluorescence spectra of atmospheric aerosol particles measured using one or two excitation wavelengths: comparison of classification schemes employing different emission and scattering results," Opt. Express **18**(12), 12436–12457 (2010).
30. H. C. Huang, Y. L. Pan, S. C. Hill, R. G. Pinnick, and R. K. Chang, "Real-time measurement of dual-wavelength laser-induced fluorescence spectra of individual aerosol particles," Opt. Express **16**(21), 16523–16528 (2008).
31. M. Seaver, D. C. Roselle, J. F. Pinto, and J. D. Eversole, "Absolute emission spectra from Bacillus subtilis and Escherichia coli vegetative cells in solution," Appl. Opt. **37**(22), 5344–5347 (1998).
32. T. V. Haavardsholm, Ø. Farsund, and G. Rustad, "Biological aerosol standoff detection and agent discrimination based on experimental UV laser induced fluorescence data," presented at *2008 Algorithm Workshop*, DTRA and JSTO (Baltimore, MD, Nov. 4–6, 2008).

1. Introduction

Standoff detection of biological aerosols (bioaerosols) has been identified as an important means to reduce the consequences of an eventual bioaerosol attack, due to its early warning capability [1], and it also has significant potential in environmental monitoring [2]. The majority of current standoff instruments detect aerosolized biological agents using ultraviolet laser induced fluorescence (UVLIF) [3]. While early instruments measured the fluorescence in one or a few spectral bands, modern instruments tend to have greater spectral resolution [4,5]. These instruments commonly use the third or fourth harmonic of a Q-switched Nd:YAG laser as excitation source. Such a laser and harmonic stages are commercially available and deliver pulses of appropriate duration and sufficient energy for detection up to about one km standoff distance. However, there are drawbacks with the commercially available wavelengths. While excitation wavelengths around 350 nm seem to be customary [3], the most important naturally occurring fluorophores, tryptophan, phenylalanine and tyrosine, absorb most efficiently at wavelengths considerably shorter than 355 nm [6, p. 3-17], [7, p. 65]. At the fourth harmonic of Nd:YAG (266 nm), on the other hand, absorption by atmospheric ozone close to the ground can dramatically reduce standoff distance. More specifically, based on laboratory measurements at several excitation wavelengths, the region

#175155 - $15.00 USD Received 30 Aug 2012; revised 15 Oct 2012; accepted 16 Oct 2012; pub. 24 Oct 2012

around 280 nm has been held to be more efficient in terms of excitation for fluorescence than 355 nm [6, p. 28-12], [8–10].

FFI has previously developed a UVLIF standoff instrument using a 355 nm laser light source for the excitation of the bioaerosols with high spectral resolution of the detected fluorescence. This biological lidar instrument (hereafter *biolidar*) was used in several field experiments [11,12]. Recently, a compact 294 nm pulsed laser source was developed by means of nonlinear conversion of a commercial Nd:YAG laser [13]. This source was integrated in the lidar instrument, and standoff detection experiments using a semi-closed release chamber were carried out. Seven different agents used for the simulation of biological warfare agents (BWA) were released at 210 m standoff distance, and their fluorescence spectra when excited at the two different wavelengths were measured at standoff distance.

In the following, we give a brief theoretically based motivation for choosing a more difficult accessible excitation wavelength, followed by a description of the lidar instrument and the experimental setup. Finally, the measurement results are presented, discussed and compared to single aerosol particle measurements reported by others.

2. Theory and motivation

The fact that some parts of the biological material emit fluorescence when exposed to ultraviolet light is utilized [6, p. 3-17], [7, p. 63], [14, pp. 575, 776]. The biolidar uses range-gated, ultraviolet laser induced fluorescence to detect biological aerosols at a distance. Assuming a laser emitting a pulse propagating through a column of air before being inelastically scattered by aerosols within a probe volume confined by the field of view (perfectly overlapping the laser beam) and range gating, the return signal impinging the ICCD camera, can be described by a simplified form of the lidar equation [15, pp. 237–256], [16]:

$$E(\lambda, r) = E_L K_0(\lambda) T(\lambda, r) \frac{A_0}{r^2} N(r) \frac{\sigma^F(\lambda_L, \lambda)}{4\pi} \frac{c\tau_d}{2} \tag{1}$$

The intention of this work was to investigate the fluorescence response in terms of magnitude and spectral features as function of two different excitation (laser) wavelengths (λ_L). Experiments allow for good control over several parameters; the laser pulse energy (E_L), geometry (area of collecting optics, A_0, and standoff distance, r) and detector integration time (τ_d). The number density of aerosol particles in the probed volume (N) can be measured indirectly for example by a particle counter or slit sampler. Based on instrument component specifications, the instrument spectral response (K_0) may be calculated. We are thus able to measure a combination of the fluorescence scattering cross section (σ^F) with atmospheric transmission (T) and other inelastic scattering processes, such as Raman scattering, isolating it from instrument characteristics and normalized with respect to a measure of aerosol scatterers.

The main reason for using 355 nm laser light is that it is easily available through third harmonic generation of the 1064 nm pulses from a Nd:YAG laser. The main substance that fluoresces after 355 nm excitation is the molecule NADH. This is the reduced form of nicotinamide adenine dinucleotide (NAD^+), and is important in cell respiration and hence metabolism. NADH is therefore present in bacteria and other living cells [14, p. 776], but to a lesser degree in spores or viruses. We have previously seen that the fluorescence following 355 nm excitation of various substances exhibit sufficient dissimilarities that the different substances can be classified [4,11,12], but it is a challenging task as the differences between the fluorescence spectra are relatively small. It is well known that the growth medium and the preparation the agents will influence the spectral signatures; and thereby distort the ability to discriminate agents [17,18]. The effects of the growth medium and agent preparation have not been studied in the present work. Among the most important biological fluorophores, tryptophan is not excited in the 355 nm laser approach because tryptophan requires excitation at wavelengths below ~310 nm [6, p. 28–12], see Fig. 1 (a). As tryptophan is an amino acid and therefore present in all biological material, this is an important limitation of the 355 nm excitation scheme. Tryptophan can be excited with laser pulses at 266 nm, which is the fourth

#175155 - $15.00 USD Received 30 Aug 2012; revised 15 Oct 2012; accepted 16 Oct 2012; pub. 24 Oct 2012

harmonic of the Nd:YAG laser, and this has been used in some instruments [5]. However, presence of ozone close to the ground will absorb this wavelength. For example, at 100 ppb O_3 concentration, which can occur in urban areas in the summer [19], 266 nm light experiences ~90% loss per km. For comparison, at 280 nm and 290 nm, the corresponding loss is ~60% and ~30%, respectively, which affects the lidar return signal accordingly (through T(λ,r) in Eq. (1)), see Fig. 1 (b). As the absorption cross section for tryptophan is significantly larger for 280 nm than 266 nm, it is of interest to examine wavelengths in the 280-290 nm range for their suitability in standoff detection of biological aerosols. This has been the topic of this work.

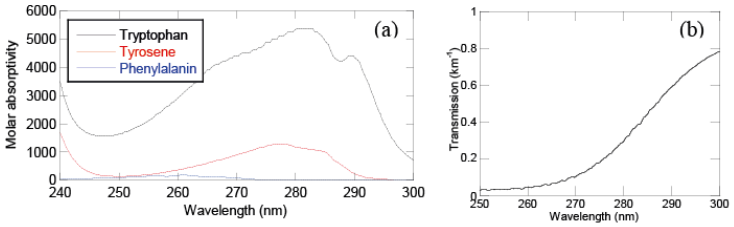

Fig. 1. (a) Absorption spectra for the most important fluorescing amino acids; tryptophan, tyrosine and phenylalanine (spectra taken from [20]). (b) Calculated transmission through 1 km of USTD atmosphere with 100 ppb O_3 using MODTRAN [21].

3. Experiment

3.1 Lidar

A sketch of the FFI biolidar and its key figures used during the experiment are shown in Fig. 2. Laser light is sent out on-axis of the optical telescope that collects the return fluorescence. This is spectrally resolved through a spectrograph and detected with a range gated intensified CCD (ICCD) camera with ~7 nm spectral resolution [12].

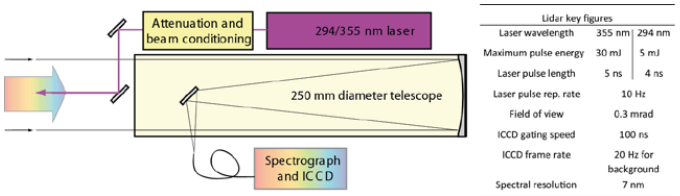

Fig. 2. Sketch of the lidar and its key figures. Pulse energy levels were restricted because of unstable Nd:YAG laser operation at high pulse energies during field use.

Both the fundamental wavelength and the frequency tripled output from a frequency tripled flash-lamp pumped Nd:YAG laser was used to extend the capacity to shorter wavelength UV. We used an optical parametric oscillator (OPO) pumped by the laser fundamental wavelength to generate 1.7 μm radiation, with which 294 nm was generated by sum frequency mixing with 355 nm using a nonlinear crystal (BBO) [13]. The beam quality was suitable for stand-off detection owing to the orthogonal critical planes geometry used in the large-beam OPO [22]. Ideally, an even shorter UV wavelength is preferential, but transmission properties in the optical materials in the current setup limited the wavelength to 294 nm. Both the 294 nm beam and the 355 nm beams could be used as the lidar excitation source. Minor modifications to the setup would allow for automatic dual wavelength operation, for example shot-to-shot alteration. The optical layout is shown in Fig. 3(a).

The ICCD camera gating was set according to the distance to and size of the aerosol release chamber, to approximately 100 ns which was significantly greater than the pulse

#175155 - $15.00 USD Received 30 Aug 2012; revised 15 Oct 2012; accepted 16 Oct 2012; pub. 24 Oct 2012

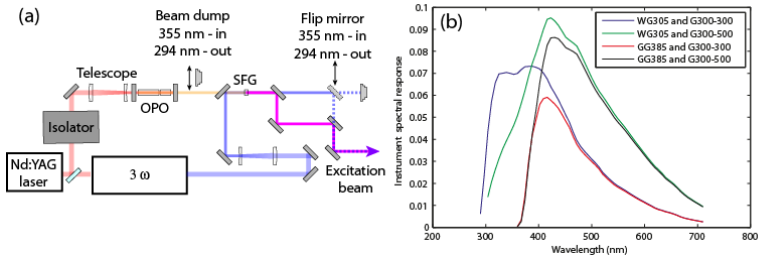

Fig. 3. (a) Excitation laser of the lidar. A 294 nm beam was generated by sum frequency mixing the 1.7 μm OPO signal with the third harmonic (355 nm) of the laser. 294 nm or 355 nm excitation wavelength was selected by adjusting the flip mirror and beam dump, as is explained in the figure. (b) Calculated instrument spectral responses of the biolidar for the four different combinations of color glass filter and grating used, including the ICCD quantum efficiency.

length and the biological aerosol fluorescence life time (approximately 3.1 ns and 0.4 ns for tryptophan and NADH, respectively [7, pp. 63–64, 488]). The average laser power was measured immediately prior to dissemination of the agent. During 294 nm operation, the output pulse energy was 3-5 mJ, whereas approximately 30 mJ was used during 355 nm operation. These levels were used to allow for stable operation. We have demonstrated more than 25 mJ operation of the 294 nm light source in a fine-tuned experiment in the laboratory [13]; however, unstable operation of the commercial frequency tripled Nd:YAG laser with changing ambient temperature affected the stability of the UV pulse energy severely. The Andor Shamrock 163i spectrograph was employed with either one of two different gratings during the experiment, both with 300 lines/mm ruling, but with different blaze angles (optimized for transmission at 300 nm and 500 nm, respectively). To reduce elastic backscatter levels to avoid saturation of the Andor DH720-18H-83 ICCD camera, WG 305 and CVI LP385 (corresponds to Schott GG385) color glass filters were used for 294 nm and 355 nm excitation, respectively. The calculated total instrument spectral responses for the four different configurations (including mirrors, optical fiber and camera) corresponding to K_0 of Eq. (1), are shown in Fig. 3(b). All spectra presented in Figs. 9–10 have been corrected for the corresponding spectral response. The camera operated at twice the 10 Hz laser pulse repetition rate to acquire one background spectrum for each fluorescence spectrum. The measured spectrum was corrected on the fly.

3.2 Agent dissemination and referencing

The 5 m long semi-closed release chamber had 1 m × 1 m air curtains at each end to confine the aerosols within the chamber without the use of windows (windows would have rendered the measurements impossible as they fluoresce significantly after UV excitation). The laser diameter was only about 100 mm inside the chamber, thus filling the entire chamber with aerosols would be needless in terms of amount of agent use and time to fill and evacuate the chamber. We therefore fixed a 500 mm diameter and 3 m long ventilation duct between the air curtains of the container, into which the agents were released using aerosol generators and a fan placed at the far end (with respect to the lidar), see Fig. 4(a). The particle concentration inside the duct was monitored by means of an Aerodynamic Particle Sizer (APS 3321 from TSI Inc), which had its inlet located half way down the duct; see Fig. 4(b).

The APS measured the aerodynamic diameter distribution of the aerosols. A background measurement was carried out prior to the release. The background was subtracted from the measurement carried out during the release, giving us a reference for the particle number and size distribution of the dissemination. The integral over all particle sizes released was used for reference (which measures the particle concentration, “particles per liter air,” *ppl*), as a slit

#175155 - $15.00 USD Received 30 Aug 2012; revised 15 Oct 2012; accepted 16 Oct 2012; pub. 24 Oct 2012

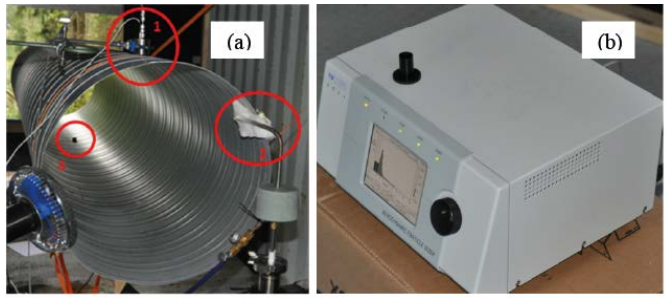

Fig. 4. (a) Ø500 mm duct through which the lidar was directed, and into which the aerosols were released either wet (1) or dry (2). (b) The APS measured the aerosol size distribution, and was located with its inlet protruding into the pipe (position 3 in Fig. 4(a)).

sampler (which gives measurements of viability units, "Agent Containing Particles per Liter of Air," *ACPLA*) was not used in the experiments. UVLIF standoff measurements refereed with particle concentration and viability units have been reported, and the *ACPLA* to *ppl* ratio in their experiments varied between 1% and 30% [23].

Agents dissolved in water solution were disseminated using a 48 kHz ultrasonic spray nozzle (from Sono-Tek Corporation). Dry agents were released using custom built gear. The lidar was located at 210 meters distance from the release chamber, see Fig. 5. The laser beam was centered in the test tube and both the 355 nm and 294 nm beams had diameters of approximately 10 cm inside the chamber.

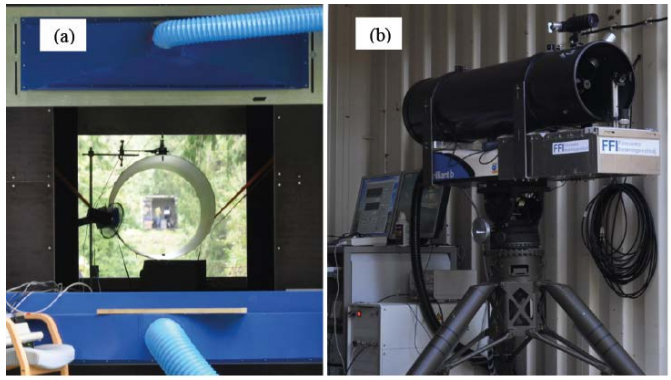

Fig. 5. (a) The lidar as seen through the release chamber, 210 m behind. The size of the laser beam inside the test chamber was about 100 mm diameter, i.e., significantly smaller than the 500 mm cross section of the release duct. (b) Photo of the FFI biolidar.

3.3 Biological agents disseminated in the experiments

Seven different agents were released during the experiments. BG is spores of *Bacillus atrophaeus*. The spores originate from *Dugway Proving Ground*, batch #026, lot #19076-03268. The spores were suspended in deionized water at a concentration of 8 mg/ml. BG spores are commonly used as a BW simulant for *Bacillus anthracis* spores. BT is spores of *Bacillus thuringiensis* (we used a commercial preparation called Turex, normally used as a biological insecticide). BT is another simulant for anthrax spores. EH is *Pantoea agglomerans,* originating from the *American Type Culture Collection* (ATCC 33243). The

#175155 - $15.00 USD Received 30 Aug 2012; revised 15 Oct 2012; accepted 16 Oct 2012; pub. 24 Oct 2012

culture was cultivated overnight at 30°C in nutrient broth from Merck (5.0 g/l peptone from meat and 3.0 g/l meat extract). EH was used as a simulant for pathogenic gram-negative bacteria, like *Francisella tularemia* (rabbit fever) and *Yersinia pestis* (plague). *E.coli* is the gram negative bacterium *Escherichia coli*, from *Deutsche Sammlung von Mikroorganismen und Zellkulturen* (DSM 4230). This culture was also grown at 30°C overnight in nutrient broth. *E.coli* can be used as a simulant for pathogenic gram-negative bacteria. MS2 is a bacteriophage, i.e., a virus infecting bacteria. MS2 was inoculated into a log phase *E.coli* culture (DSM 5695) and grown overnight at 37°C in LB medium (10 g/l tryptone, 5 g/l yeast extract and 10 g/l NaCl). After cultivation, bacteria were removed by centrifuging at 2000 *g* for ten minutes, followed by filtration using a 0.2 µm filter (from Whatman) [24]. The bacteriophage MS2 was enumerated according to the double-layer-agar method [25]. MS2 is used as a simulant for pathogenic viruses, e.g. smallpox or ebola. OA is ovalbumin. We used OA named Sigma-Aldrich A5253. Fumed silica, Sigma-Aldrich S5505, was added in a concentration of 1% to make the OA more "volatile". Ovalbumin is used as a simulant for toxins, e.g. ricin. SM is *Serratia marcescens* originating from *Collection de Institut Pasteur* (CIP 53.90). The culture was grown overnight at 30°C in nutrient broth. SM was used as a simulant for pathogenic gram-negative bacteria. All agents were released in an aqueous solution (deionized water), except for BT and OA, which were disseminated dry (powder).

4. Results

The aim of the experiments was to compare the fluorescence spectra in terms of responsivity and spectral features as function of the laser excitation wavelength and pulse energy. The return spectrum between 280 nm and 630 nm was measured with the camera. As this could potentially lead to problems with overlapping of the second order of the high frequency part of the spectrum with the first order of the low frequency part in the spectrograph, we chose to only regard the 280-560 nm spectral range when exciting the agent at 294 nm. For 355 nm excitation we used data up to 610 nm. Our previous measurements at 355 nm excitation have shown that the spectral range above ~600 nm does not contain useful information (see also measured results in [6, p. 28-12], [9]).The raw data consisted of 205 channels at 10 Hz sample rate. An example of the raw data acquired during the release of OA is shown in Fig. 6(a).

The time-averaged spectrum in Fig. 6(b) is from a time interval with weak fluorescence signal and shows several distinct lines. The spikes seen in the measured spectra do not originate from the fluorescence of the agent in consideration. First of all, elastic scattering at the laser wavelength is seen even though the radiation at the excitation wavelength is attenuated by several orders of magnitude. Moreover, Raman-scattering of atmospheric constituents, in particular for N_2 shifting the wavenumber by 2330 cm^{-1} [15, p. 107] (to approximately 315 nm for 294 nm excitation), are inevitable. 355 nm elastic scattering also appears when operating the lidar at 294 nm, because our source uses 355 nm to generate the

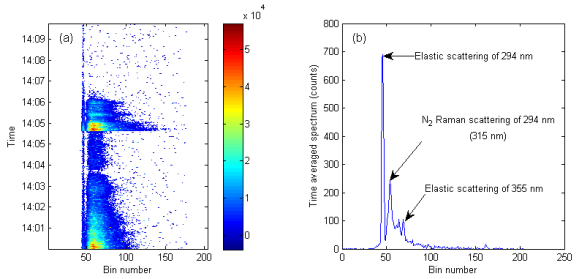

Fig. 6. (a) Example of raw data during measurement with 294 nm excitation and dissemination of OA (recorded fluorescence spectra as function of time). Color coding indicates signal strength (counts), and a bin corresponds to a spectral channel. (b) Time average of the spectra measured between 14:07 and 14:09 as shown in (a) (i.e., at weak measured fluorescence).

#175155 - $15.00 USD Received 30 Aug 2012; revised 15 Oct 2012; accepted 16 Oct 2012; pub. 24 Oct 2012

294 nm radiation. The optical leakage at 355 nm is less than 10^{-5}, but still sufficiently large that the elastic backscatter be comparable with the fluorescence following 294 nm excitation. The locations of these lines were used to calibrate the wavelength axis. The spectral features of the agents were extracted from measurements during intervals of considerable fluorescence signal and correspondingly high particle counts on the APS reference instrument, disregarding intervals with little or no fluorescence.

4.1 Response linearity with respect to agent quantity

An important assumption when averaging spectral features at different agent concentration levels, is that the features, or shape, of the fluorescence spectrum are the same for different quantities of aerosols in the measurement volume. This is tantamount to operating the laser power below a certain threshold, where fluorescence intensity is proportional to the illumination [9]. Sivaprakasam *et.al* showed that the fluorescent emission of bioaersols was linear with the incident laser fluence up to several mJ/cm^2 in experiments on individual bioaerosol particles [26]. The average of the currently measured spectra at significantly different agent concentration levels are plotted in Fig. 7(a) and normalized with respect to the particle concentration measured by the APS in Fig. 7(b).

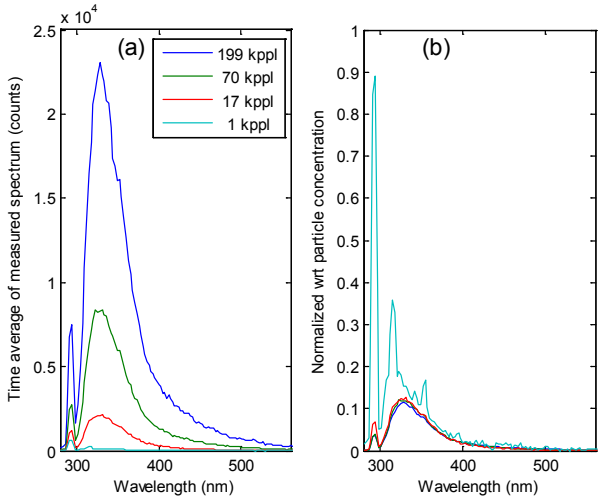

Fig. 7. (a) Spectral average of measurements acquired during different particle concentration levels (average of measured particle concentration during the acquisition); different agent concentration levels impose different signal levels. (b) Spectra normalized with respect to the particle concentration as measured by the APS coincide at different agent concentrations until the signal approaches background level, where other effects become prominent (same color coding as in (a)).

The similar spectral shapes indicate that the assumption is appropriate also in the current measurements. At low signal level we recognize the characteristic spikes related to elastic backscatter and Raman-scattering. The result is also important for the estimation of agent quantity within the probe volume, as determined by the laser cross section (or field of view if it is smaller) inside the gating depth.

4.2 Agent spectra at different excitation wavelengths

The most important parameter for the selection of excitation wavelength in terms of standoff detection sensitivity is the fluorescence cross section of the agent in consideration, σ^F of Eq.

#175155 - $15.00 USD Received 30 Aug 2012; revised 15 Oct 2012; accepted 16 Oct 2012; pub. 24 Oct 2012

(1), which depends on aerosol particle size. Sivaprakasam *et.al* measured laser induced fluorescence of single aerosol particles, and showed that the elastic and fluorescence scattering scale similarly with particle size, thus the size dependence may be eliminated by normalizing the fluorescence signal by the elastic scattering [26,27]. Our setup used several different combinations of color glass filters and diffractive gratings; hence was not optimized for measuring the elastic scattering. Moreover, in a standoff setting, the elastic scattering will be influenced by background aerosols in the measurement path. The APS for particle reference, measured the size distribution of all particles (not only the fluorescent ones) at a single point in the probe volume, and consequently did not provide adequate information on the distribution of disseminated aerosols in the probed volume to find N of Eq. (1). Figure 8 (a) shows an example of the measured total fluorescence when the aerosols were excited at 294 nm. Also shown is the particle concentration, meaning the integral of all aerodynamic diameters, as measured by the APS during a substantial release of OA. The APS and fluorescence curves correlate well taking into account that the APS has a much lower sampling rate than the standoff instrument, and the fact that the APS measured at one point location within the probed volume. The atmospheric effects in the fluorescence spectral interval may be neglected for relevant standoff distances. Transmission curves through various distances of standard atmosphere (7°C temperature, 85% relative humidity, 3 m above ground) were calculated using MODTRAN [21], see Fig. 8(b).

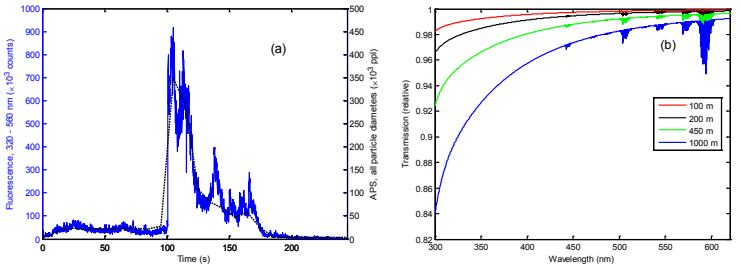

Fig. 8. (a) Comparison of measured fluorescence in the spectral range 320-560 nm (blue) and total number of particles (integrated over all aerodynamic diameters) as measured by the APS (dashed black), acquired during the release of OA while operating the lidar with the 294 nm excitation source. (b) Atmospheric influence on fluorescence spectral interval as calculated by MODTRAN, after propagation through 100 m, 200 m, which was the distance used in the experiment, 450 m and 1000 m atmosphere. See text for atmospheric parameters used in the simulations.

Therefore, in this section we present the spectra corrected for the instrument spectral response, and normalized with respect to laser pulse energy and the measured concentration of disseminated particles, as explained above, for the two excitation wavelengths, see Fig. 9. The anthrax simulants BG and BT fluoresce significantly stronger when excited by 294 nm than 355 nm. When exciting the aerosolized agents by a given pulse energy, the fluorescence is 6-8 times more intense at 294 nm than 355 nm laser wavelength. The strong 355 nm signal in the 294 nm excitation curve stems from backscattered 355 nm light that was not sufficiently attenuated before directing the pulse along the optical axis of the telescope. The fluorescence from an aerosol containing EH has approximately the same magnitude for both excitation wavelengths. Like for *E.coli*, it also seems clear that there is significant NADH content in the cells. MS2 is a simulant for BWA in the form of virus. The magnitudes of the spectra are similar for the two excitation wavelengths. The bacteriophage MS2 is a virus that infects *E.coli*. The solution was filtrated using a 0.2 µm filter before it was released in order to remove the *E.coli* bacteria. The fluorescence at 355 nm excitation indicates presence of NADH, related to metabolism which does not take place in virus. On the other side, the bacteria, and thus NADH, should have been significantly reduced by centrifuging and

#175155 - $15.00 USD Received 30 Aug 2012; revised 15 Oct 2012; accepted 16 Oct 2012; pub. 24 Oct 2012

filtration. However, the growth medium and NADH from damaged *E.coli* cells may be dissolved and pass filtration. OA is a simulant for toxins, and contains ~1% tryptophan [7, p. 445]. We therefore expected significantly stronger fluorescence at 294 nm than at 355 nm. Indeed it is stronger, however only by a factor of two. 294 nm excited SM fluoresces about twice as strongly as if excited at 355 nm.

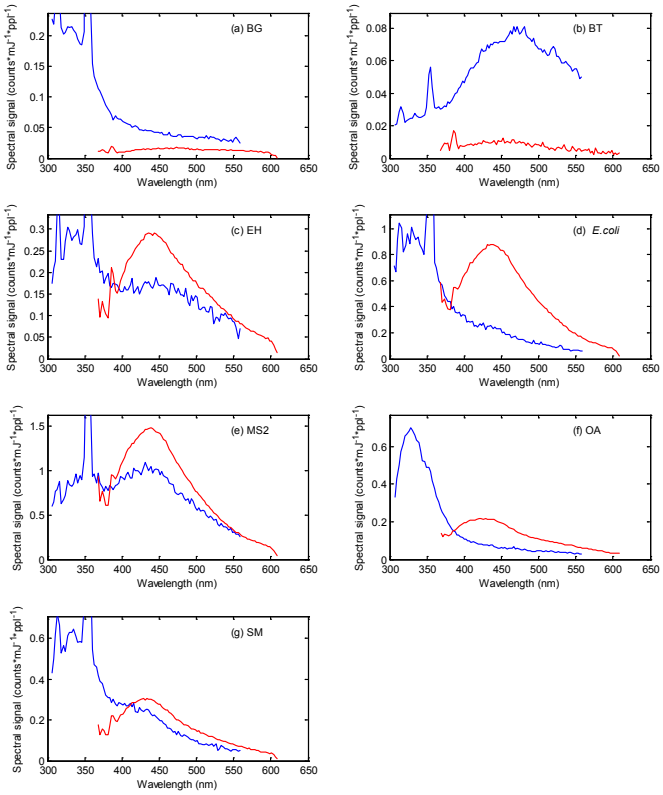

Fig. 9. Measured fluorescence following excitation by 294 nm (blue) and 355 nm (red) pulses for different aerosolized biological agents; (a) BG, (b) BT, (c) EH, (d) *E.coli*, (e) MS2, (f) OA and (g) SM. The spectra have been corrected for instrument spectral response, excluding ICCD gain, which was set to maximum, (approximately 800x), during all measurements. The fluorescence levels have been normalized with respect to laser pulse energy and particle concentration level.

4.3 Comparison of agent spectra at equal excitation wavelength

The magnitude of the fluorescence response as function of the excitation wavelength is an important parameter for the choice of laser wavelength. However, in terms of the ability to discriminate between different agents, the dissimilarities of the spectral features are crucial. In Fig. 10, the spectra for all the different agents at equal excitation wavelength are shown. The spectra were arbitrarily normalized for the purpose of comparing shapes.

As discussed at the beginning of this section, the spikes seen in the spectra are other effects than fluorescence from the agents. By visual comparison, an excitation wavelength at

#175155 - $15.00 USD Received 30 Aug 2012; revised 15 Oct 2012; accepted 16 Oct 2012; pub. 24 Oct 2012

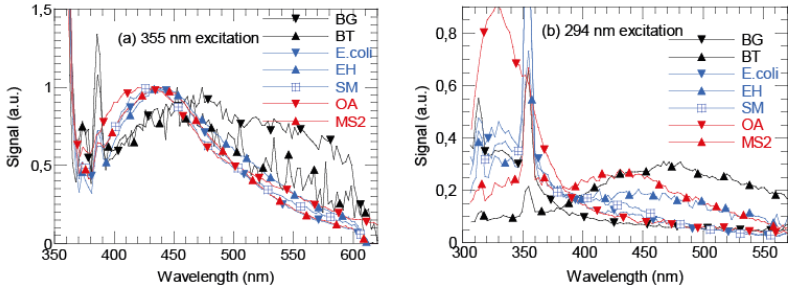

Fig. 10. Fluorescence spectra corrected for instrument spectral response, and normalized in order for visual comparison of shape for the seven different agents when excited by (a) 355 nm and (b) 294 nm radiation.

294 nm seems to generate more distinct fluorescence spectra than 355 nm excitation does. In the latter case, classification using benchmark methods, such as principal components analysis and support vector machines, is demanding due to the similarity of the spectra for the different agents. However, a genetic algorithm employed to the same data set outperformed classical methods in terms of false alarm rate [4]. The considerably larger variation in spectra with 294 nm excitation implies that we should expect even better classification results, meaning lower false alarm rates in terms of standoff detection performance at comparable laser pulse energies. However, classification has not been a topic of this work.

The fluorescence spectra are influenced by the growth media, and the preparation of the bioaerosol [9,17,26,28]. This has not been investigated in the experiments presented herein, but we note that EH, *E.coli*, SM (and MS2) which were cultivated using the same growth medium, and prepared in the same way, all have very similar fluorescence spectra after 355 nm excitation. The 294 nm excited spectra, on the other hand, possess more distinct spectral features. This observation favors the use of the shorter excitation wavelength.

4.4 Comparison of agent spectra with other publications

Fluorescence spectra of the same biological agents as studied in the current work have been presented in several publications. However, these are measurements of individual aerosol particles [29,30], or close-up laboratory measurements of aqueous solutions and aerosols [8,31], carried out at a number of different excitation wavelengths. When comparing these close-up spectra to standoff spectra, effects such as Raman scattering by atmospheric nitrogen, and in our case, 355 nm elastic scattering in the 294 nm excitation scheme, have to be taken into account. By doing this, the spectra compare well. This applies to the BG spectra (*Bacillus subtilis* compared with *Bacillus atrophaeus*), *E.coli* and albumin (albumin compares well to ovalbumin, whereas the bovine serum albumin spectrum is shifted to longer wavelengths), whereas the bacteriophage MS2 spectra [29] differ significantly for both excitation wavelengths. This may be attributed to fluorescence from the growth medium and aerosol preparation as discussed in Sec. 4.2.

4.5 Factors affecting signal-to-noise-ratio

In a system for standoff detection, several factors influence on the system performance. Our system corrects for background light on the fly by acquiring spectra at twice the laser pulse rate and subtracting the passive from the active spectrum. The noise level (or background level) of the system is strongly affected by ambient light and also of the gating time of the ICCD camera. With the settings used in this work, the rms background signal was about 30-150 counts/pulse per channel when operating under varying daylight conditions with a short gating time. A longer gating time, as would typically be used in open field surveillance, would

#175155 - $15.00 USD Received 30 Aug 2012; revised 15 Oct 2012; accepted 16 Oct 2012; pub. 24 Oct 2012

increase this accordingly. At low ambient light conditions, however, the background signal will be significantly smaller.

The signal, on the other hand, depends linearly with laser energy and with area of the collecting aperture, and is inversely proportional to the square of the standoff distance. The signal-to-noise (or signal-to-background) ratio can also be improved by reducing the spectral resolution. We have previously shown for a 355 nm based lidar that the number of spectral channels can be reduced to 10-15 before the signal processing performance with respect to false alarm or false negative is affected [4,11,32]. Such an analysis has not been a part of this work, but it seems likely that the more distinct fluorescence spectra with 294 nm excitation may see a similar or even smaller requirement for spectral channels.

5. Conclusion

The experiments verified that ultraviolet laser induced fluorescence featuring excitation by a laser with wavelength 294 nm is more efficient than one at 355 nm and comparable pulse energy for standoff detection of biological aerosols that are BWA simulants. In particular, the anthrax simulants BG and BT had almost an order of magnitude stronger fluorescence, whereas the toxin simulant OA fluoresced approximately twice as strong at the shorter excitation wavelength. For the virus simulant MS2, and the *E.coli* and SM cultures of bacteria, the fluorescence responses were approximately the same in terms of magnitude for the different excitation wavelengths. Stronger fluorescence means higher sensitivity for a given excitation pulse energy. This is crucial for standoff distance and detectable concentration levels. More importantly, however, was the prominent dissimilarities between the agent spectra at the shorter excitation wavelength as compared to those at 355 nm excitation. The fluorescence spectra measured at 210 m standoff distance compare well with spectra measured in laboratory experiments or using aerosol sampling systems; except for MS2, which may be a result of poor separation from the growth medium and aerosol preparation. More distinguishable spectra allow for better classification thus lower false alarm rates, which in the end is the major challenge of standoff detection. Even better performance in terms of false alarm rate, would be an instrument utilizing two UV excitation wavelengths, as asserted by publications on laser induced fluorescence measurements on individual particle aerosols [26,27,29,30]. The standoff instrument of the present work is capable of emitting both wavelengths. Minor modifications will allow for automatic dual excitation wavelength operation.

In order to avoid problems with Raman scattering of atmospheric constituents appearing within the peak of the fluorescence spectrum, the excitation wavelength should ideally be shorter than the 294 nm used in these experiments. The advantage of moving the Raman scattering out of the fluorescence window has to be balanced by the reduced transmission in air caused by ozone pollution. An optimal excitation wavelength is probably in the 280-290 nm range. In any case, using a different excitation wavelength than one available from a commercial laser has to be traded off against the cost of generating it in terms of pulse energy and system complexity.

Acknowledgments

We acknowledge Torbjörn Tjärnhage (Swedish Defence Research Agency) for lending us the dry release equipment. We also acknowledge Arthur D. van Rheenen (FFI) for providing the MODTRAN calculations.